Optical Studies of Photonic Crystals and High Index-Contrast Microphotonic Circuits

by

Peter Thomas Rakich

B.S. Honors Physics
Purdue University, 1999

SUBMITTED TO THE DEPARTMENT OF PHYSICS IN PARTIAL FULFILLMENT OF THE REQUIREMENTS FOR THE DEGREE OF

DOCTOR OF PHILOSOPHY IN PHYSICS
AT THE
MASSACHUSETTS INSTITUTE OF TECHNOLOGY

JUNE 2006

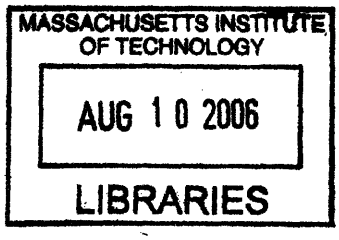

Signature of Author.....
Department of Physics
May 19, 2006

Certified by.....
Erich P. Ippen
Professor of Physics
Elihu Thompson Professor of Electrical Engineering
Thesis Supervisor

Accepted by.....
Thomas J. Greytak
Professor, Associate Department Head for Education
Department of Physics

Massachusetts Institute of Technology
Professor Erich P. Ippen
Professor John D. Joannopoulos
Professor David E. Pritchard
Department of Physics

Doctor of Philosophy Dissertation

Optical studies of photonic crystals and high index-contrast microphotonic circuits

by

Peter T. Rakich

Supervisor: Professor Erich P. Ippen

Cambridge MA, 2006

In loving memory of my father
Steven D. Rakich
1943-2005

Optical studies of photonic crystals and high index-contrast microphotonic circuits

by

Peter Thomas Rakich

Submitted to the Department of Physics in partial fulfillment of the requirements for the degree of Doctor of Philosophy in Physics

Abstract

Both high index-contrast (HIC) photonic crystals and HIC microphotonic circuits are presented in this thesis. Studies of macro-scale 2D photonic crystal meta-materials are first described. Through comparison of experimental and theoretical beam evolution about the super-collimation frequencies, the effects of disorder on beam evolution are pinpointed. Despite the effects of disorder, super-collimation is found to be robust, producing stationary beam-widths over 600 isotropic diffraction-lengths. In addition, nano-scale photonic crystal defect modes are studied over large optical bandwidths through newly developed supercontinuum based techniques. Novel all-fiber supercontinuum sources facilitate the generation of unpolarized supercontinuum light over 1.2-2.0 micron wavelengths. Broadband experimental methods make possible the application of these sources to the study of 1D and 3D photonic crystals with defect states.

Studies of both static and dynamic microring resonator based HIC filters are described. Numerous microring based studies are reported which lead to frequency-compensated multi-ring filters, permitting the first high-fidelity microring filters in HIC microphotonics. Though telecom-grade performance achieved via frequency compensation, the aforementioned filters exhibit severe polarization sensitivities, making them incompatible for real-world applications. Through integration of identical sets of these filters in a generalized polarization diversity scheme, polarization insensitive HIC filters are demonstrated for the first time, yielding a maximum polarization dependant loss of 2.2 dB over broad bandwidths. Finally, evanescent field-perturbation is investigated as a means of tuning microcavities over ultrawide wavelength ranges. Through nano-metric control of a silica perturbing body in the near-field of a microring waveguide, a 27 nm (or 1.7%) reversible tuning of its cavity mode is achieved.

Thesis Supervisor: Erich P. Ippen Title: Professor of Physics, Elihu Thompson Professor of Electrical Engineering

Contents

Acknowledgements

Over the course of my thesis studies, I have had the tremendous honor of working with a host of talented scientists and engineers from whom I have learned a great deal. I cannot emphasize how much people shape the experience one has in graduate school.

Let me begin by thanking Professors Pritchard, Joannopoulos and Ippen for taking the time out of their busy schedules to be on my thesis committee and critique my thesis.

To Professor Ippen, I owe a great debt of gratitude. I am honored that he took me on and I am thankful that he believed in me, even at times when my confidence in myself began to wane. Working in his lab has been a pleasure, in large part, because he does a wonderful job of generating a creative atmosphere and treating his students with dignity and respect. He has always made himself available to discuss and develop new ideas, and to support whatever ideas his students want to throw themselves at. On numerous occasions, his years of research experience and his X-ray vision for research problems has saved me from troubles ahead. Through his guidance, I have had the good fortune to take part in cutting-edge research. Though these projects all come to an end, I hope to take carry on the pragmatic and forward looking approach to research that he has imparted to me.

I feel blessed to have taken part in research with the late Professor Hermann A. Haus. He was a truly inspirational as an academic and as a human being. I remember being electrified after meetings and discussions with him. He always had incredible perspective about science and history, as only someone who has taken part in that history can. Everything seemed possible after a brief discussion with Professor Haus. It is only after these meetings that my co-workers and I would realize "damn this is gonna be tough...". This is just a

testament to the fact that he was very inspirational for many of us in the Ippen group who benefited greatly from his presence. I was saddened by his passing, and miss him terribly.

In many ways Professor Joannopoulos has been an unofficial co-advisor involving several photonic crystal related research projects. His enthusiasm is contagious, and often just what a frustrated experimentalist needs to keep his nose to the grind-stone. Furthermore, I feel very lucky to have had such close interaction with him and his premier theory group. I am thankful for his support through numerous research endeavors described in this thesis.

Through studies of 2D photonic crystals presented in Chapter 1, I worked very closely with Marcus S. Dahlem, Mihai Ibanescu, Sheila Tandon, Marin Soljacic and Gale Petrich and Leslie Kolodziejski. Working with all of you through this research has been an exciting and creative process, producing outstanding theoretical and experimental work. Marin was responsible for stroke of genius, leading us to super-collimation studies, and Mihai skillfully performed the band-structure computations and photonic crystal design presented in Chapter 1. I am grateful to both Marin and Mihai for their willingness to entertain all of my questions about the physics of photonic crystals. At times I have been a student to both, and I am grateful to both for being willing teachers. Sheila developed the fabrication process yielding world-class photonic crystals for these optical studies. It should be said that, without her, these studies wouldn't have happened. I thank her for entertaining my curiosities about fabrication and for having patience throughout longer-than-anticipated optical studies. Throughout the optical studies Marcus and I had a very close partnership. After observing him in action, I am absolutely certain that he can do anything he puts his mind to. He has been a remarkable and creative scientist with whom I have forged a lasting friendship. After countless late nights in the lab, I know more about him than I should reveal. I am grateful to him for being supportive of me in some pretty rough times, and my life has been enriched by knowing him. Marcus, no more hanging off of 100 meter tall castle walls WITH ONE ARM!

The supercontinuum based studies of Chapter 2 would never have happened without Hideyuki Sotobayashi, Juliet Gopinath and Jason Sickler. I am grateful for their friendship and generosity inside and outside of the lab. This work merged all of the expertise in our lab, and would never have been possible without them. Hide and Juliet investigated numerous nonlinear fibers discussed in Chapter 2 and taught me a great deal about nonlinear fiber-optics and laser-physics. Juliet is a relentless experimentalist and friend, whose diligence and

work ethic are unparalleled. Thank you for friendship and guidance over the years! Through work with Hide, I have come to understand that he knows a hell-of-a-lot more than he often articulates. I am honored to be his student and friend. Jason Sickler has been a wonderful friend and colleague in this project and in many others. He always finds time to ponder technical problems with others, and lends a helping had whenever possible. I owe much of my understanding of fiber-lasers and fiber-optics to countless discussions with him. I am thankful for his friendship. The 1D photonic crystal microcavities of Chapter 2 were the fruits of Chee Wei Wong efforts. Through our lab-partnership we managed to learn a great deal about waveguides and photonic crystals. He isn't afraid of anything. This is what is necessary to do interdisciplinary research! I am also indebted to Steven Johnson for running numerous FDTD simulations of the 1D photonic crystal microcavity, and numerous discussions. Finally, I should thank Minghao for involving me in his 3D photonic crystal work presented at the end of Chapter 2. I will only stay up that late to do measurements for you Minghao!

Through the ring resonator work presented in Chapters 3 and 4 I have had the great pleasure of working very closely with Tymon Barwicz, Milos Popovic, and Michael Watts, and Charles Holzwarth. I have never known a more passionate group of scientists and engineers. Whenever discussion starts... sparks fly!! World-class nano-fabrication of microrings and optical circuits of Chapter 3 were performed by Tymon. I am thankful to Tymon for entertaining countless questions about materials science; he makes a very good teacher, since his enthusiasm is truly contagious. I owe much of my understanding of waveguides and integrated optics to countles... countless discussions with Milos. I am honored that he feels comfortable to share ideas and curiosities on a daily basis. I have benefited greatly from his friendship and feedback over the years. I have interacted most with Mike on the evanescent tuning research and well as in the conceptualization of several measurement techniques. I can always count on some very creative and fresh feedback from him, and I hope that our we continue research doing research together in the future. The loss studies of Chapter 3 wouldn't have happened without Trey. It has always been a pleasure. Thanks for explaining the materials science to me! I'll see more of you.

Through the numerous research endeavors of grad school, friends and co-workers are often indistinguishable. When I first arrived at MIT I was rather uncertain about whether I really belonged at a place like this; however,over the years (and despite the stress of graduate studies), I have continued to feel more comfortable and happy than I have ever been in my life. This, I realize, is because I am

surrounded by peers that I can relate to for the first time in my life. This is priceless experience for someone who has always considered himself a loner. If I am to attempt to name you all here, I am afraid that I will fail. So, I'll do my best to thank you in person.

Here I thank just a few of the many mentors who have impacted me greatly during and before my graduate studies:

Daniel Ripin was a superb mentor through my first couple of years in the Ippen group. As a first year student, I hounded him endlessly about photonic crystals and optics, and he did a wonderful job of introducing me to numerous projects in the Ippen group. Through our countless hours in the lab together, he was always a fascinating conversationalist on topics ranging from politics to religion to philosophy. The value of this cannot be underestimated while performing many of the unenviable tasks that grad students spend a great deal of time doing. Furthermore, he always did his best to foster a sense of community in the Ippen group. As a mentor, he could be counted on for selfless guidance and words of wisdom. Thank you for all of these things Dan.

As a sophomore at Purdue University, Professors David Nolte and Anant Ramdas made a big impact on me through their teaching of the undergraduate optics course. Both were very passionate about optics, and did a wonderful job of conveying this to the students through their lectures and laboratory class. This course represented a turning point for me in my studies. During the course I remember rummaging through the Physics stacks and reading every optics book I could get my hands on. At the end of the term, I begged Professor Nolte let me take part in activities in his lab. He obliged, and over the following several years I was exposed numerous real-world research problems. He gave me as much responsibility as I could possibly handle. He was a very patient and encouraging mentor, humoring numerous basic questions. Through this experience, I also met Mihaela Dinu, who was then a graduate student of Professor Nolte's. Through much persistence, I managed to hound her into explaining all sorts of interesting physics and optics to me. I would stay late to help her fill the helium dewar, and in exchange she would explain the experiments to me. With time, she became an unofficial mentor of mine, and I am grateful for her generosity and friendship. I feel that I owe both of them a great deal. (To Mihaela: For the record, Linear Algebra and Complex Analysis aren't for kinder gardeners!)

During my Junior year of college, I also had an invaluable intern-ship experience working under Mario Paniccia of Intel Corporation. His was a very intense, but

exciting group to be a part of. Mario could probably see that I was far too serious for my own good, and wanted some really tough problems to work on. He gave me as much as I could handle, and more! He was a very supportive mentor, and a terrific person. (I am sorry if was a willful pain-in-the-ass sometimes Mario. Thanks for putting up with me.)

The summer before my senior year of college, I was without research plans, and approached Professor Andrew Weiner to see if he could use an undergraduate over the summer. He agreed to take me on, and I now realize how lucky I was to receive his mentoring and guidance. He was not only a very insightful scientist and inventor, but also one of the most talented managers that I have ever had. I felt that I clicked in his group, and I really enjoyed working under both him and Dan Leard over the following year. Thank you for your generosity, and for helping me find my way to graduate school.

Last, but not least, I must thank the loved-ones who have supported me throughout this process:

Waty Lilaonitkul emotionally supported me through the first several years of grad school, which invariably has its ups and downs. I don't know how I would have made it through the grueling qualifier process without her unconditional love and support. Thank you Waty.

Tanja Atanasijevic has been by my side for the remaining several years of my graduate studies. She helped me through some very troubling times, somehow making it possible to enjoy life when things seemed so dark. You have been wonderful. I cannot thank you enough. I love and adore you.

Without my loving and supportive family, especially Mom, Dad, Nick and Kate, I don't know where I would be. You guys are my core. You have shaped who I am, and you have always helped me to remember what is really important in life. You are priceless to me.

Preface

Engineering of high-refractive-index-contrast waveguides and photonic crystals at the nano-scale enables unprecedented control of light at both micro and macro-scales. Through the construction of high-index-contrast (HIC) waveguides, tight bending radii and micron-scale optical cavities are possible. Furthermore, patterning of periodic structures facilitates the strong Bragg scattering necessary for photonic bandgap engineering, yielding macro-scale effective optical properties and micron-scale defect-modes. Both approaches to the manipulation of light, promise to yield numerous technological and scientific advances.

In this thesis, optical studies of both photonic crystals and HIC microphotonic circuits are described, concentrating on experimental methods and the discoveries made through application of these methods. In Chapter 1, we present studies of large-area 2D photonic crystal meta-materials, which enable centimeter-scale super-collimation, and examine the effects of disorder on beam evolution about the super-collimation frequency. Chapter 2 focuses on newly developed supercontinuum based techniques for the study of nano-scale photonic crystal devices over large optical bandwidths. These methods are then applied to the study of 1D and 3D photonic crystals with defect states.

In Chapters 3 and 4, studies of both static and dynamic microring resonator based HIC filters are described. In Chapter 3, we report numerous microring based studies leading to the first high-fidelity multi-ring filters and polarization insensitive HIC microphotonic circuits to date. Finally, Chapter 4 investigates evanescent field-perturbation as a means of tuning microring and other types of microcavities. Through nano-metric control of a silica perturbing body, a 27 nm (or 1.7%) reversible tuning is achieved in HIC microring resonators.

It should be said that these projects only represent a fraction of the projects that I have participated in during my tenure in Professor Ippen's lab. Through the above projects, and numerous others, I have had unparalleled exposure to a vast number of experimental and theoretical problems, and had the op-

portunity to play a significant role a number of numerous exciting projects. These have lead to a great number of experiences not mentioned in this thesis. Among them are: (1) The development of tunable Ti:Sapphire laser and Raman microscope, for resonant-Raman study of carbon nanotubes. (2) The development of Geiger-mode photon counters for photon-starved NSOM experiments. (3) Photoluminescence studies of active 2D photonic crystal LEDs. (4) Experimental studies of two different classes of microphotonic optical-MEMS devices. (5) The proposal and development of novel mode-locking mechanisms through nonlinear spatial evolution. While some of these projects have lead to publications, some have not; however through all of them,I have learned a great deal. During my time in the lab (36-324), its appearance has been transformed numerous times in order to accommodate these projects. At this time, the laboratory is over-taken by tunable lasers, nano-positioning equipment, and countless optical microscopes which supplement our vision through numerous tedious experiments. Although many of the experimental diagrams shown in the thesis appear very conceptually simple, in practice, we often employ as many as 5 separate cameras embedded in different microscopes to monitor an experiment which takes place on a integrated optical circuit which is much smaller than a human fingernail!

Chapter 1

Super-collimation in 2D photonic crystals

1.1 Introduction

A photonic crystal is an optical medium possessing a periodic modulation in its optical properties, typically in refractive index. Such periodicities give rise to Bragg resonances, which can drastically modify the optical properties at and about the Bragg frequency. On resonance, Bragg scattering gives rise to a band of frequencies over which there are no propagating optical states, referred to as a photonic bandgap. Above and below the Bragg frequency the effective index and group index can be greatly modified, drastically altering the temporal and spatial dispersion in such a medium. Both resonant (Bandgap) and non-resonant behavior of photonic crystals make possible engineering of optical properties and optical devices yielding an unprecedented level of control

over effective material properties, and ultimately the behavior of electromagnetic waves propagating inside of these devices and materials. As a result, photonic crystals have been the subject of intense study over the past decade giving rise to a burgeoning field of research [**1**, **2**, **3**, **4**]. Much of this research seeks to provide integrated optical devices which are sub-wavelength in size, with unparalleled performance.

This chapter focuses on some of the unique optical properties facilitated by photonic crystals through careful design of their dispersive properties. Photonic crystals of this type, often referred to as meta-materials, can enable remarkably anisotropic physical properties through proper engineering photonic band structure, in this case leading to greatly reduced spatial dispersion through an effect called super-collimation. In what follows, super collimation is demonstrated for the first time in a macroscopic photonic crystal system over centimeter scale distances, retaining spatial width confinement without the need for waveguides or nonlinearities. Through quantitative studies of the beam evolution in a 2D photonic crystal, it is found that the beam evolution in a real PhC cannot be explained from the dispersive properties alone. Through experimental and computational studies of the beam evolution, it is found that a miniscule degree of disorder is sufficient to disrupt the behavior of PhC meta-materials, and cannot be ignored in most cases. Despite the problematic effects of disorder, super-collimation is found to be remarkably robust over large length scales. It is discovered that this super-collimation possesses unexpected, but inherent, robustness with respect to short scale disorder (e.g. fabrication roughness) en-

abling super-collimation over 600 isotropic diffraction-lengths. The effects of disorder are identified through experiments and understood through rigorous simulations.

1.2 A key measure for super-collimation

A natural metric for the scale of collimation experiments is the length over which a Gaussian optical beam would normally spread by a factor of $\sqrt{2}$ in an isotropic medium, referred to as the isotropic diffraction-length. It is defined as

$$L_d = \pi w^2/\lambda_{||}. \tag{1.1}$$

Here w is the Gaussian beam waist radius and $\lambda_{||} = 2\pi/k_{||}$is the wavelength of light in the direction of propagation. Evidence of collimation has been observed in some beautiful early experiments [5, 6, 7, 8, 9, 10] in mesoscopic ($\sim$100 μm) systems. However, the utility of this effect is strongly linked to the distance over which super-collimation can be maintained, or more precisely, the number of diffraction-lengths possible. This figure of merit is important since it dictates the maximum density and complexity of an optical circuits based on super-collimation [9, 10, 11]. Previous experimental studies of super-collimation have used devices of small dimensions ($\sim$100 μm) to estimate the beam evolution in the PhC. However, estimates of this type translate to large uncertainties in macro-scale properties of these meta-materials, which are critical for appli-

cations such as optical interconnects and non-diffractive imaging. To address this issue, we present the first quantitative study of super-collimation, utilizing both near-field scanning optical microscopy (NSOM) and confocal imaging techniques, and we demonstrate that this phenomenon is indeed possible over as much as 600 isotropic diffraction-lengths. This represents a two orders of magnitude improvement over previous demonstrations, and is an important enabling step toward the creation of high-density and low-cost optical interconnects.

In what follows we describe the basic physics leading to super-collimation, and quantitative experimental studies of super-collimation in a silicon 2D photonic crystal. Through careful analysis of the beam evolution within the PhC, it is found that the beam evolution in a real PhC cannot be explained from the dispersive properties alone. Through experimental and computational studies of the beam evolution, it is found that a miniscule degree of disorder is sufficient to disrupt the behavior of PhC meta-materials, and cannot be ignored in most cases. Despite the problematic effects of disorder, super-collimation is found to be remarkably robust over large length scales.

1.3 Diffraction in Isotropic Media

Before we delve into a discussion of spatial dispersion (or diffraction) in highly anisotropic system, such as a 2D photonic crystal, it is helpful to begin by examining of the origin of spatial dispersion in the isotropic case. Analytical treatments of spatial evolution of propagating beams are explored quite thoroughly

in a number of classic texts, and will not be repeated here [12, 13]. Fortunately, a detailed analytical treatment is not necessary to understand the underlying physics involved in spatial evolution of propagating beams. For brevity, a simple heuristic explanation of diffraction and super-collimation is employed, which mirrors the fast-Fourier transform beam propagation method (FFT-BPM). This method is rigorously described in Ref. [4], and later used for computational studies of beam evolution in this chapter.

1.3.1 Analysis of diffraction with the dispersion surface

In describing diffraction, a number of different approaches are typically taken in pedagogical texts, ultimately leading to Frenel or Frauhoffer approximations of a scalar Green's function integral or particular solutions of the Helmholtz equation [14, 13, 12]. While these treatments of diffraction are incredibly useful for practical problem solving, they do not necessarily provide the most obvious explanation of why a beams tend to disperse as they propagate in free space, and how to modify the properties of a medium to effect its spatial dispersion. The key to these questions, however, can be understood through proper interpretation of a dispersion surface. The dispersion surface (also referred to as the projected band structure) is defined as the set of all points swept out by $\vec{k}(\omega)$ for a given frequency ω, and provides a graphical means of determining the propagation constant associated with a given transverse wave-vector (or spatial frequency).

To examine the origin of spatial dispersion with use of the dispersion surface,

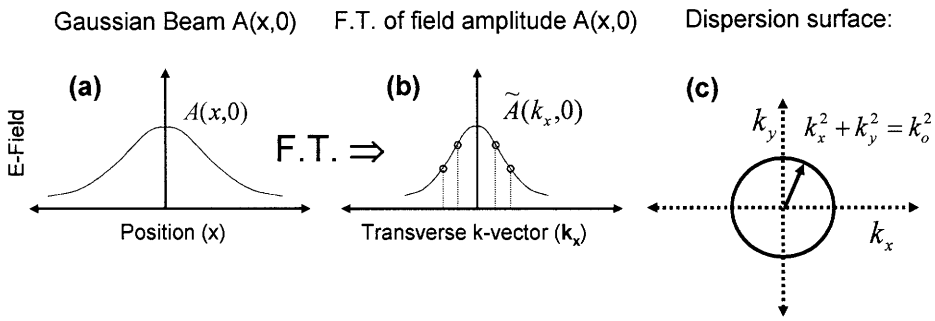

Figure 1.1: (a) Electric field profile of a Gaussian beam vs. position. (b) Fourier transform of Gaussian beam in terms of conjugate variable k_x. (c) Dispersion surface of isotropic medium.

we need only notice that any propagating beam can be decomposed into a basis of plane-waves. See for example Fig. 1.1a, which depicts the cross-section of Gaussian beam for which we assume a flat phase vs. position (x), propagating in the y-direction. The Fourier transform, which is also a Gaussian, reveals the amplitude of the different transverse wave-vectors (or spatial frequencies) which make up the Gaussian beam (see Fig. 1.1b). The dispersion surface, in the isotropic case, is defined by a circle with a radius equal to the square of the propagation constant, allowing us to easily determine the phase velocity of each spatial frequency. For clarity, several spatial frequencies are depicted in vector form in Fig. 1.2a. Since the length of each plane-wave's wave-vector is conserved, higher spatial frequencies must have smaller propagation constants ($k_{||}$). Therefore, as a beam propagates, the higher spatial frequency components of its' plane-wave basis will incur a larger phase change than low spatial frequencies, resulting in phase walk-off. This results in beam dispersion, or diffraction. This simple description of propagation, through use of the dispersion surface,

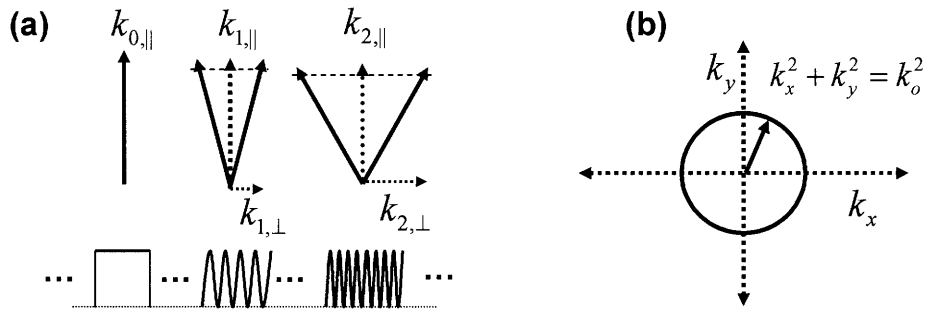

Figure 1.2: (a) Three characteristic spatial frequencies, illustrated both in vector form and in space. (b) The dispersion surface of an isotropic medium.

provides a physically accurate and insightful understanding of diffraction.

1.4 Diffraction in Photonic Crystal Meta-Materials

From this simple analysis presented above it becomes clear that an isotropic medium must always exhibit spatial dispersion. It is also evident that reduced spatial dispersion can only occur if all of the spatial frequencies comprising a beam have the same, or similar propagation constant ($k_{||}$). In other words, the dispersion surface must be flat. Although it seems unlikely that spatial dispersion can be drastically reduced in naturally occurring anisotropic media, through new opportunities presented by photonic bandgap engineering, some very interesting possibilities present themselves.

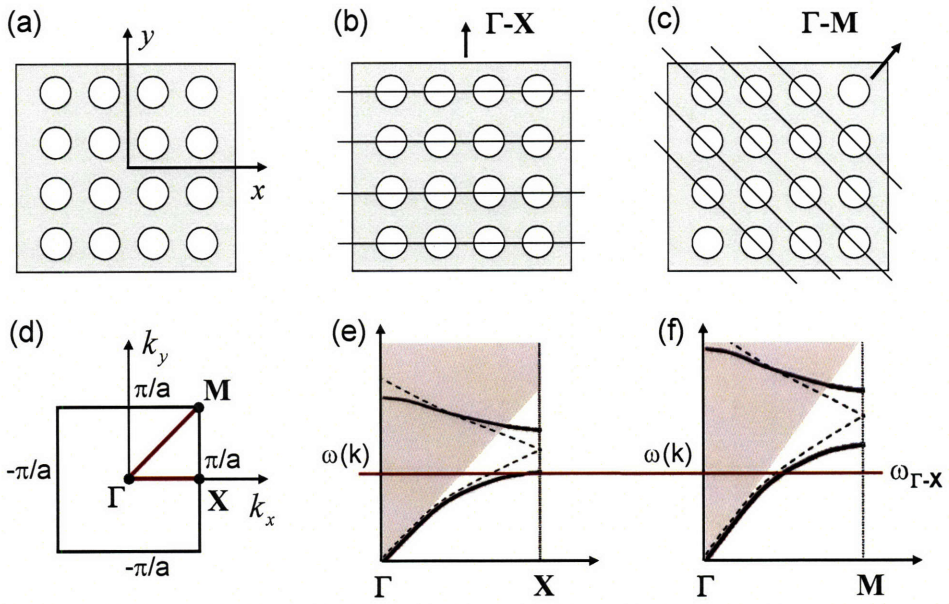

Figure 1.3: (a) A 2D photonic crystal comprised of a square lattice of holes (b) Bragg planes corresponding to Γ-X direction (c) Bragg planes corresponding to the Γ-M direction (d) Reciprocal space representaion of Γ, X and M points (e) Sketch of dispersion relation plotted along the Γ-X direction and (f) the Γ-M direction. Dashed curves indicate the dispersion relation for the 'free' modes and solid lines represent the dispersion of the photonic crystal structure.

1.4.1 Bragg scattering & the dispersion surface

An example of a 2D photonic crystal can be seen in Fig. 1.3a, which consists of a dielectric slab with a square lattice of air holes. In this structure, the periodic modulation in index of refraction results pronounced Bragg resonances in various symmetry directions. In Fig. 1.3b-c some Bragg planes have been highlighted corresponding to the (Γ-X) and (Γ-M) symmetry directions. In both symmetry directions Bragg scattering couples the forward and backward propagating waves strongly, resulting in a photonic bandgap. Since the separation

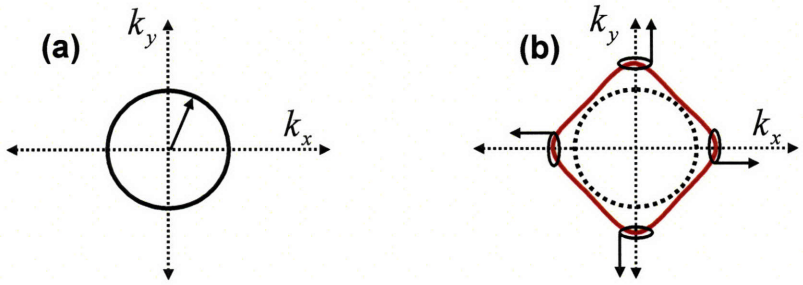

Figure 1.4: (a) An isotropic dispersion surface. (b) Sketch of modified dispersion surface in the vicinity of Γ-X resonances. Close proximity to these resonances results in distortion of dispersion surface in k_x and k_y directions

of the Bragg planes is smaller in the Γ-M directions, the Bragg resonance and the corresponding photonic bandgap must occur at higher frequencies. Dispersion relations corresponding to both the Γ-X and Γ-M symmetry directions are sketched in Figs. 1.3e-f, in the reduced-zone scheme. Here the dashed line represents the "free" slab modes (or the modes that would exist in the absence of holes) and the solid line is the dispersion relation a structure with a periodic array of holes.

It is important to note that the photonic bandgap results in greatly modified dispersion above and below the bandgap, giving rise to an increased phase index (n_p) and group index (n_g) near the band-edge. For frequencies below bandgap, which is what interests us in the study of dispersive meta-materials, it is clear that the Γ-X resonances are the closest-lying resonances, resulting in the largest distortion to the dispersion surface. From these simple observations, we can form a picture of how the dispersion surface is modified as ω approaches the

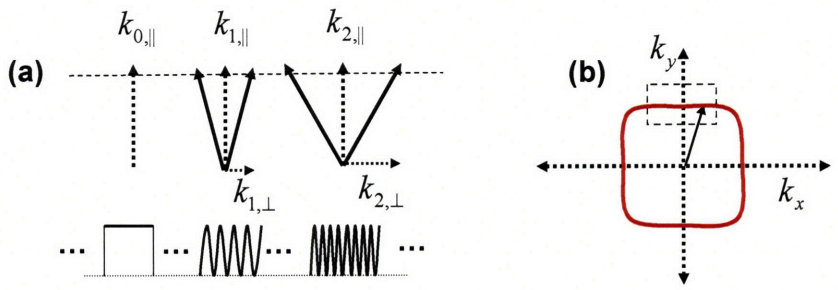

Figure 1.5: (a) Vector representation of spatial frequencies and corresponding propagation constants in PhC system when propagating along the Γ-M symmetry direction (b) Dispersion surface of PhC with 45 Deg. rotated coordinates k'_x and k'_y corresponding to Γ-M symmetry direction.

band edge of the fundamental Γ-X resonance. In the vicinity of the $\Gamma - X$ Bragg resonance (indicated by the solid line extending between Figs. 1.3e-f) , this increase in n_p effectively stretches the dispersion surface in the Γ-X direction, transforming the circular dispersion surface of Fig. 1.4a to a surface more similar to that seen in Fig. 1.4b.

1.4.2 Special case: flat dispersion surface

Interestingly, this topological change makes possible a flat portion of the dispersion curve in the Γ-M direction. In this case, if a Gaussian beam is excited in the Γ-M direction, as illustrated in Fig. 1.5, greatly reduced spatial dispersion can be expected for some band of spatial frequencies. This reduced spatial dispersion, enabled by photonic bandgap engineering, is called super-collimation, which is the subject of this chapter. So far we have arrived at some conceptual understanding of this effect. However, rigorous methods for the computation

of band structure can be found in Refs. [1, 2, 3, 15].

1.5 Photonic crystal system under study

In sections 1.3-1.4 we described the conceptual foundations of spatial dispersion, and painted a simple picture of how Bragg resonances can be utilized to engineer unique dispersive properties in 2D photonic crystals. In this section we describe experimental studies of super-collimation using 2D PhC fabricated in a silicon-on-insulator (SOI) material system, and compare the experimental results to rigorous simulations.

1.5.1 Fabricated large-area 2D photonic crystal

The physical system under study consists of a centimeter-scale 2D PhC slab formed by a square lattice of air holes in a 205 nm thick silicon film. Vertical confinement of the light in the film is achieved through index guidance, with an air over-cladding and a 3.0 m-thick SiO_2 under cladding. A scanning electron micrograph (SEM) of the large area PhC, fabricated by Sheila Tandon through interferometric lithography [10], is shown in Fig. 1.6a. The lattice constant (a = 350 nm) and hole radius (r = 0.3a) were chosen to produce an ultra-flat dispersion surface in the 1.5 μm wavelength range for TE polarized light (electric field parallel to the 2D plane). The dispersion surface of the PhC slab under study was computed with a 3D frequency-domain eigenmode solver by Mihai Ibanescu [11]. The indices of refraction used for the simulations were

$n_{silicon} = 3.5$, $n_{silica} = 1.45$. Fig. **1.6**b shows several equifrequency contours for the lowest band of the PhC, with magnified views of the relevant contours near the wavelengths of interest (Fig. **1.6**c). For the normalized frequency $\omega = a/c = 0.228$, the PhC exhibits remarkably little spatial dispersion in a transverse wavevector (k_y) range from -0.05 to 0.05 (2π/a).

1.6 Evolution within ideal photonic crystal

Beam evolution of light propagating in the PhC can be quite naturally simulated through the beam propagation method (BPM) based on the computed dispersion surfaces (Figs. **1.7**a-c). For a detailed description of the BPM method, and how it is implemented, see Ref. [**4**]. In each of the simulation domains shown in Figs. **1.7**a-c, the PhC is excited with a 1 μm FWHM beam for comparison with experiment, and is displayed over a 500 x 225 μm area located approximately 500 μm to the right of the input. As one might expect, the beam divergence is negligible for $\omega = 0.228$, where the dispersion surface is flattest. It is interesting to note that at frequencies below the super collimation frequency ($\omega = 0.215$), the dispersion surface $k_y(k_x)$ has two inflection points, seen in Fig. **1.7**. This unusual topology results in the mapping of many of the higher spatial frequency transverse wave vector components of the Gaussian beam to angles ($\pm\theta_{max}$) defined by the inflection point [12]. This leads to the unusual beam evolution seen in Fig. **1.7**a, namely the sharp roll-off in the transverse beam profile. In contrast, the transverse profile of the beam is much more diffuse for $\omega = 0.239$,

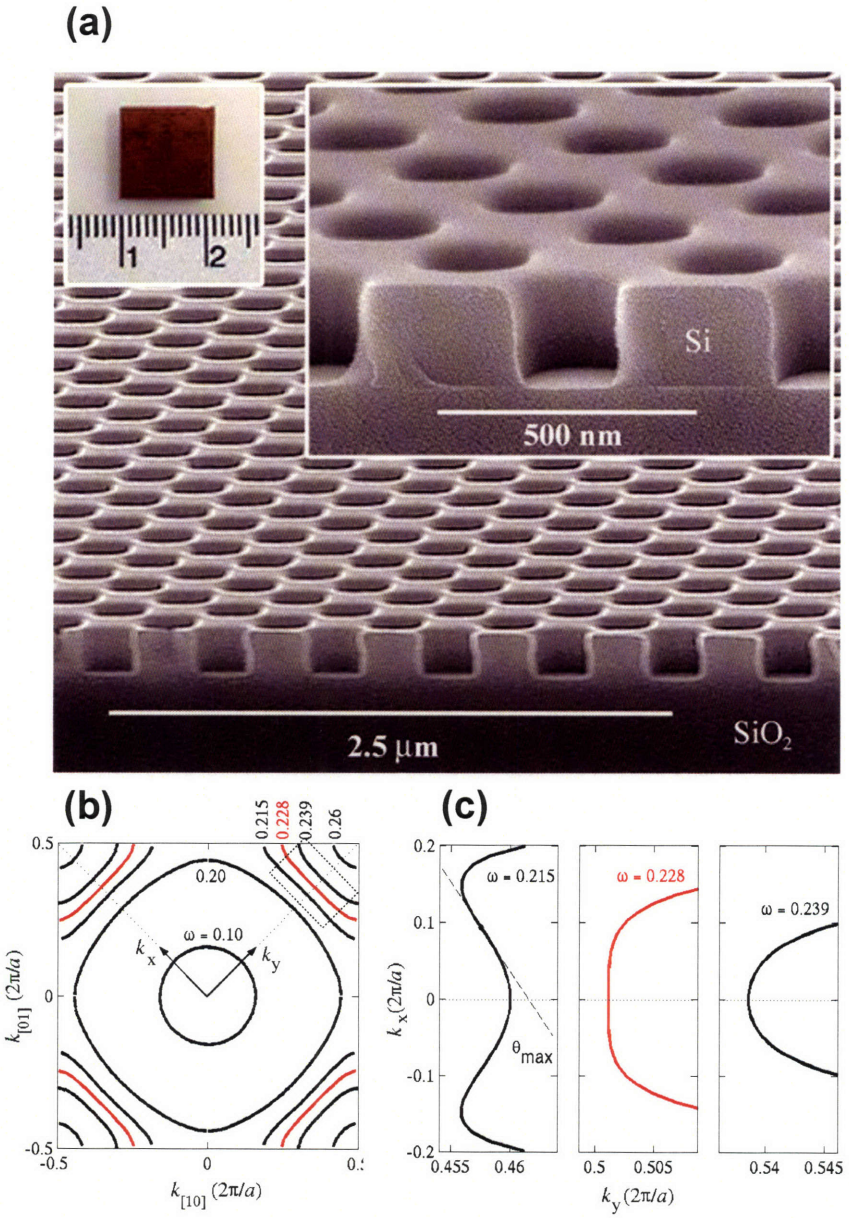

Figure 1.6: (a) Scanning electron micrograph showing large area cross-sectional image of PhC. Left inset: Digital photograph showing full 1x1 cm sample. Right inset: Scanning electron micrograph showing cross-section of the PhC structure. (b) Equifrequency contours for the lowest band of the fabricated PhC. (c) Magnified view showing the "flat" region of the equifrequency contours from b where super-collimation occurs. Plot is rotated by 45 deg so that k_x is the wave number along the propagation direction (Γ-M) and k_y is the transverse wave number [SEMs of (a) by Sheila Tandon, Band structure computations of (b) & (c) by Mihai Ibanescu]

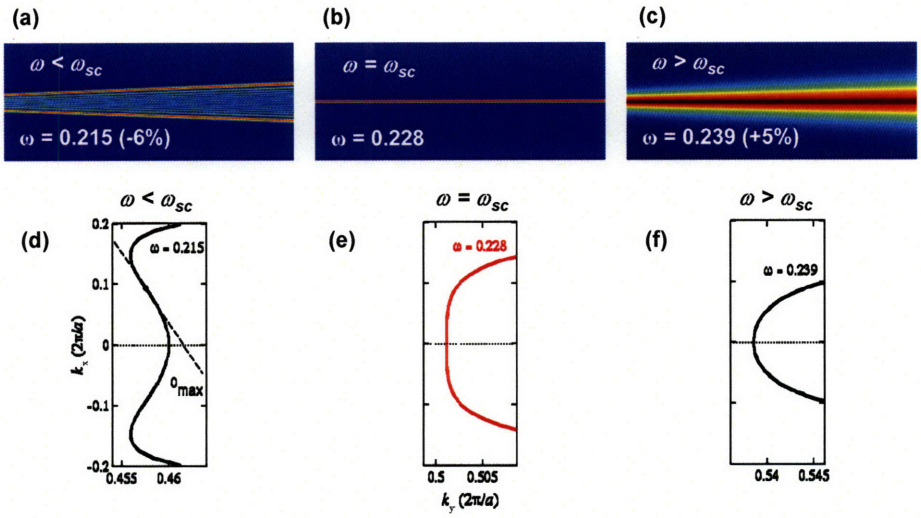

Figure 1.7: (a) Simulated evolution of intensity profile for $\omega = 0.215$. Similarly (b) & (c) are profiles computed for $\omega = 0.228$ and $\omega = 0.239$. The computed dispersion surfaces used to perform simulation (a)-(c) are shown in figs (d)-(f).

Fig. 1.7c. This is because the surface can be approximated by a parabola, and is more reminiscent to the isotropic case (however, the dispersion carries an opposite sign to that of isotropic media).

1.7 Experimental observation of super-collimation

Large area PhCs such as that described in section 1.5 are interesting for their potential as macro-scale meta-materials. However, before experiments investigating super-collimation can be performed over macro-scales, it is first imperative that we characterize dispersive properties of this PhC. This enables the identification of the wavelength range over which our fabricated PhC supports

super-collimation.

1.7.1 Scattered light imaging of beam evolution

Evolution of the beam in the PhC is experimentally visualized by collecting light scattered through nano-scale roughness. Excitation of a TE-polarized propagating beam was achieved using a tunable laser source and a high numerical aperture (NA) lensed fiber and a polarization controller. The lensed fiber permits an initial beam full-width at half-maximum (FWHM) of 1.0 μm at the PhC input (corresponding to a wave-vector range of -0.1 to 0.1 (2π/a)). The scattered light from the PhC was imaged with an infrared (IR) vidicon camera (Figs. **1.8**d-f) for frequencies of 0.220, 0.233, and 0.245, $(2\pi/a)$ respectively (or wavelengths of 1590 nm, 1500 nm and 1430 nm). Each image is displayed over a 500 x 225 μm area located approximately 500 μm to the right of the input to avoid saturation of the camera due to scattered laser light generated through coupling. Each experimental image, was formed by averaging 300 IR images while tuning the laser over a 3nm spectral range (in 0.01nm steps). Spectral averaging of these images was found to be very effective for the reduction of laser speckle, which tends oscillate as a function of wavelength. In addition, a moving background subtraction algorithm enabled improved image contrast seen in Figs. **1.8**c-e.

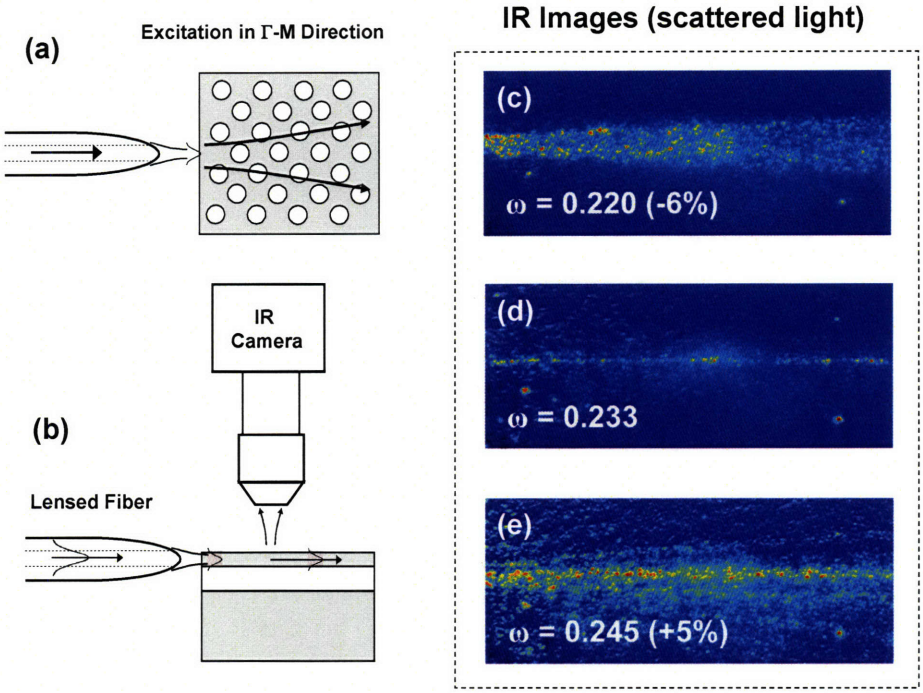

Figure 1.8: (a) Top view of experimental geometry. (b) Side view of experimental geometry. (c)-(e) experimental scattered images for frequencies of $\omega = 0.220, 0.233 and 0.245 (c/a)$ respectively.

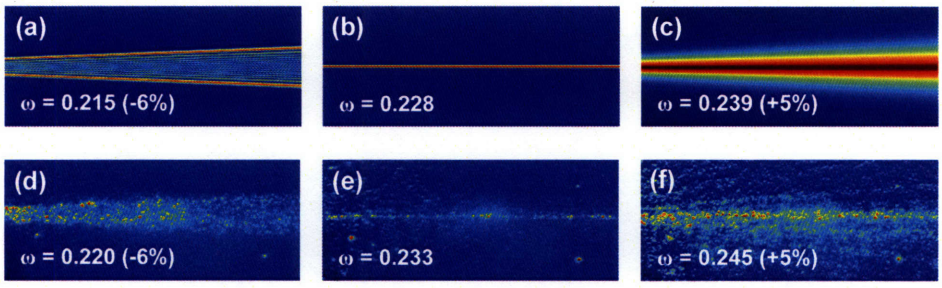

Figure 1.9: (a)-(c) simulated beam profiles for $\omega = 0.215, 0.228$ and 0.239 (c/a) respectively. (d)-(f) experimental scattered light images for comparable relative frequency shifts about the super-collimation wavelength. (d)-(f) correspond to frequencies of $\omega = 0.220, 0.233$ and 0.245 (c/a) respectively.

1.7.2 Comparison of experiment with theory

In examining these images, one clearly observes greatly reduced beam divergence at 1500 nm, suggesting a flat dispersion surface. It should be noted that simulations predict super-collimation wavelength of 1535 nm, while the fabricated system exhibits super-collimation at 1500 nm. This corresponds to a 2% discrepancy, well within the experimental uncertainty. For comparison with experiments, the simulations are displayed with comparable frequency shifts about the super-collimation frequency. Remarkable agreement in beam shape is seen for the low frequency beam evolution. Both BPM simulations and experiment display similar divergence angles and a sharp transverse roll-off expected as a result of the inflection points of the dispersion surface, although the rapid oscillations expected in the transverse beam profile of Fig. 1.9d are not resolvable by this imaging mechanism. At intermediate frequency (Figs 1.9) no beam divergence is resolvable, which is consistent with simulations. However, for higher frequencies, discrepancies between the theoretical and experimental beam evolution are seen.

1.8 Puzzle: beam break-up

Close inspection of Fig. 1.9c & f reveals beam break-up not captured in the theoretical model of a perfect PhC. We can see that the distinct beams eminate at angles between 3-6 degrees(see Fig. 1.10). Further experimental trials reveal that as the position of excitation is varied, the angles and character of beam

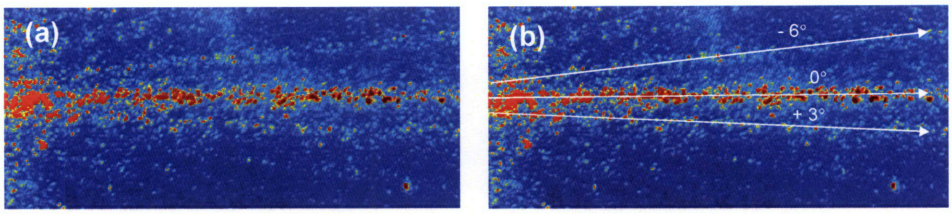

Figure 1.10: (a) Scattered light image for $\omega = 0.239$ (b) Same scattered light image with angles of fanning beams labeled

breakup can change drastically. It is also important to note that in many instances the fanning beams appear to originate at points within the bulk of the 2D PhC. This is a strong indication that beam breakup has little to do with the endfacet quality, since a phase transformation at the point of excitation would result in result in a similar point of origin for all beams. Therefore, we conclude that these additional spatial frequencies are being generated within the PhC, and the phase being imprinted on the beam has an irregular form, since the character changes as the input position changes.

1.8.1 Transverse k-vectors of beam breakup

One can use the computed dispersion surface in order to relate these angles of beam break-up to a realistic transverse wave-vector range. Since the direction of energy flow is obtained from the dispersion surface normal-vector [3], a reasonable estimate of the scattered wave-vector range can be obtained by computing the angle that the normal-vector makes with the direction of propagation (see for example Fig. 1.11).

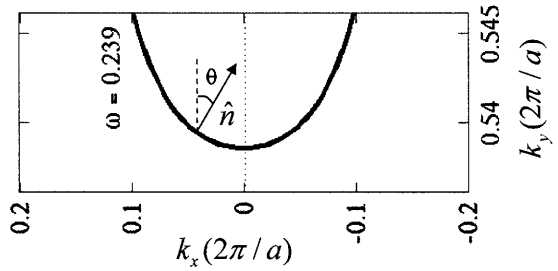

Figure 1.11: Plot of the dispersion surface for $\omega = 0.239$ with surface normal vector. The angle of propagation within the PhC can be determined from the angle that the surface-normal $\hat{n}$ makes with respect to direction of propagation for a given value of transverse wave-vector.

Through a fourth order polynomial fit*, a good approximation of the dispersion surface can be obtained, allowing us to relate the angles observed in beam break-up to meaningful transverse wave-vectors within the PhC. A polynomial retaining only 2^{nd} and 4^{th} order terms, as seen in Eq. 1.2, is sufficient to represent the dispersion surface over the wave-vectors of interest.

$$k_y(k_x) = k_{yo} + \alpha k_x^2 + \beta k_x^4 \tag{1.2}$$

Here $\alpha = 0.3\ (2\pi/a)^{-1}$ and $\beta = 15\ (2\pi/a)^{-3}$ for $\omega = 0.239$. From this fit, we find that angles of beam breakup (3 & 6 degrees) correspond to transverse wave-vectors of approximately 0.09 & 0.18 $(2\pi/a)$, which is well outside of the transverse wave-vector range at the input of the PhC ($\pm$ 0.10 $(2\pi/a)^{-1}$), indicating that only rapid spatial oscillations could be producing the beam break-up.

*Band structure computations and polynomial coefficients obtained by Mihai Ibanescu

1.9 Origin of beam break-up

Through examination of numerous types of experimental imperfections (i.e. layer thickness variations, interferometric lithography and endfacet quality), the only plausible mechanism by which wave-vectors could be generated within this range is through disorder resulting from lithographic variations. As a starting point, we consider some of the simplest types of defects that could be produced by lithographic variations. One can imagine that our fabricated photonic crystal would have a range of hole radii slightly displaced from their desired lattice sites due to lithographic roughness. These types of defects can be seen as perturbations on the perfect photonic crystal, resulting in slight phase shifts (of either sign) on the propagating wavefront and be expressed only at the lattice points. This is illustrated in Fig. 1.12. According to the sampling theorem, this discretely generated phase-noise can produce a continuum of spatial frequencies up to some maximum spatial frequency ($2\pi/a$) determined by the lattice spacing. Therefore, lithographically induced disorder appears to present a plausible explanation for this peculiar behavior. However, it is difficult to know what character disorder will really add to these propagating beams without detailed simulations.

Fortunately, the BPM method can be quite naturally tailored to incorporate the effects of disorder. In implementing simulations which more closely approximate the real photonic crystal, possessing some degree of disorder, we make the following observations: (1) Interference lithography produces a very uniform av-

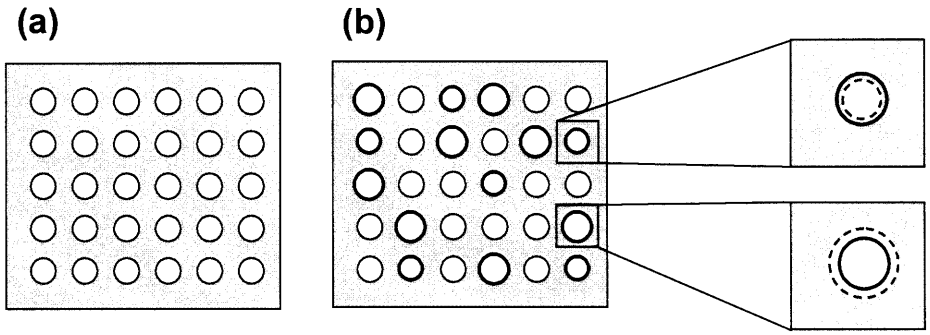

Figure 1.12: (a) An ideal photonic crystal, posessing holes of identical radius. (b) A disordered photonic crystal with the simplest type of defect, a variation in hole radius.

erage hole radius and lattice constant across the entire sample (2) lithographic roughness produces largely uncorrelated variations in hole dimension. Therefore the following correction to the physical model seems justified; light propagates in a material whose dispersion relation is determined by the perfect photonic crystal, and this material has small local (random phase) perturbations centered at the positions of the holes of the underlying PhC lattice. This model of disorder is easily incorporated into BPM simulations by distributing random phase changes at the lattice points with a phase amplitude estimated from the RMS fluctuation in hole radius.

1.9.1 Sensitivity analysis

In order to relate the simulated phase variations to a physically meaningful change in photonic crystal dimensions, we first perform a simple perturbative calculation. It is easy to examine the sensitivity of the propagation constant in

the Γ-M direction to change in radius through two band structure calculations[†]. Through two band structure computations at $\omega = 0.228$ for $r_1 = (0.30)a$ and $r_2 = (0.31)a$ we find the corresponding change in propagation constant $\Delta k_x = k_x|_{r_1} - k_x|_{r_2} = (0.01)2\pi/a$. This gives us some ability to estimate the phase change which results from a hole variation. If we have an isolated defect, the phase change incurred locally can be approximated as $\Delta\phi \approx \Delta k_x a$. Thus, the phase sensitivity to the change in hole radius over a single lattice constant is $\Delta\phi/\Delta r \approx 1.0$ (Deg/nm) for our photonic crystal system.

1.9.2 Evidence of disorder

The SEM seen in Fig. **1.13** provides some clue as to the magnitude of the hole size variation in the fabricated device through the measurement of a small number of holes in our PhC system. This image, obtained with a LEO scanning electron microscope, appears to indicate that the hole dimension could be changing by a couple of nanometers. Although, field distortion may account for some of these apparent variations, it is clear that hole morphology changes slightly from hole to hole. Unfortunately, such morphological changes are more difficult relate to a meaningful phase change, and would require rigorous Green's function methods to model properly [**16**].

[†]Band structure calculations performed by Mihai Ibanescu

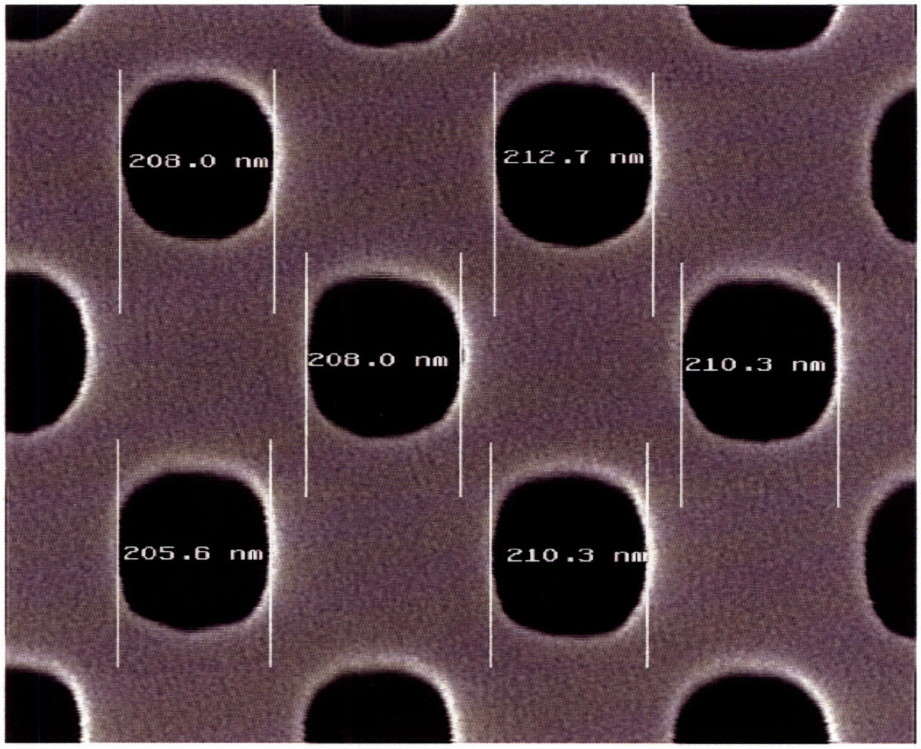

Figure 1.13: Scanning electron micrograph of PhC device under study. Image obtained with the LEO scanning electron microscope. [SEM image by Sheila Tandon]

1.9.3 A simple first simulation example

In this section, we use the sensitivity analysis and SEM measurement of the previous sections as a guide to perform our first simulations of the beam evolution within a disordered photonic crystal. Applying the BPM method, with the inclusion of random phase changes at the lattice sites (i.e. disorder), we have the results seen in Figs. **1.14** g-i. In this first simulation example, we consider only the simplest type of perturbations on the PhC lattice in the form of a hole

radius variation. This simulation incorporates a 0.6 degree rms phase change. According to the sensitivity analysis of the previous section, this corresponds to $\sim$ 0.6 nm rms radius variation. It is interesting to note that for both $\omega = 0.215$ and $\omega = 0.228$ the character of the evolving beams isn't drastically altered despite the fact that high spatial frequencies are being generated by the disorder. However, for $\omega = 0.239$ the creation of new spatial frequencies is obvious, and is manifest as fanning of the beam, more similar to the experimental images. This agreement further supports the hypothesis of disorder as the source of nonidealities in the PhC under study.

In comparing Figs. **1.14** f&i , however, a key difference between experiment and simulations can be seen. The experimental beam break-up appears to produce somewhat better defined, or narrower beams, shedding more power to large wave-vector range. There could be numerous causes for the difference in character. However, before any further complexities are assumed in our model, it is instructive to first investigate how the character of this beam break-up is effected by the amplitude of the phase noise, and the dimension of the propagating beam.

1.10 Conceptual picture for beam breakup

Through the simulations of the previous section, we have established plausibility of disorder as the cause for beam breakup. However, until we develop some conceptual understanding of this process we have little to guide us in our

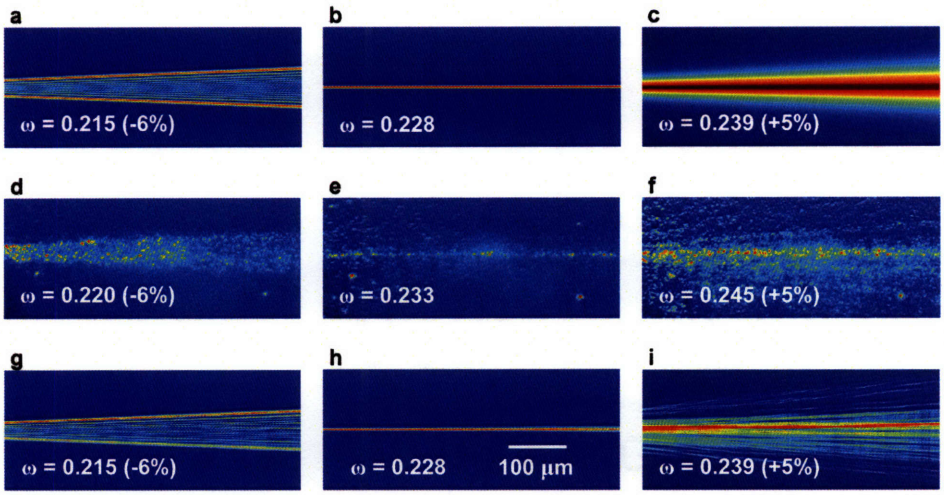

Figure 1.14: Theoretical beam evolution generated through BPM for ω = 0.215, 0.228 and 0.239, to be compared with experiment (d-f). d-f, Top view experimental images of light travelling through the PhC for $\omega = 0.220$, 0.233 and 0.245 (1590 nm, 1500 nm and 1430 nm) obtained through light scattered from the beam with an IR camera. Each image is approximately 500 μm to the right of the point of excitation. g-i, BPM simulations of the beam evolution (for ω = 0.215, 0.228 and 0.239) including effects of disorder.

simulations. In this section we seek to develop a basic conceptual framework through which we can understand the process of beam evolution in the presence of discrete disorder. To better understand propagation in a disordered medium, we would like to know several things. For instance, what dictates (1) the amplitude and (2) the bandwidth of a phase fluctuation that develop in the beam as it propagates? This is important since both will dictate the angles and magnitude of beam break-up. It is also important to understand how (3) spatial dispersion and (4) beam dimension effect this process? In our first attempt to address these questions, we make some greatly simplifying assumptions about

the beam evolution so that we can develop a tractable picture for the process of beam breakup.

1.10.1 Phase evolution in the absence of diffraction

We begin analyzing the effect of disorder on a propagating wavefront by neglecting the effects of diffraction. This is an interesting exercise since it provides a zero-order estimate the length-scale over which a propagating beam will accumulate a significant phase fluctuation. In the absence of diffraction, each point in the wavefront of a beam can be treated as a ray traversing the photonic crystal. As before, the photonic crystal can be viewed as a uniform medium, except at the lattice points where deviations from the perfect hole dimensions result in small phase 'kicks' of rms magnitude δ. See for example Fig. **1.15**a. Since the kick at subsequent positions is additive we can see that the standard deviation (σ_ϕ) of the phase at any point in the propagating wave-front will be dictated by the number of lattice points (N) that a given ray in the beam traverses. Therefore, the phase evolution can be likened to a random walk in phase, and is given approximately by $\sigma_\phi = \delta\sqrt{N}$. A simple example of the phase evolution through this random walk can be seen in Figs. **1.15**c-d.

1.10.2 Magnitude of fluctuation consistent with breakup

Now that we have some means of estimating the magnitude of phase fluctuations in the beam, it is instructive to estimate the magnitude in phase change required to significantly alter the beam evolution. Through the process of beam-

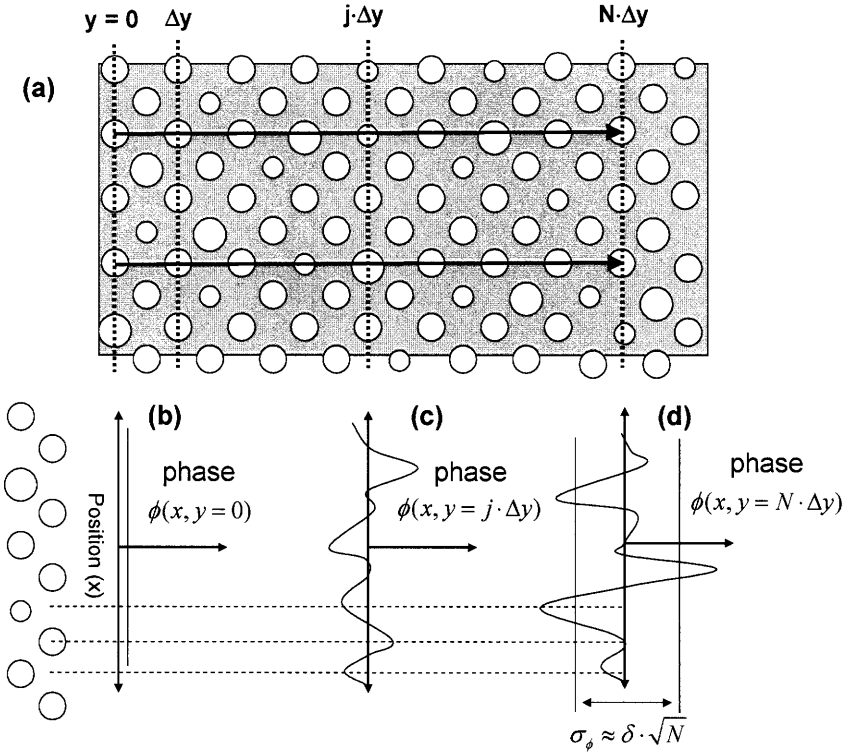

Figure 1.15: (a) Diagram illustrating a beam (in absence of diffraction) propagating along the $\Gamma - M$ direction in disordered photonic crystal. (b)-(d) are plots of characteristic phase profile for beams at positions y = 0, $j\Delta y$ and $N\Delta y$ respectively. In the absence of diffraction, the phase kick generated at each lattice point is additive resulting in a standard deviation in the phase front of $\sigma_\phi \approx \delta\sqrt{N}$

breakup, we observe the creation of distinct beams emanating from the excited beam in experimental images. This behavior could be explained by side-band generation through a phase modulation of our beam. In order to estimate the magnitude that is crucial for significant side-band generation (i.e. like that seen in experimental images), we can consider a single spectral component of this phase modulation. Through use of the Bessel identity given in Eq. 1.3, we can see that a sinusoidal phase modulation can be expressed as a superposition of

plane-waves [13].

$$\exp\left[i\cdot\theta\sin(kx)\right]=\sum_{m=-\infty}^{\infty}J_m(\theta)\exp(i\cdot kx\cdot m) \tag{1.3}$$

Here, $J_m(\theta)$ is a Bessel function of the first kind. Through evaluation of $J_m^2(\theta)$ as a function of θ, it is clear that a significant fraction of the power (~40%) is shed to sidebands only when $\theta \sim 1$ radian. Therefore, we can loosely define an important length-scale, L_{crit}, as the distance over which the phase front of a given ray will accumulate a phase shift of $\sigma_\phi \approx \phi_{crit} \approx 1$. The critical-length then becomes

$$L_{crit} \approx N\Delta y \approx \Delta y\cdot\left(\frac{\phi_{crit}}{\delta}\right)^2. \tag{1.4}$$

In the above expression, Δy is taken to be the separation between scattering sites in the direction of propagation.

1.10.3 Incorporating the effects of diffraction

In the absence of diffraction, this simple estimate presented in section **1.10.1** leads us to believe that the phase fluctuations that accumulate in a beam can be of arbitrary spatial frequency (i.e. as high as $(2\pi/a)$). However, when we include the effects of diffraction, this is clearly not the case. This is because diffraction tends to result in much more rapid dispersion for high spatial frequencies than low frequencies, resulting in a band-limiting of the phase noise imprinted on the beam. This band limiting process is illustrated more clearly through Figs. **1.16** which depict the evolution of a beam with an initially broadband spatial

phase-noise. After propagation over a single diffraction length, due the rapid diffraction of the higher k-vector components, the spatial phase only retains oscillations which are comparable in spectral content to the beam. Rigorous justification for this approximation is given in appendix B.

So far, our analysis tells us that the spatial evolution of the beam within the photonic crystal will be dictated by both phase noise creation and diffraction. To first order, we treat the phase noise as an additive random process, and diffraction as a band-limiting process. Therefore, we can form some conceptual picture of this complicated beam evolution by lumping the phase noise creation and spatial dispersion of a step into separate operations, and repeating this process. Through this picture it seems clear that there is likely to be a frequency bandwidth over which the phase-noise is likely to grow.

A more quantitative idea of how phase oscillations in the beam profile will be band-limited can be formed if we can make use of the definition of the diffraction length given in Eq. 1.1. This expression tells us, at what point, a Gaussian beam of width w will begin to disperse. Since the transverse wave-vector spread of a beam can be related to it's diffraction length, we can form an estimate of the filtering bandwidth produced by the process of diffraction over a single diffraction length. Using the uncertainty relation for Gaussian beams, $w \cdot \Delta k_x = 2$, the diffraction length can be expressed quite generally as

$$L_d = \frac{w^2}{2\alpha} = \frac{2}{\Delta k_x^2 \cdot \alpha}. \tag{1.5}$$

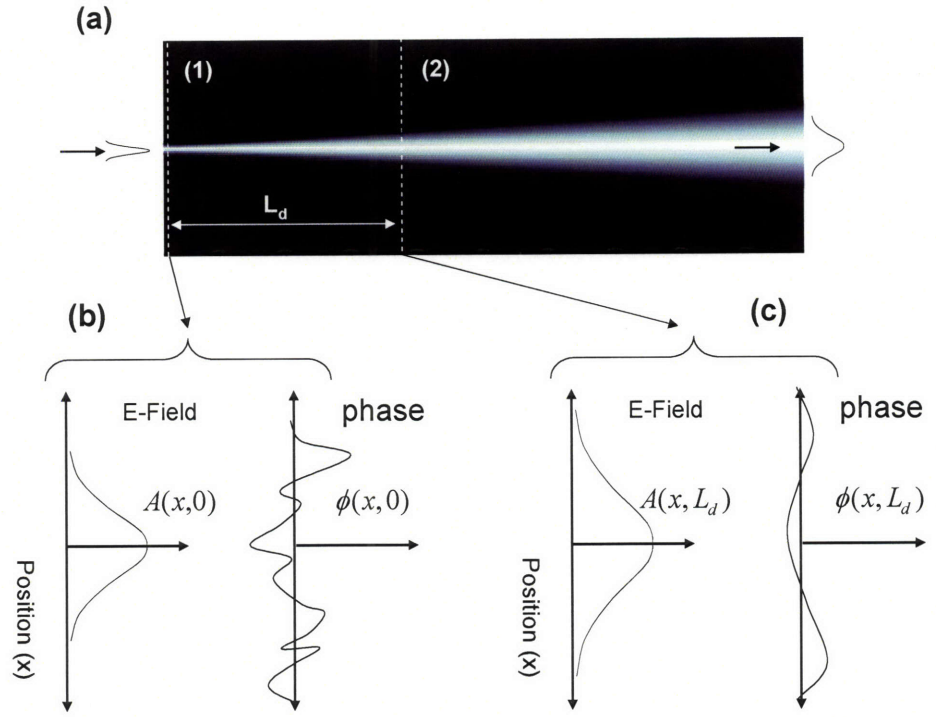

Figure 1.16: Diagram illustrating the effects of diffraction on phase noise imprinted on a propagation Gaussian beam (a) Gaussian beam evolution over diffraction length L_d. (b) Plots of the Gaussian beam and phase profiles at start position (1). Here the phase profile is assumed to be broad-band (c) Plots of the beam and phase profiles after propagation over a distance L_d, indicated by position (2). Note that the phase oscillations within the beam are of reduced bandwidth.

Here w and Δk_x are the beam waist radius in space and in the transverse wave-vector, and $\alpha \equiv \frac{d^2 k_x}{dk_y^2}|_{k_y=0}$, the curvature of the dispersion surface. The bandwidth limitation placed on the phase noise after a single diffraction length is traversed is illustrated in Fig. 1.16. Solving for Δk_x of Eq. 1.5 approximates the bandwidth in this case. However, the bandwidth limitation placed on the phase will clearly scale with the distance the beam is allowed to evolve. Since

this distance needn't be the diffraction-length, we can replace L_d with the Δl. Solving for the bandwidth of phase oscillations, Δk_x, at an arbitrary distance, Δl, then yields

$$\Delta k_x = \sqrt{\frac{2}{\Delta l \cdot \alpha}}. \tag{1.6}$$

If we assume that the observed beam breakup occurs as a result of phase fluctuations which approach ~ 1 radian, beam breakup could only occur after a distance of L_{crit} is traversed. Therefore, substituting L_{crit} for Δl of Eq. **1.6** yields first order approximation of the expected k-vector range produced by beam breakup.

$$\Delta k_x = \left(\frac{\delta}{\phi_{crit}}\right) \cdot \sqrt{\frac{1}{\Delta y \cdot \alpha}}. \tag{1.7}$$

From the above expression, we see that the maximum transverse wave-vector of diffracted orders scales linearly with the magnitude of the rms phase kick, δ, at each lattice point. It is also interesting to note that as spatial dispersion (α) decreases, so does the maximum bandwidth of the sidebands. Assuming that Eq. **1.8** is approximately correct, the spectral content of the diffracted beams would be describable by a convolution of the beam initial wave-vector spread, $A(k_x, 0)$, with that of the phase noise imprinted on the beam, $N(k_x)$. To first order, the wave-vector spread generated by the phase noise can be expressed as a quadrature sum of their spectral widths, or as

$$\Delta k_{x,tot} \approx \sqrt{\Delta k_{x,scatt}^2 + \Delta k_{x,init}^2}. \tag{1.8}$$

It is important to note that the above analysis is very simplistic, and would only be valid in describing the beam evolution in the first few diffraction lengths, since higher order scattering processes will complicate the beam evolution very quickly. Nonetheless, both trends will be interesting to examine through simulations.

1.11 Computational study of beam evolution

The simple analysis presented in section **1.10** leads us to expect that higher transverse k-vector components will be created as δ is increased. As noted in the first simulation example of section **1.15**, $\delta = 0.6$ degrees appears to underestimate the power shedding that is observed in experiment. Using the simple conceptual analysis as our guide, we perform simulations for $\delta = 1, 3.3$ and 5 degrees. Some characteristic simulation results can be seen in Figs. **1.17**-**1.19**. Further examples are given in appendix **B**.

In examining these results, we see varying degrees of beam distortion as δ is increased. For $\delta = 1$ degree, comparison with the beam evolution in the absence of disorder reveals that the beam profile is only slightly distorted from its original form. Slightly more power is shed to larger angles, and slow oscillations are apparent in the beam center, but the beam spans a similar wave-vector range with and without disorder. For $\delta = 3.3$ degrees, the beam profile is drastically altered, shedding a much more power to a larger transverse wave-vector range. Interestingly, scattered beams appear much more localized,

and discrete in appearance. Despite the stronger scattering, there remains a significant amount of power centered at $k_x = 0$ (zero order). For $\delta = 5$ degrees, we see the most drastic shedding of power to a large transverse wave-vector range. There remains little power at zero order, and the several broken beams of comparable intensity span angles which are more than twice that seen without disorder. At first glance, the simple analysis performed above appears to capture the correct behavior, however a quantitative trend is difficult extract from images of this form.

Although simulations for δs of 3.3 and 5 degrees produce localized broken beams which are discrete in appearance, comparison with Fig. **1.14** reveals that both aren't consistent with experiment. The scattered light image for $\omega = 0.245$ (Fig. **1.14**f) shows a significant amount of power in the zero order. This is clearly absent for $\delta = 5$ degrees, meaning that the PhC under study possesses a smaller degree of disorder, which is likely closer to $\delta = 3.3$ degrees.

In testing this hypothesis we can perform simulations for comparison with experimental images Fig. **1.14**d-e. Any divergence from the experiment at the frequencies $\omega = 0.220$ and 0.233 may allow us to further pinpoint the range of disorder that our PhC exhibits. Some characteristic simulations for $\delta = 1, 3.3$ and 5 degrees can be seen in Figs **1.20**-**1.25** for $\omega = 0.228$ and 0.215. For $\omega = 0.228$ we see that the beam evolution is virtually unaltered for $\delta = 1, 3.3$ while it is significantly distorted for $\delta = 5$. A similar trend is seen for $\omega = 0.217$.

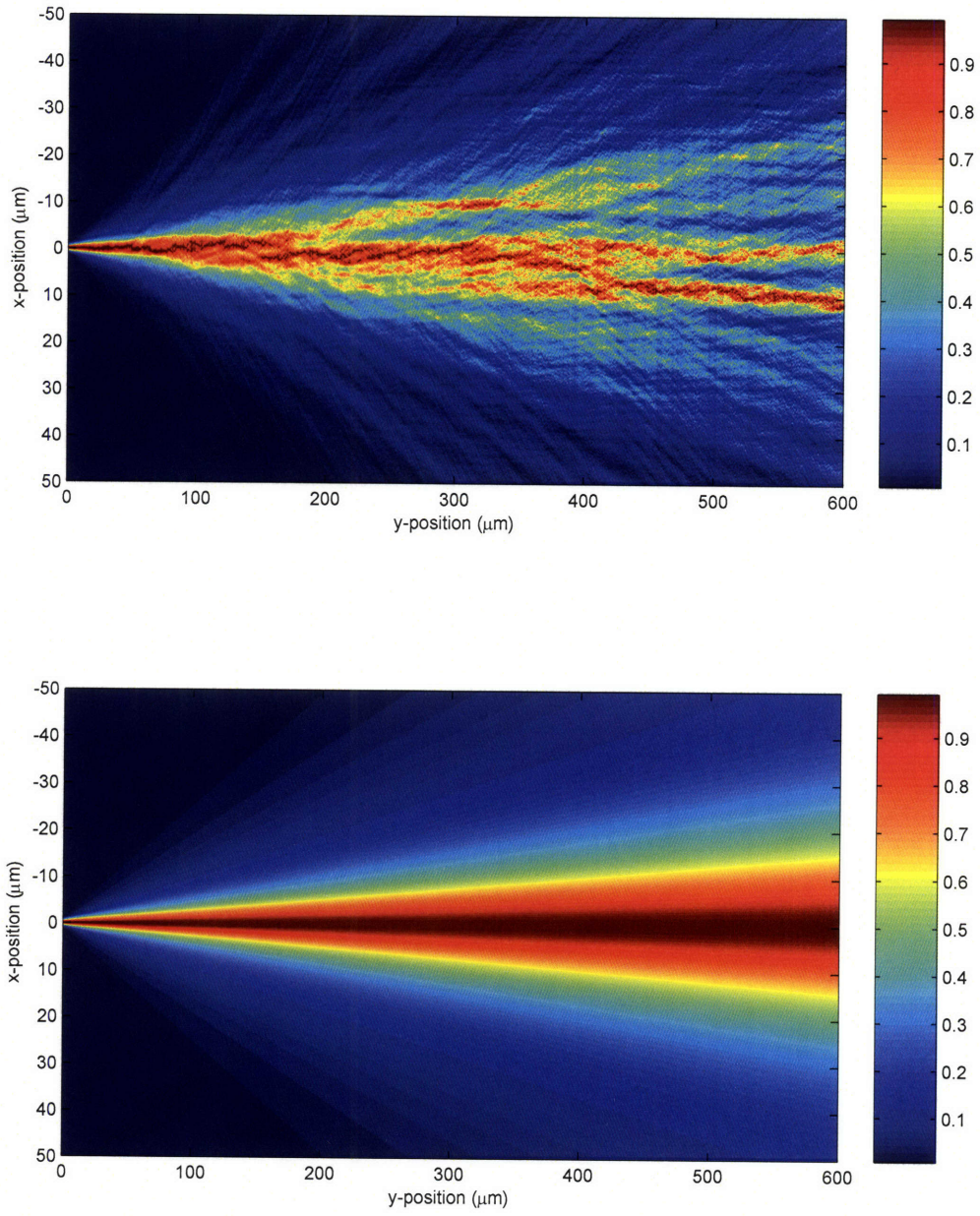

Figure 1.17: Theoretical beam evolution generated through BPM for $\omega = 0.239$. For comparison, BPM simulations with disorder (upper) and without disorder (lower) are displayed. Here $\delta \approx 1$, and a Gaussian waist radius of 0.85 microns (or FWHM of 1 micron) are used. Simulations are displayed over a 100 x 600 micron area.

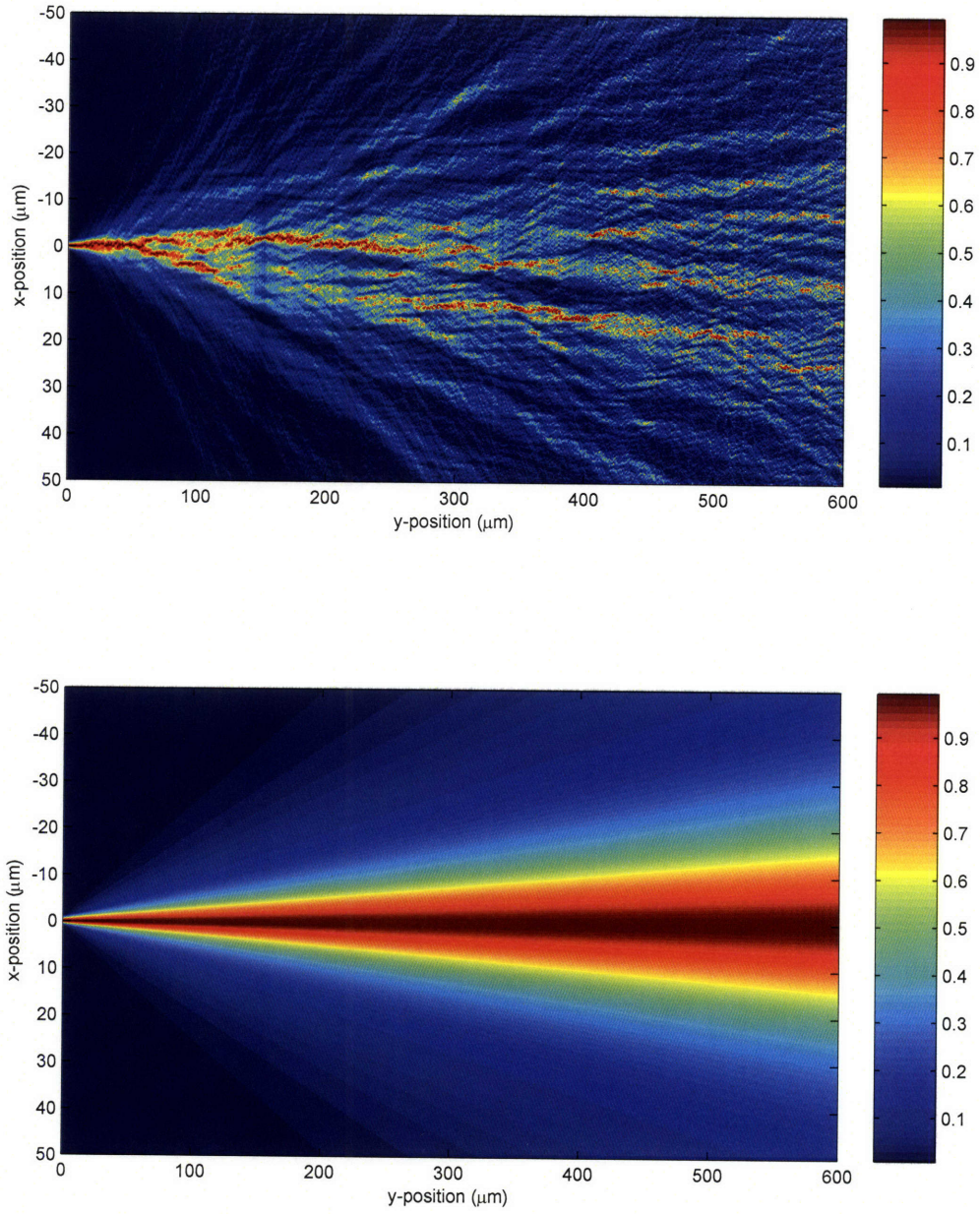

Figure 1.18: Theoretical beam evolution generated through BPM for $\omega = 0.239$. For comparison, BPM simulations with disorder (upper) and without disorder (lower) are displayed. Here $\delta \approx 3.3$, and a Gaussian waist radius of 0.85 microns (or FWHM of 1 micron) are used. Simulations are displayed over a 100 x 600 micron area.

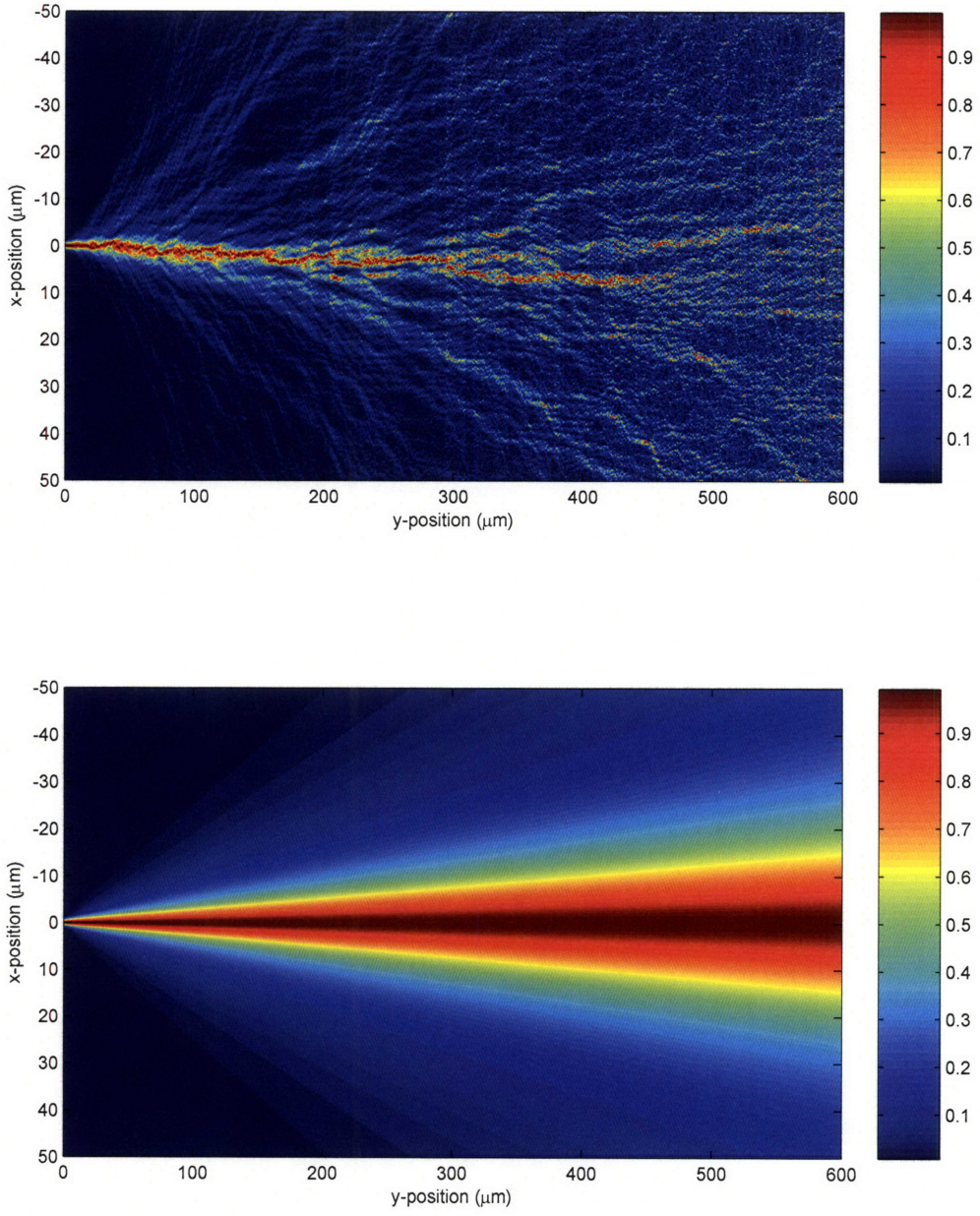

Figure 1.19: Theoretical beam evolution generated through BPM for $\omega = 0.239$. For comparison, BPM simulations with disorder (upper) and without disorder (lower) are displayed. Here $\delta \approx 5$, and a Gaussian waist radius of 0.85 microns (or FWHM of 1 micron) are used. Simulations are displayed over a 100 x 600 micron area.

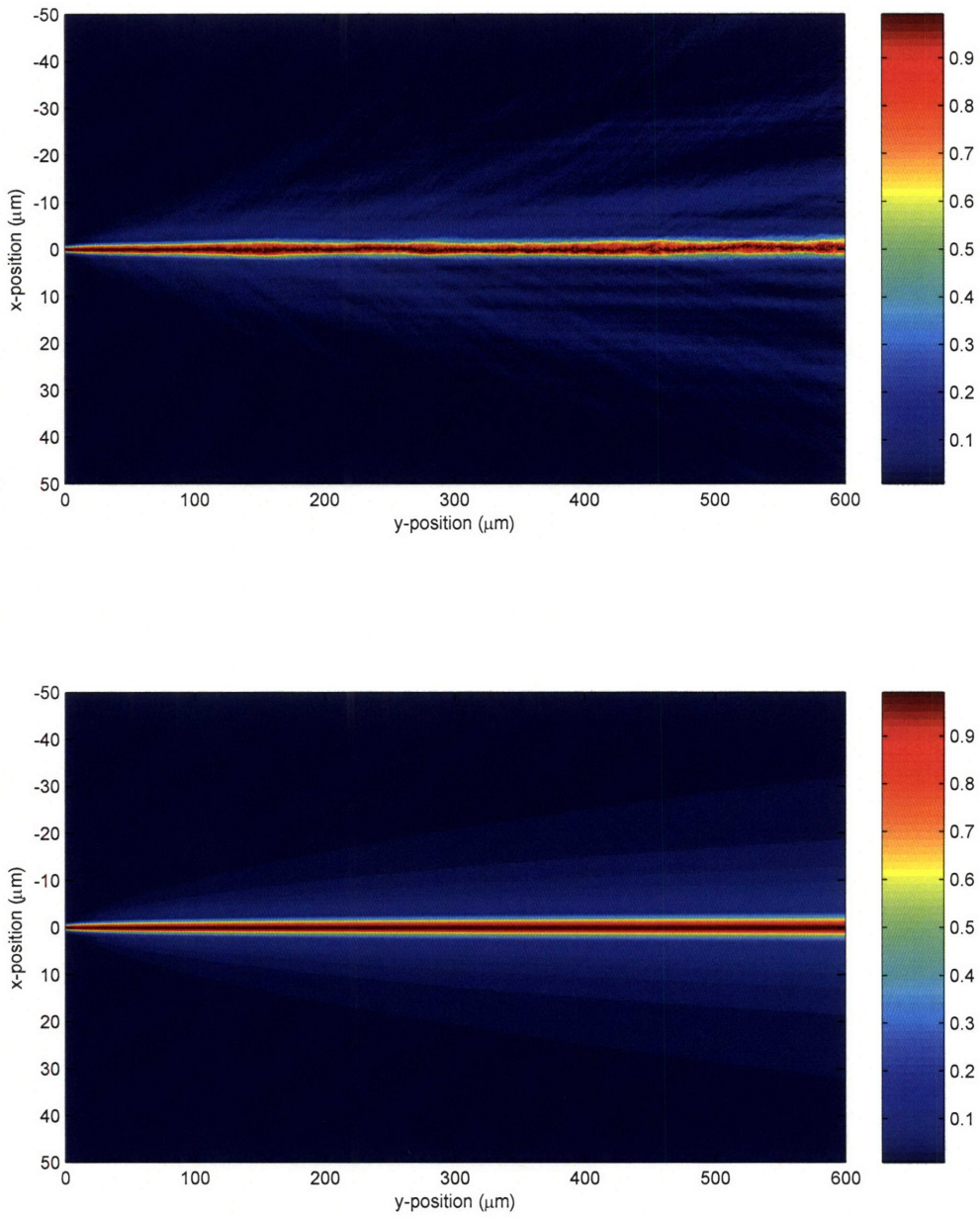

Figure 1.20: Theoretical beam evolution generated through BPM for $\omega = 0.228$. For comparison, BPM simulations with disorder (upper) and without disorder (lower) are displayed. Here $\delta \approx 1$, and a Gaussian waist radius of 0.85 microns (or FWHM of 1 micron) are used. Simulations are displayed over a 100 x 600 micron area.

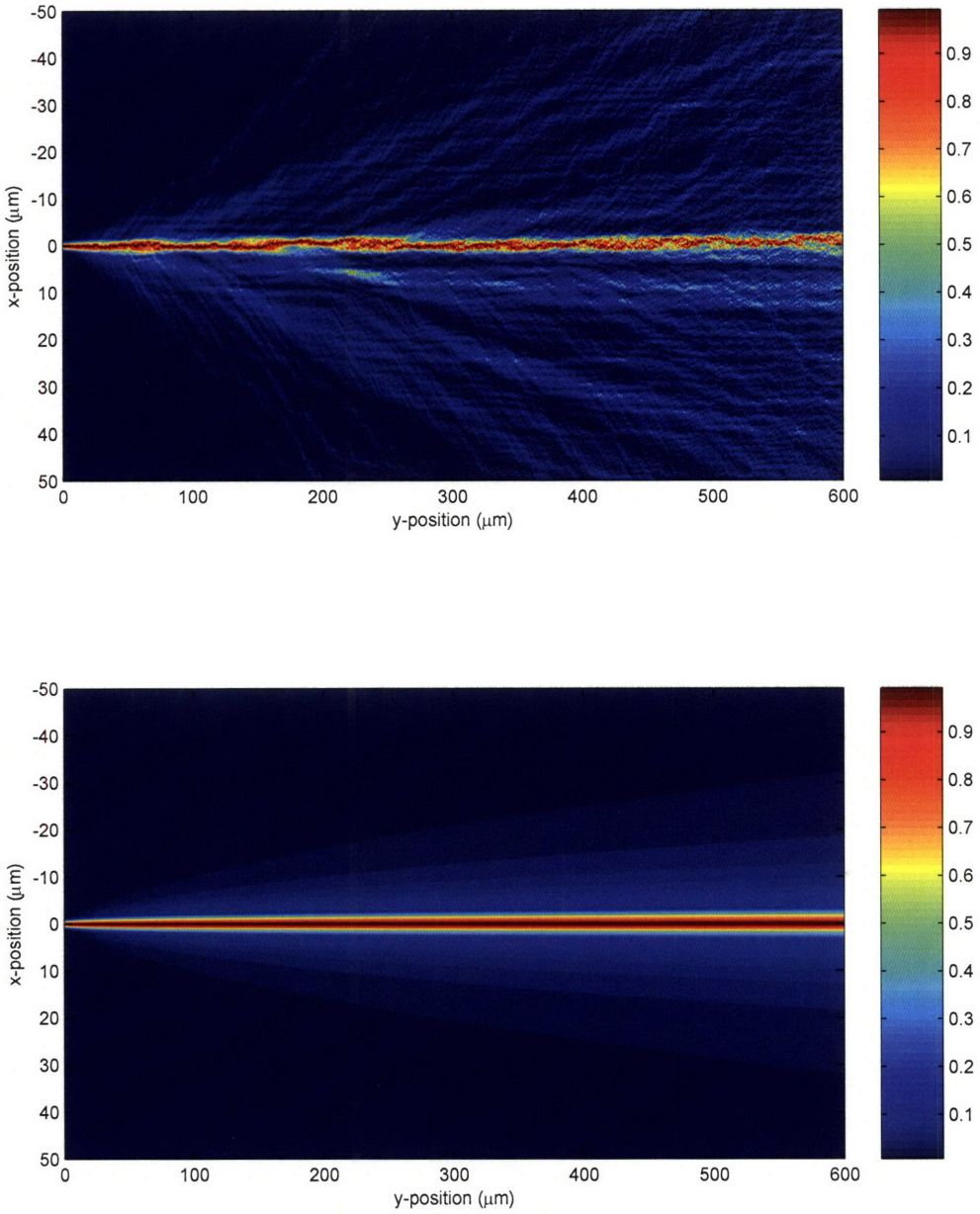

Figure 1.21: Theoretical beam evolution generated through BPM for $\omega = 0.228$. For comparison, BPM simulations with disorder (upper) and without disorder (lower) are displayed. Here $\delta \approx 3.3$, and a Gaussian waist radius of 0.85 microns (or FWHM of 1 micron) are used. Simulations are displayed over a 100 x 600 micron area.

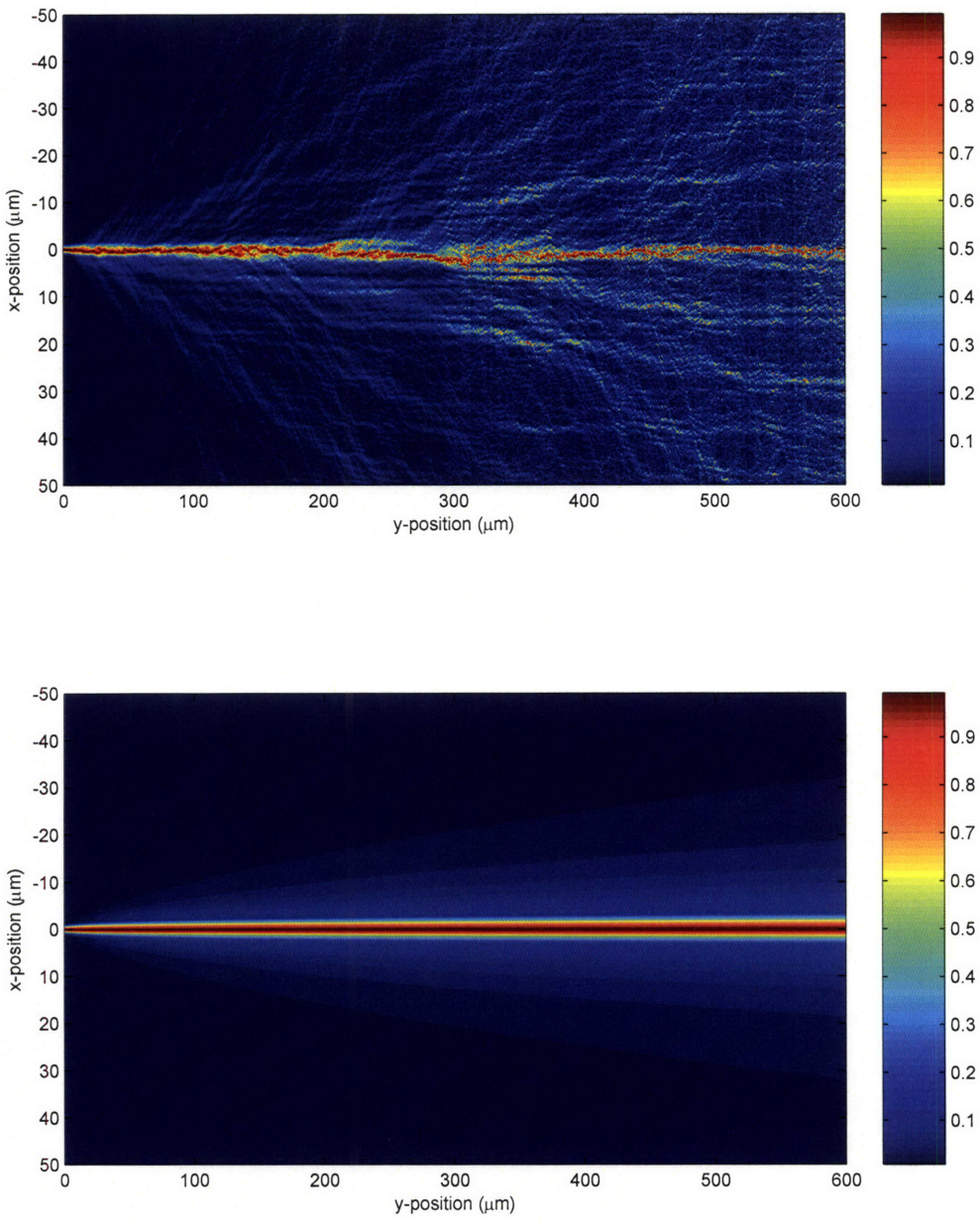

Figure 1.22: Theoretical beam evolution generated through BPM for $\omega = 0.228$. For comparison, BPM simulations with disorder (upper) and without disorder (lower) are displayed. Here $\delta \approx 5$, and a Gaussian waist radius of 0.85 microns (or FWHM of 1 micron) are used. Simulations are displayed over a 100 x 600 micron area.

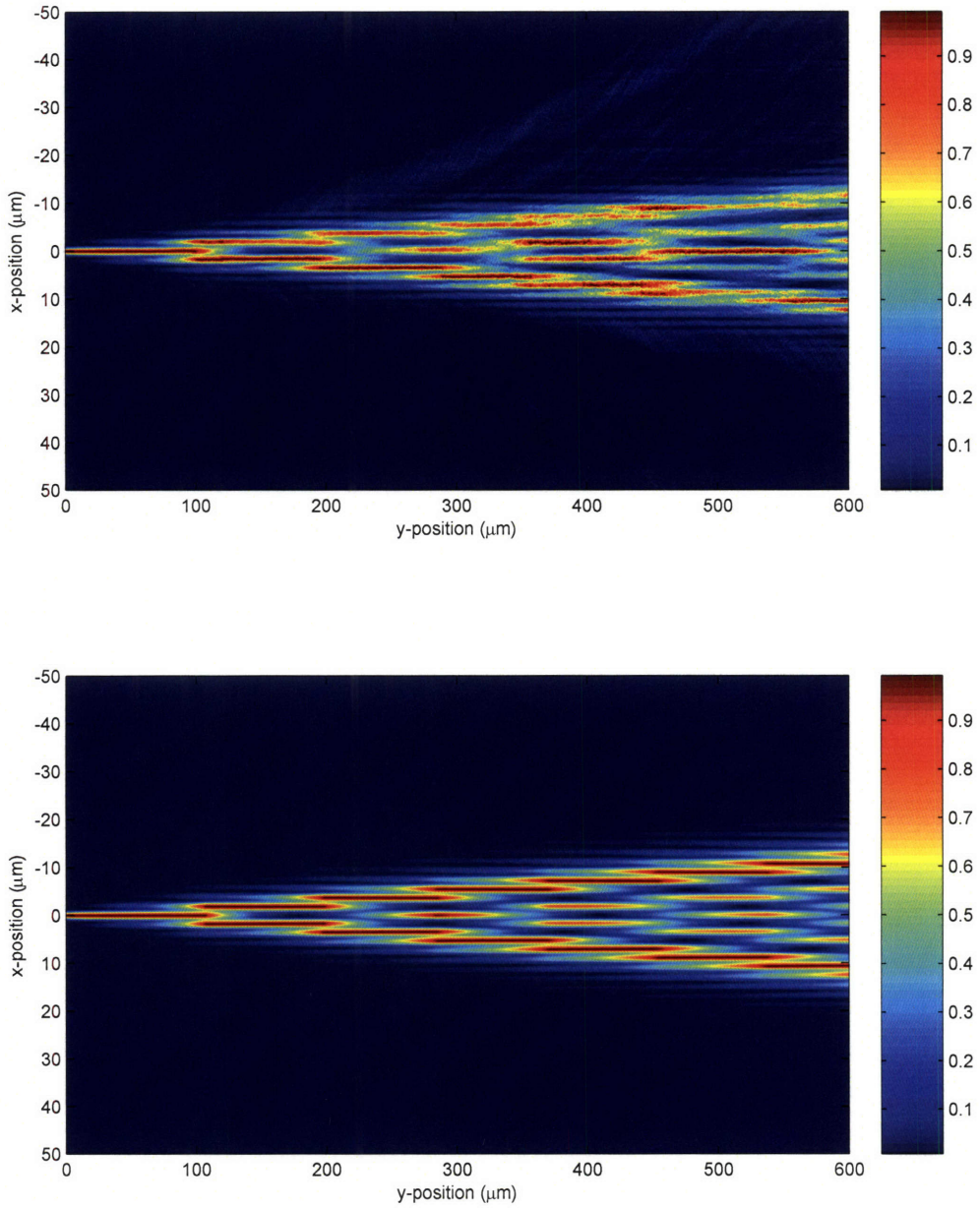

Figure 1.23: Theoretical beam evolution generated through BPM for $\omega = 0.215$. For comparison, BPM simulations with disorder (upper) and without disorder (lower) are displayed. Here $\delta \approx 1$, and a Gaussian waist radius of 0.85 microns (or FWHM of 1 micron) are used. Simulations are displayed over a 100 x 600 micron area.

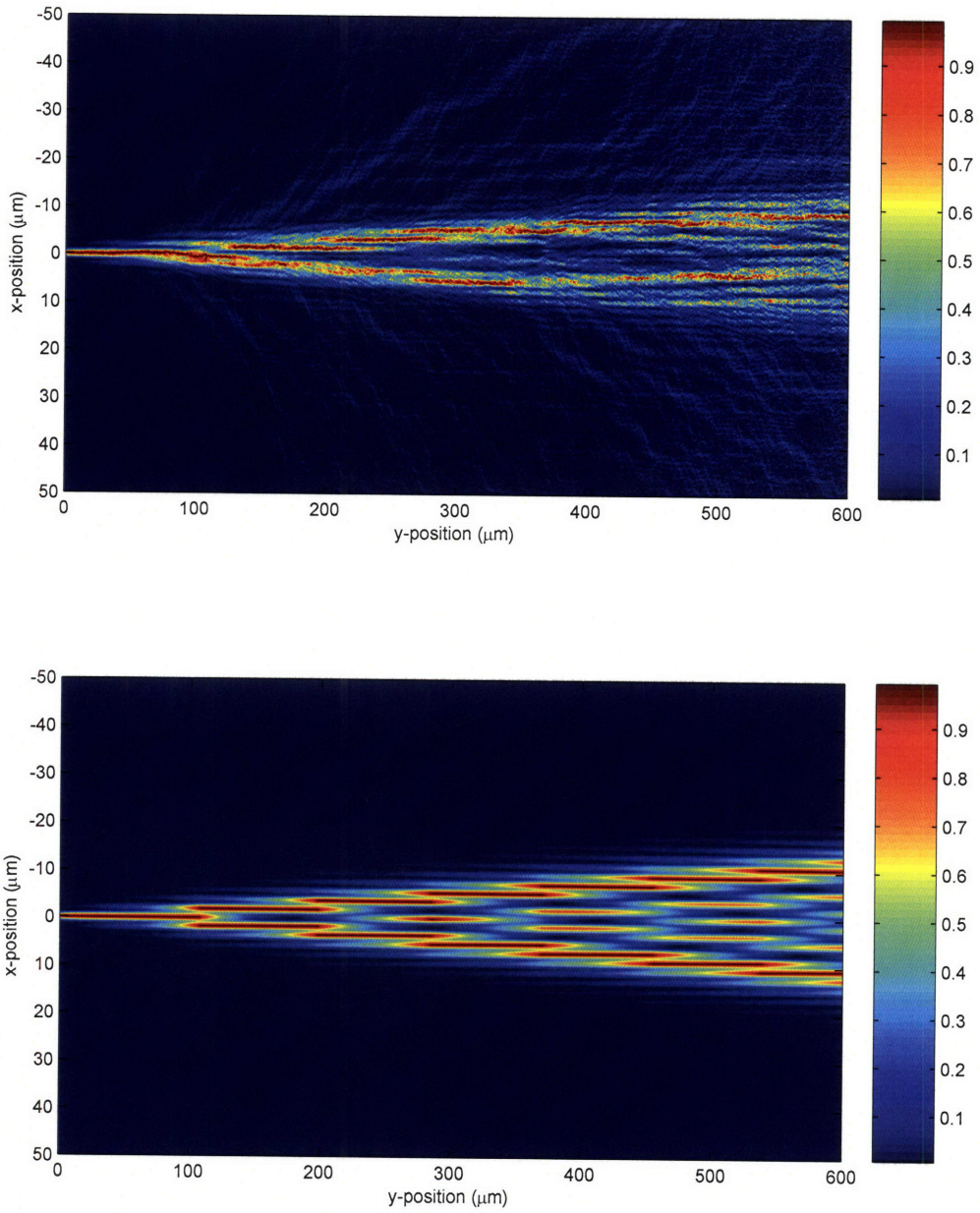

Figure 1.24: Theoretical beam evolution generated through BPM for $\omega = 0.215$. For comparison, BPM simulations with disorder (upper) and without disorder (lower) are displayed. Here $\delta \approx 3.3$, and a Gaussian waist radius of 0.85 microns (or FWHM of 1 micron) are used. Simulations are displayed over a 100 x 600 micron area.

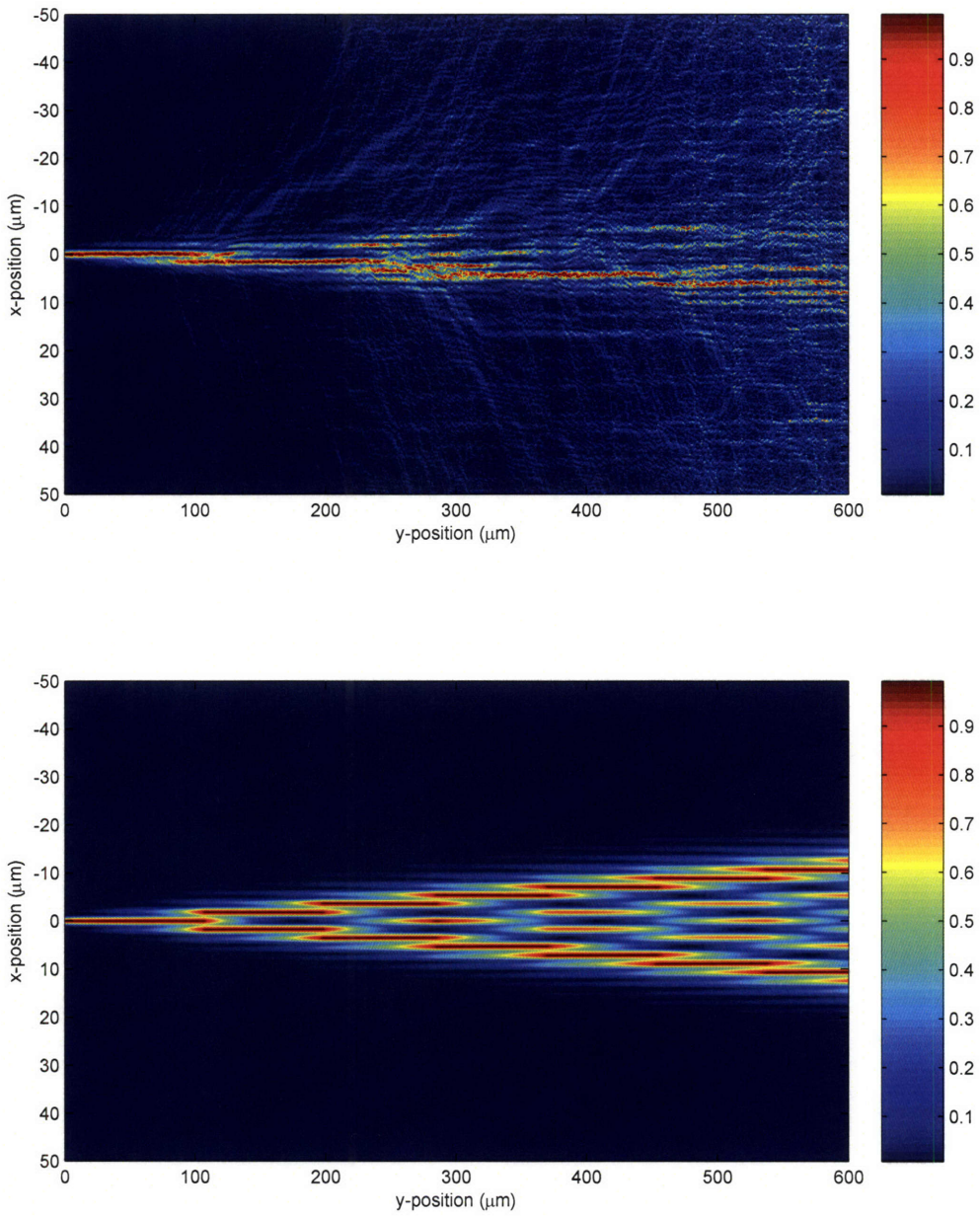

Figure 1.25: Theoretical beam evolution generated through BPM for $\omega = 0.215$. For comparison, BPM simulations with disorder (upper) and without disorder (lower) are displayed. Here $\delta \approx 5$, and a Gaussian waist radius of 0.85 microns (or FWHM of 1 micron) are used. Simulations are displayed over a 100 x 600 micron area.

1.12 Spectral content of beam break-up

The basic analysis of disorder and simple assumptions made in section **1.10** would lead us to believe that the broken beams could eminate at a continuum of angles up to some maximum angle dictated by the magnitude of δ. However, numerous simulations of the type seen in Figs. **1.17-1.19** lead one to wonder whether this process gives preference to a set of angles. To investigate this further, we run a series of simulations over a 600 micron distance. The averaged the power spectrum of a vertical intensity stripe at the output over 80 runs. These simulations, performed for values of $\delta = [1.33, 1.67, 2.0, 2.5, 3.33, 4.0]$ degrees, can be seen in Fig. **1.26**, and give us some ability to estimate the angles of beam breakup if we assume that all beams emanate from a similar point of origin.

Although disorder gives rise to a set of broken beams which are discrete in appearance for individual trials, averaging over a statistically significant number of trials washes out the discrete appearance in k-space. In examining the spatial frequencies consistent with beam break-up we find that disorder related scattering results in a pedestal which closely approximates an exponential in the power-spectrum. In certain instances, oscillations form in the pedestal, although, it is difficult to determine whether these might be an indication of resonant scattering in particular directions since fluctuations in the point of origin and higher order scattering processes may wash out any such information.

Nevertheless, it is interesting to use these data to develop a more quantita-

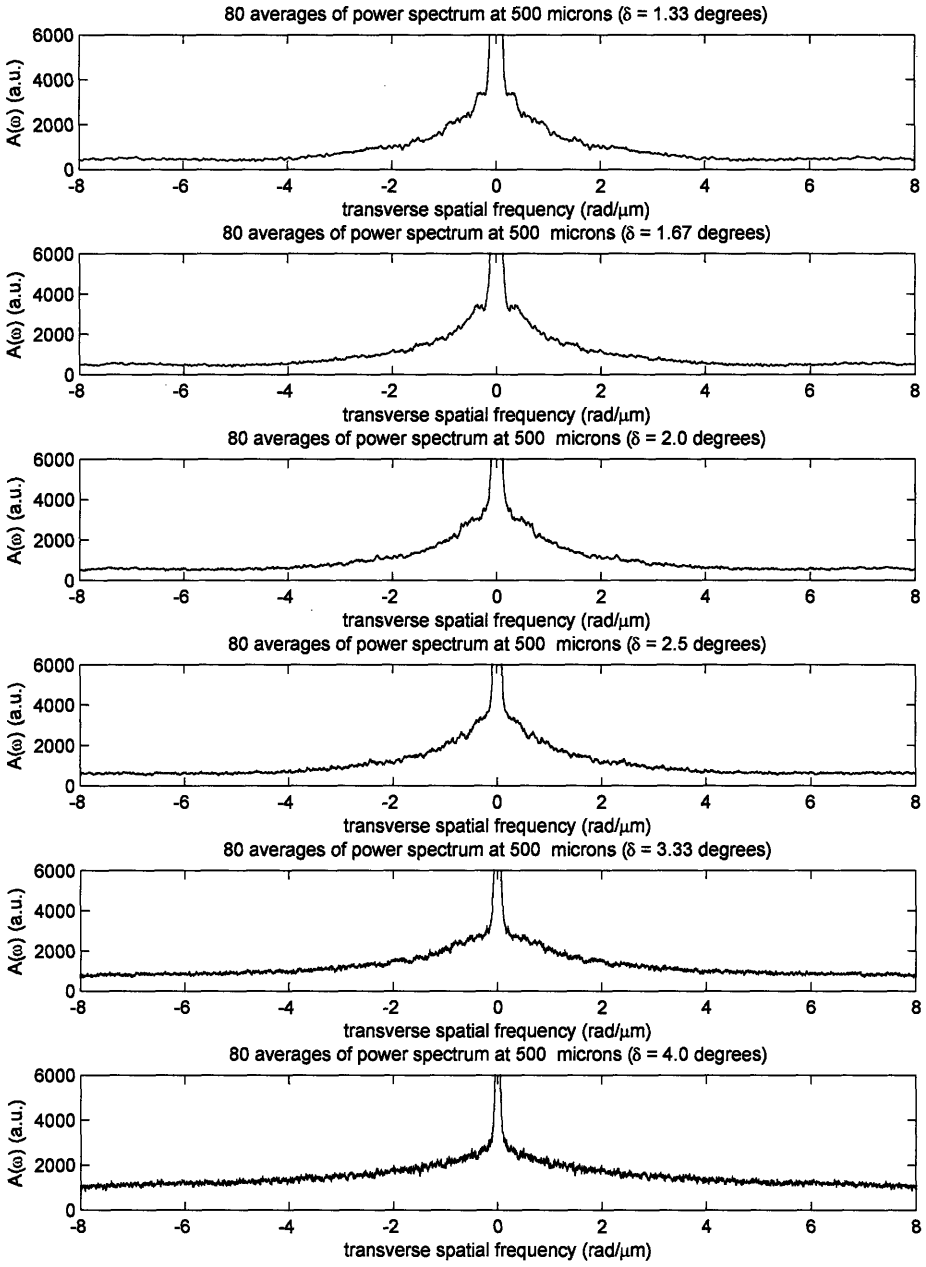

Figure 1.26: Plots of the computed intensity power-spectrum averaged over 80 separate BPM runs. Each spectrum above is obtained by averaging the FFT of the intensity produced by a vertical stripe of pixels the output of a simulation run such as those shown in the previous section.

tive understanding of how disorder related scattering creates new k-vectors, and how it varies with δ. Through exponential fits of each pedestals seen in fig **1.26** we find that the pedestal increases by $\sim$2 in bandwidth over this range of δs, and approximately follows a quadratic trend with δ. This is roughly consistent with the estimate described in section **1.10**.

Perhaps the most interesting thing about this trend is that it points to the possibility that a statistically significant number of beam break-up images (such as that seen in Fig. **1.10**) could allow us to accurately assess the degree of disorder that the PhC possesses. More insightful analysis would require a more rigorous treatment of the beam evolution. This presents a potentially interesting new direction for disorder studies in meta-materials.

1.13 Long distance super-collimation

So far, we have used scattered light imaging techniques to identify the dispersive properties over distances between 500-1000 μm. We have also identified non-idealities, such as lithographically induced disorder, which drastically effect the beam evolution at frequencies above the super-collimation wavelength. Since numerous proposed applications for super-collimation require propagation over large distances, the study of meta-material properties at larger length-scales is highly relevant. As described in section **1.5**, through interferometric lithography, device dimensions of centimeter-scale are quite accessible, affording us the unique opportunity to study meta-material losses and uniformity at these scales.

1.13.1 Experimental results

A top-view image of scattered light (similar to those in Figs. **1.8**c-e) from the PhC is shown in Fig. **1.27**a, over a 0.3 cm long sample[‡], providing a good first indication of the device uniformity. Super-collimation is apparent over the entire length without any resolvable beam divergence, for $\lambda = 1500$ nm. To further quantify the spatial evolution of the beam, coarse contact-mode NSOM was applied at various positions along the sample, detecting light scattered from the evanescent field of the PhC by a tapered glass fiber-probe [**17**]. Three images taken by this method (at positions 0.02 cm, 0.10 cm and 0.30 cm from the input) are shown in Figs. **1.27**b. Careful analysis reveals near-Gaussian beam shapes and FWHM beam widths of 2.5, 2.5 and 2.7 m ($\pm$ 0.2 m). Deconvolution with the imaging impulse response is necessary to estimate the beam width, yielding values of 2.1, 2.1 and 2.3 m (± 0.2 μ m) respectively. This demonstrates a remarkably stationary beam width over the entire 0.3 cm device.

It is important to note that, while the spot size used to excite the PhC is 1.0 μm FWHM, the collimated beam observed along the PhC has an approximately unchanging beam width of 2.0 μm FWHM. Careful simulations of the beam evolution inside the PhC reveal that over the first propagation distance of approximately 100 μm, the 1.0 μm input beam sheds some of its transverse wave-vector components through diffraction and evolves into a super-collimated

[‡]This scattered light image is a concatenation of several smaller images acquired by the methods described in section **1.5**

beam of 2.0 μm FWHM. The BPM simulations indicate that a 2.0 μm beam is the smallest super-collimated beam that the fabricated PhC can support over centimeter lengths, and experimental observations are consistent with these findings.

Propagation losses of (3.6 $\pm$0.5) dB/mm were measured from the scattered light images (see appendix **C**). This attenuation made NSOM measurements difficult for device lengths greater than 0.3 cm. However, a collimated beam could still be observed by imaging the mode exiting the PhC with a confocal scanning microscope. Fig. **1.28**c shows a confocal image of the TE-light collected at the end of a 0.5 cm PhC device at the super collimation wavelength (λ = 1495 nm). A Gaussian fit, and deconvolution with the imaging impulse response, reveal a beam FWHM of 2.0 ± 0.2 μm, clearly demonstrating negligible spreading of the beam over the entire PhC length. Since the isotropic diffraction length for this PhC is 13.2 μm, these observations are consistent with super collimation over 380 isotropic diffraction lengths. Similar studies at numerous positions along the entire PhC, and in the different symmetry directions, revealed virtually identical optical properties over the entire area of the PhC. Additional studies of a 0.8 cm PhC device have yielded measurements of beams with similar transverse profiles and a figure of merit closer to 600 isotropic diffraction lengths.

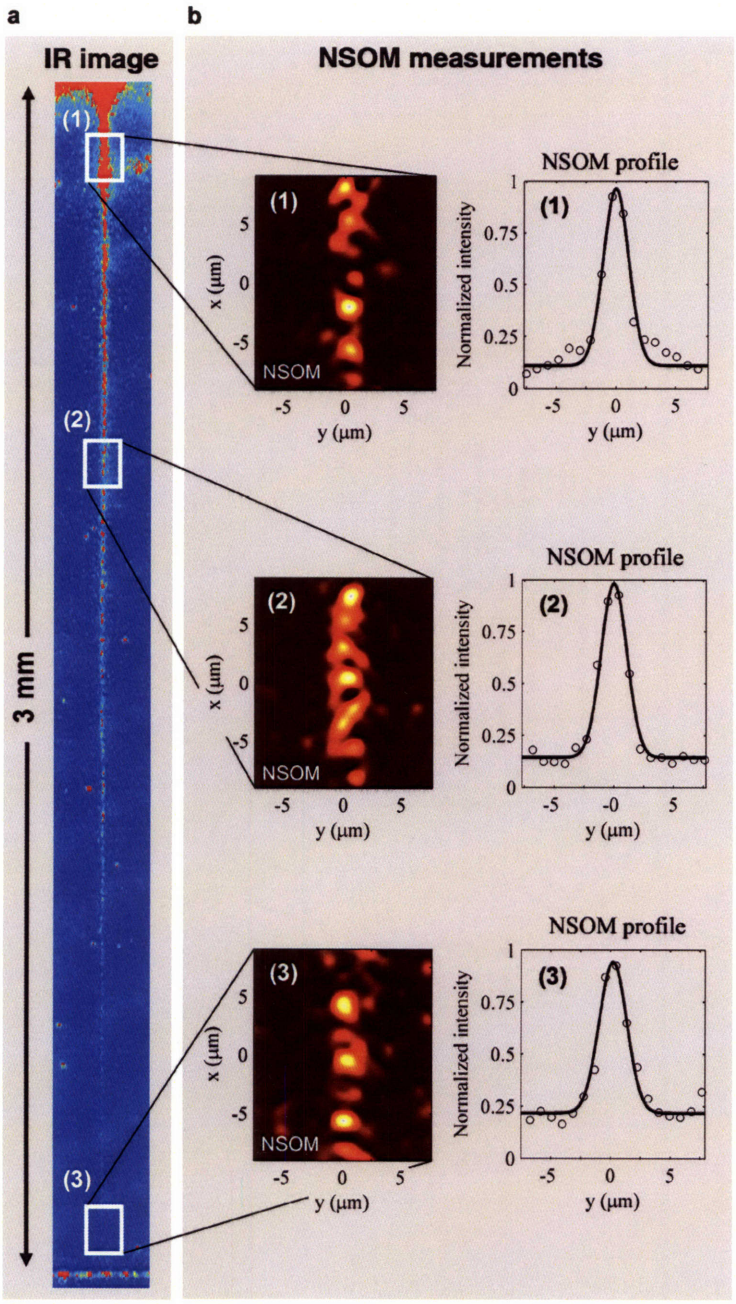

Figure 1.27: a, Top view of the TE light guided along the PhC, acquired with an IR camera. b, NSOM images of the collimated beam at positions labelled (1)-(3) in a (corresponding to 0.02 cm, 0.10 cm and 0.30 cm along the device). Beside each NSOM image is a beam cross section obtained from the intensity map, (with Gaussian fit).

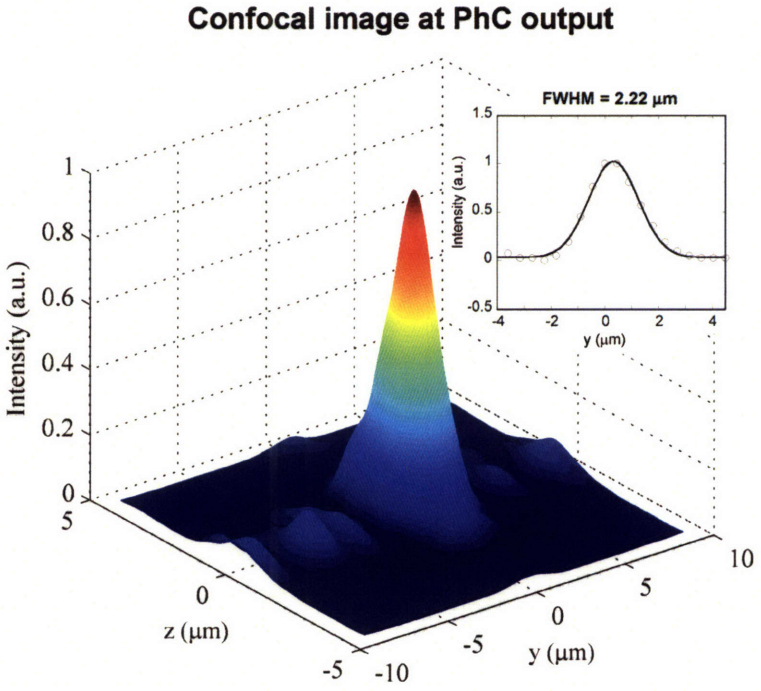

Figure 1.28: Confocal image (displayed as a surface-plot) at the output of an identical 0.5 cm long PhC, showing the TE beam profile at the super-collimation wavelength. Right inset: Line-scan of the beam profile (circles) and a Gaussian fit (solid), showing a 2.2 m FWHM.

1.14 Experimental methods

Although scattered light imaging is a very powerful technique, it is statistical in nature, and suffers from interference effects such as laser speckle. As described in section **1.5**, these effects can be mitigated through spectral averaging; however, it is difficult to obtain quantitative information from such images, since Vidicon cameras typically have nonlinear photo-cathode response in the NIR due to the poor performance of S1 photocathode materials. For these reasons,

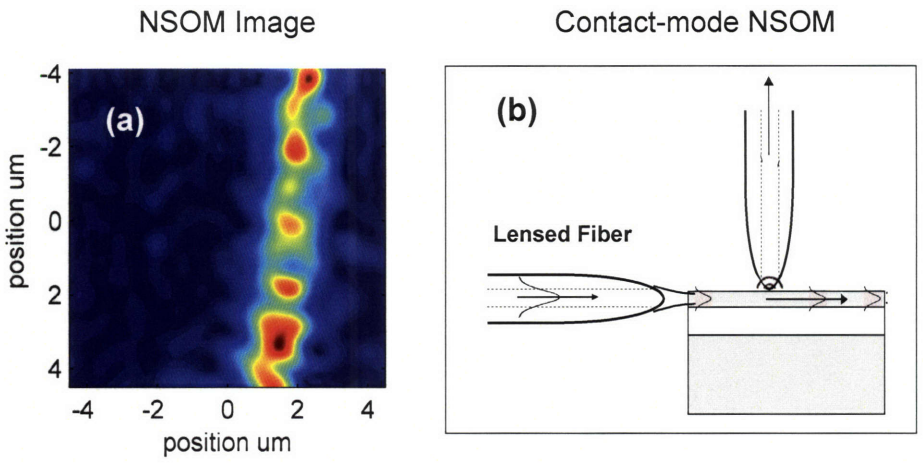

Figure 1.29: Contact-mode NSOM apparatus

NSOM imaging is a very invaluable technique for obtaining quanitative measurements of the beam evolution. In these experiments contact-mode collection NSOM, or photon scanning tunneling microscopy (PSTM) was performed. The basic idea implemented here can be seen in Fig. 1.29b. This technique utilizes the fact that this unclad PhC mode has an evanescent field which extends from the device. Therefore, through near-field interaction, it possible to scatter a small amount of light from the PhC mode through use of fiber probe. Some fraction of this scattered light is collected with the fiber probe and detected as the fiber probe is raster scanned on some area of the device.

The NSOM images of Fig. 1.27 were obtained by exciting a 1 μm FWHM mode at the input of the PhC with use of a Nanonics lensed fiber. Coupling of the lensed fiber was achieved with a piezo controlled flexure stage and monitored with a vidicon camera. Once coupling was optimized, the beam evolution could be visualized through scattered light, and contact mode NSOM imaging

could be used to obtain high resolution images over a small area of interest. The NSOM apparatus used was constructed with GPIB controlled Melles Griot nano positioning stage (Nanoblock 17ANC001) and position calibrated controller (17PCZ013). Images were formed by manually contacting a cantilevered lensed fiber probe to the PhC and then performing computer controlled raster scans. By simultaneously detecting the collected power with a computer controlled lockin amplifier (EG&G 7220), the images of Fig. **1.27** were obtained.

Signal detection is often a problem in NSOM, since experimenters often seek sub-wavelength imaging, which results in photon-starved experiments. However, in these experiments, we only required a resolution which was comparable to the collimated beams to characterize the beam evolution (i.e. $\sim 1\mu$m is sufficient). This affords us the freedom us to use an NSOM probe of larger cross section to enable larger throughput. It was found that with tapered glass fiber probes having a radius of curvature of ~ 1.1 microns [**18**], 10-100 pW of scattered light could collected with 10mW of excitation power. Through lock-in detection (at 2.5kHz) a noise floor of $\sim$100-500 fW could be achieved with a transimpedance amplified InGaAs PIN photodiode, enabling reasonable dynamic range for measurement. Raster scanning while acquiring point-by-point from the lockin-amplifier (EG&G 7220), we were able to obtain the images seen in Figs. **1.27** & **1.29**.

Before any quantitative interpretation of these images can be made, the imaging impulse response of this method must be quantified. Unfortunately, to rigorously compute the impulse response of our probe-waveguide system

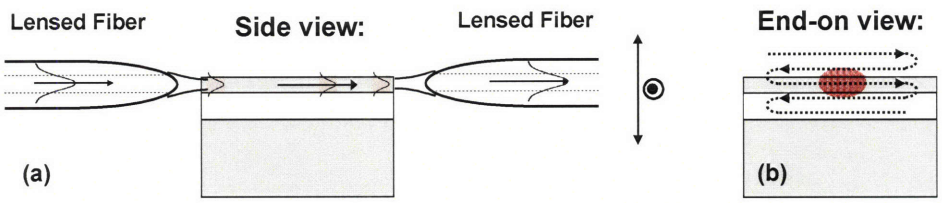

Figure 1.30: Confocal imaging apparatus

isn't trivial, and would require a 3D-FDTD simulations (as well as very accurate knowledge of the probe morphology). However, a reasonable estimate of the imaging impulse response was formed through the measurement of silicon waveguides of dimensions 240 x 450 nm [§]. Although the waveguide width was known to be 450 nm, NSOM images produced the image seen in Fig. 1.29, with an intensity FWHM of $\sim 1.4\mu$m. This allows us to extract a reasonable estimate of the NSOM impulse response through deconvolution with the waveguide width.

Confocal images of the waveguide mode exiting the device, such as that seen in Fig. 1.28, could be formed in a similar way through the experimental geometry seen in Fig. 1.30. Through minor adjustments of the NSOM apparatus, piezo controlled raster-scanning of the collection lensed fiber and lockin detection of the collected light could be performed. The only difficulty here is to ensure that raster scanning of the lensed fiber remains parallel to the output facet of the device. If this isn't done, the impulse response of the acquired image will vary along as a function of position. Furthermore, close proximity of the lensed fiber

[§]Fabrication through E-beam lithography performed by Minghao Qi. Further details provided in chapter 3

to the device endfacet makes damage to the endfacet more likely.

1.15 Conclusions and future work

In conclusion, the established macroscopic nature of super-collimation demonstrates, for the first time, that control of photonic crystal structure at nanoscales enables the realization of an effective bulk medium with anomalous photonic properties. Through a photonic crystal fabricated by interferometric lithography, super-collimation is demonstrated for the first time in a macroscopic photonic crystal system over centimeter-scales. Spatial width confinement is maintained without the need for waveguides or nonlinearities. This is an important first step toward the creation of optical interconnects [19], and it opens new windows of opportunity for novel beam-steering mechanisms [20] and non-diffractive imaging over macroscopic length scales.

Through quantitative studies of the beam evolution in a 2D photonic crystal, it is found that the beam evolution in a real PhC cannot be explained from the average dispersive properties alone. Through experimental and computational studies of the beam evolution, it is found that a miniscule degree of disorder is sufficient to disrupt the behavior of PhC meta-materials, and cannot be ignored in most cases. Despite the problematic effects of disorder, super-collimation is found to be remarkably robust over large length scales. It is discovered that this super-collimation possesses unexpected, but inherent, robustness with respect to short scale disorder (e.g. fabrication roughness) enabling super-collimation

over 600 isotropic diffraction-lengths. The effects of disorder are identified through experiments and understood through rigorous simulations.

In this work we have identified the effects of disorder and established some qualitative trends that disorder related beam breakup follows. However, improved performance of photonic crystal meta-materials requires that the effects of disorder be mitigated. To this end, it seems reasonable to (1) formulate a rigorous theory for beam evolution in disordered meta-materials and (2) investigate ways of quantifying the degree of disorder in an experiment. The initial results presented in sections 1.10-1.12 indicate that that transverse spatial frequencies of beam-breakup may provide strong evidence of the degree of disorder in a photonic crystal. Therefore, rigorous computational studies of such trends could yield meaningful models with which experimental beam evolution can be analyzed.

Chapter 2

Broadband studies of 1D and 3D photonic crystals

2.1 Introduction

High-index contrast photonic crystal waveguides are of interest for an increasing variety of applications. However, the measurements required to understand the basic physical phenomena of photonic crystal devices often present serious experimental challenges. In many cases it is necessary to perform spectral measurements over 50 - 100% of the center frequency of the device (i.e. as much as an octave) in order to understand the bandgap-related phenomena. Additionally, due to the nano-scale dimensions of such devices, high insertion losses and low throughput are typical in a laboratory setting. It is for this reason that high brightness sources such as tunable lasers are typically used to scan the broad spectral features of photonic crystals. Unfortunately, tunable laser

sources spanning the entire 1 - 2 μm spectral range, critical for the study of telecom-centered devices, are not readily available. To facilitate the science and study of photonic crystals and integrated photonic devices, we develop practical femtosecond fiber-laser-based supercontinuum sources (SC) spanning the 1.2 - 2.0 μm wavelength range and broadband SC based measurement techniques. These techniques are then applied to a host of new studies of high index contrast photonic crystal devices. Experiments involving both 1D periodic photonic crystal microcavity waveguides and 3D periodic photonic crystals with embedded point defects are described. Experimental findings are compared with rigorous electromagnetic simulations [**21**, **22**, **23**].

2.1.1 Background

Earlier applications of SC sources to the study of photonic devices have utilized solid state Ti:Sapphire sources and short lengths of microstructured fiber (centered at 800 nm) to the study of silicon nitride photonic crystals with a system utilizing free-space optics [**24**]. Unfortunately, short lengths of nonlinear fiber tend to result in wavelength polarization drift, making them difficult to use. In contrast, we develop unpolarized all-fiber SC sources centered at telecommunications wavelengths (1.55 μm) for the study of photonic crystals and integrated circuits. To minimize the losses and complexity produced by broadband free space optics, we focus instead on all-fiber methods for broadband polarization control and coupling. Additionally, through sensitive detection and careful normalization many of the undesirable aspects of a typical SC source

can be mitigated, producing high fidelity measurements over the entire 1.2 - 2.0 μm wavelength range [**21**, **23**].

2.2 Supercontinuum sources and techniques

Over the past couple of decades, numerous methods of supercontinuum generation have been studied in physical systems ranging from gas filled optical cells to nonlinear waveguides [**25**]. However, the tremendous interaction lengths and high mode confinement afforded by fiber-optics have made possible the most dramatic supercontinuum generation to date [**26**, **25**, **27**, **28**, **29**], giving rise to a host of devices and applications. Although supercontinuum generation is an exceedingly complicated nonlinear process, [**26**, **25**, **27**] the necessary requirements for most efficient supercontinuum generation can be summarized quite simply. One requires a fiber-optic with: (1) anomalous dispersion, (2) large nonlinear coefficient and (3) large peak optical excitation powers. At shorter wavelengths, the modal confinement afforded by microstructured or tapered fibers is required to produce the anomalous dispersion in silica fibers*. However, since silica exhibits anomalous dispersion at long wavelengths, conventional step-index fibers can produce total anomalous dispersion at 1.5 μm, enabling effective supercontinuum generation about these wavelengths.

*Bulk silica possesses normal dispersion from 1300nm to shorter wavelengths. Therefore, a large anomalous waveguide dispersion is required to enable anomalous total chromatic dispersion.

2.2.1 Nonlinear fibers for supercontinuum generation

In this work we pursue SC generation with use the of step index fibers and femtosecond sources centered at 1.5 μm since this offers the most efficient conversion of laser power to the 1.0-2.0 μm wavelengths. In the early stages of supercontinuum source development, the nonlinear properties of various highly nonlinear step-index fibers were investigated with the use of a Ti:Sapphire pumped tunable optical parametric oscillator (OPO). This tunable femtosecond source, which produces pulses of 150 fs duration, enabled peak powers of ~12 kW to be coupled into single mode fibers over wavelengths near 1550 nm. This was helpful to identify the optimum conditions for efficient supercontinuum generation in various fibers. Two noteworthy examples of spectra generated in nonlinear fibers can be seen in Fig.**2.1**. The SC spectra of Figs.**2.1**a & b were produced by a 9 meter length of Furukawa HNL fiber and 500 meters of Sumitomo HNL-DSF fibers whose parameters are described in Table **2.2**.

While we can see that both fibers generate usable spectrum over the 1.2-2.0 μm range ,initial experiments revealed some important distinctions in the polarization properties of the two fiber sources. It was found that, with the 9 meter Furukawa fiber, the polarization state produced at each wavelength differs and tends to wander over the course of several minutes. During polarization sensitive measurements, polarization drift presents a problem since polarization state variations can result in wild variations in the signal-to-noise ratio. Interestingly, no such problems occured when the 500 meter length of Sumitomo fiber was

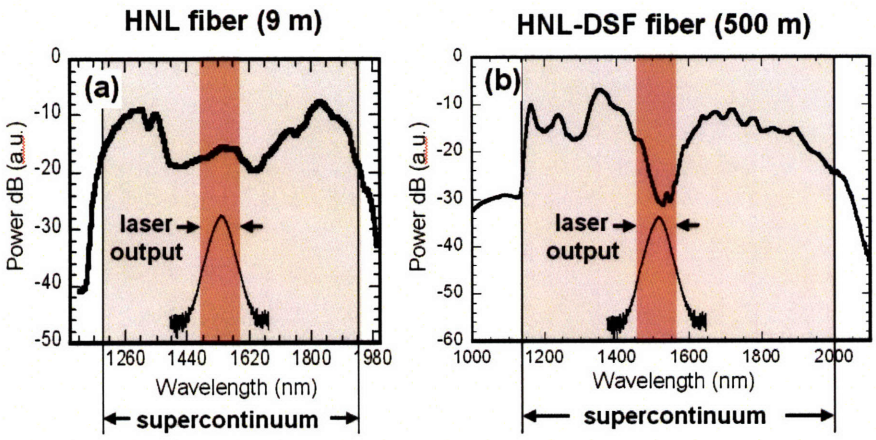

Figure 2.1: (a) Laser spectrum (before) and supercontinuum spectrum (after) Furukawa highly nonlinear fiber (b) Laser spectrum (before) and supercontinuum spectrum (after) Sumitomo highly nonlinear dispersion-shifted fiber (HNL-DSF)

Fiber type	HNL (Furukawa)	HNL-DSF (Sumitomo)
Dispersion	-1.259 ps·(nm·km)$^{-1}$ at 1550 nm	Zero at 1565
Nonlinear coefficient	22 (W·km)$^{-1}$	23 (W·km)$^{-1}$

Figure 2.2: Table of relevant fiber paramters for both Furukawa and Sumitomo fibers studied

used, making it a much more practical source despite the larger spectral variations it exhibits. Further study of the polarization properties revealed that SC generated by the Sumitomo fiber is unpolarized when measured at millisecond time-scales.

Numerous factors likely contribute to the unique polarization properties of the Sumitomo fiber, however, the most important are its large length, and high nonlinear coefficient. These makes possible a very high degree of nonlinear polarization evolution (NPE). This process is illustrated in Fig. 2.3, and results

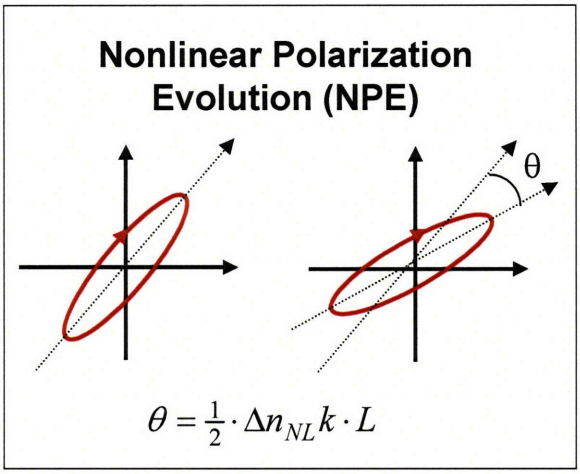

Figure 2.3: Diagram illustrating nonlinear rotation of an eliptical polarization state through Kerr nonlinearities. Here Δn_{NL} is the difference between nonlinear index induced along the major and minor axes, k is the wavenumber in the medium and L is the interaction length.

in intensity dependent rotational transformations of eliptical polarization states within a fiber optic [26, 30]. To understand how NPE manifests itself on the SC spectrum we need only know that within the first several meters the vast majority of spectral generation has occurred, resulting in numerous distinct pulses (most are picosecond duration solitons) with sufficient peak power to incur ~1000 radians of rotation in the remaining length of fiber [31]. Therefore small fluctuations in intensity are sufficient to result in large changes in polarization state. Furthermore, amplitude noise at the input of the fiber is greatly amplified through the nonlinear processes, which likely results in a wildly different polarizations state from pulse to pulse [32].

2.2.2 Unpolarized fiber-laser supercontinuum source

Although the OPO was a very powerful tool for the study of nonlinear fibers, it is a rather costly and impractical for use as a white light source, making this approach of SC generation unrealistic in any real-world applications. Fortunately, sufficient peak powers are attainable with use of compact fiber lasers for SC generation at 1.5 μms, making an fiber-laser-based unpolarized supercontinuum source a realistic goal.

To this end, the stretched-pulse fiber laser seen in Fig. **2.4**(a) was developed by Hideyuki Sotobayashi and Jason Sickler. The laser consists of a 55.6 cm length of bismuth oxide based erbium-doped fiber (Bi-EDF), 1.8 meters of low-nonlinearity single-mode fiber (LNL-SMF), two polarization controllers, and a polarizing beam-splitter. The rejection port of the polarizing beam splitter forms the output coupler of the laser, while a bi-directionally pumped length of Bi-EDF fiber serves as the gain medium, providing a broad gain bandwidth and high gain per unit length [**33**]. To balance the dispersion of the Bi-EDF, and manage the intracavity nonlinearity, 1.8 m of LNL-SMF is included in the laser. Mode-locked operation of the laser was obtained through nonlinear polarization evolution[**34**]. For pump powers of 350 mW, a 28 mW average output power was obtained with center wavelengths and spectral full-width half maxima of 1571 nm and 58 nm respectively. Through external compression with a 1.8 m segment of LNL-SMF 100-fs pulses were obtained, providing a peak pulse power of $\sim$8.5 kW which was sufficient for the generation of a broad SC spec-

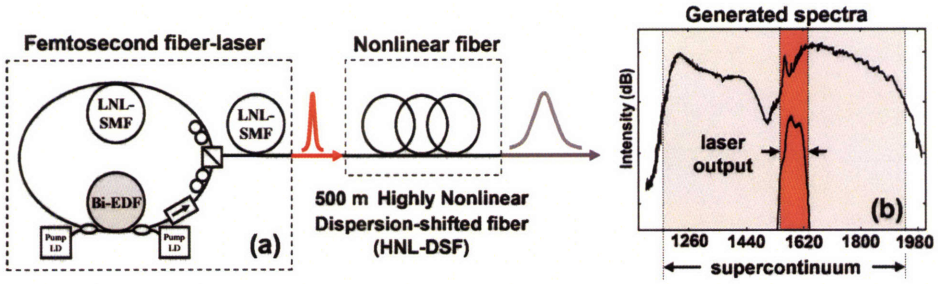

Figure 2.4: (a) Schematic of supercontinuum source, which consists of a femtosecond fiber-laser and a length of highly nonlinear dispersion shifted fiber. (b) Optical power spectrum of the fiber laser output before and after passing through the nonlinear fiber.

trum. Pulses are injected into 500 meters of HNL-DSF having a zero-dispersion wavelength of 1565 nm and a nonlinear coefficient of 21 km^{-1} W^{-1} to generate SC. The laser spectra before and after the HNL-DSF are shown in Fig. 2.4(b). As was the case in OPO excitation, the supercontinuum light generated by this method is unpolarized when measured at millisecond time scales due to nonlinear polarization evolution produced in the HNL-DSF. Additionally, the nonlinear nature of the SC generation makes the shape of the spectral output very sensitive to changes in laser state [32].

The SC spectrum generated in the HNL-DSF is coupled into the apparatus shown in Fig. 2.5(a) for waveguide transmission studies. The unpolarized SC light is first passed through a broadband fiber-optic coupler, splitting the continuum into two ports, signal and reference. The signal is then sent through an inline polarizer and polarization controller, which define the polarization at the input of the waveguide. A lensed fiber is then used to couple the signal into the waveguide. A second lensed fiber collects the waveguide output that is

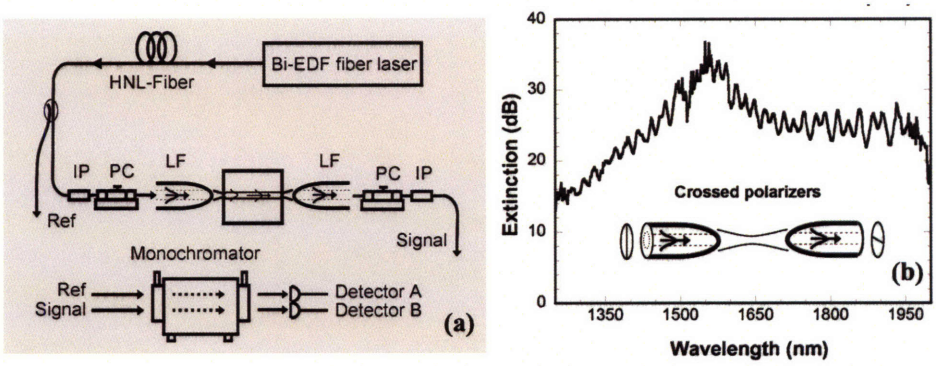

Figure 2.5: (a) A schematic of measurement apparatus. A small fraction of SC light is diverted by a coupler for reference (Ref) measurement while the remainder (Signal) is passed through the waveguide. The signal and reference are then imaged through a monochromator onto identical photodetectors for real time normalization. (b) Polarization extinction obtained through polarization control method depicted in (a).

sent through a polarization controller and inline polarizer for polarization analysis. The signal and reference are then imaged through a monochromator onto two identical photodetectors, for real-time normalization of the SC fluctuations and spectral changes. Detection is performed with Peltier cooled IR-enhanced InGaAs photodiodes and lock-in amplifiers to achieve low noise measurements (with a noise equivalent power of 28 fW/$\sqrt{Hz}$) and enable rapid scans (less than one minute) with as little as 4 mW of SC light.

Polarization control of the light launched into the waveguide and polarization analysis of the light collected from the guide were performed with use of broadband inline polarizers and strain-type polarization controllers as depicted in Fig 2.5(a). As can be seen in Fig. 2.5(b), this provides greater than 20 dB of polarization extinction over most of the spectral range of the SC source. However, critical to broadband performance is (1) the type of in-line polarizer used,

and (2) minimization of polarization mode dispersion (PMD) which follows the polarizer. Laminated in-line polarizers of the type described in reference [**35**] were used to provide high extinction and low insertion losses over the entire 1 - 2 μm wavelength range. PMD was managed by minimizing the length of fiber between the polarizer and lensed fiber and any bending experienced by the fiber. For the measurement shown in Fig **2.5**(b), fiber lengths were kept below 30 cm. Additionally, through a slight change in the state of the polarization controller $>$ 25 dB contrast can be achieved at any wavelength in the 1.2 - 2.0 μm range, enabling higher polarization extinction through more than one wavelength scan if needed.

2.3 Studies of 1D photonic crystal with a defect

This method was applied to the study of a number of HIC devices, however, in this paper we will examine a 1D photonic bandgap microcavity and 3D photonic crystal with point defects [**23**]. The 1D photonic crystal microcavity, which has been studied extensively over the past several years, consists of a silicon strip on top of an oxide layer, forming a waveguide with a single TE-like mode over much of the 1 - 2 μm wavelength range [**36**, **37**]. A photonic crystal is patterned in the waveguide by etching a periodic array of holes through the silicon strip. The photonic crystal defect is then defined by increasing one hole spacing from a (the lattice constant) to a_d (the defect length). A device schematic and scanning electron micrograph (SEM) are shown in Fig. **2.6**(b).

For comparison with experiments, simulations of the device band structure and power transmission were performed based on the parameters extracted from SEM measurements [**38**, **15**]. Results of the band-structure computations can be seen in Fig **2.6**(a) while the dashed curve of Fig **2.6**(c) shows the simulated power transmission. Superposed with the theoretical transmission (dash) of Fig. **2.6**(c) is the measured transmission spectrum (solid) obtained with the apparatus described above. It is important to note, however, that normalization was crucial to obtaining the photonic crystal transmission characteristics. The experimental transmission seen in Fig. **2.6**(c) was obtained by measuring the transmission of a waveguide with a photonic crystal and normalizing to a calibration scan of an identical waveguide without a photonic crystal. This enables the removal of spectral variations due to waveguide coupling and waveguide propagation losses.

It should be noted that, through SEM measurements, a lattice constant of $a = 424$ nm $\pm 5\%$ was found. Simulations demonstrate best agreement when using $a = 410nm$, which is within the experimental uncertainty; no other parameters were adjusted. Remarkable agreement is seen between the salient features of both experiment and theory for wavelengths between 1400 - 2000 nm. A 265 nm stop-band is clearly visible in the experiment from approximately 1425 - 1690 nm. In addition, the high-resolution scan shown in Fig. **2.6**(d) reveals a sharp microcavity resonance at 1542 nm. On resonance, efficient power coupling through the photonic crystal is observed, with approximately 52% transmission. This is in reasonable agreement with the simulated transmission

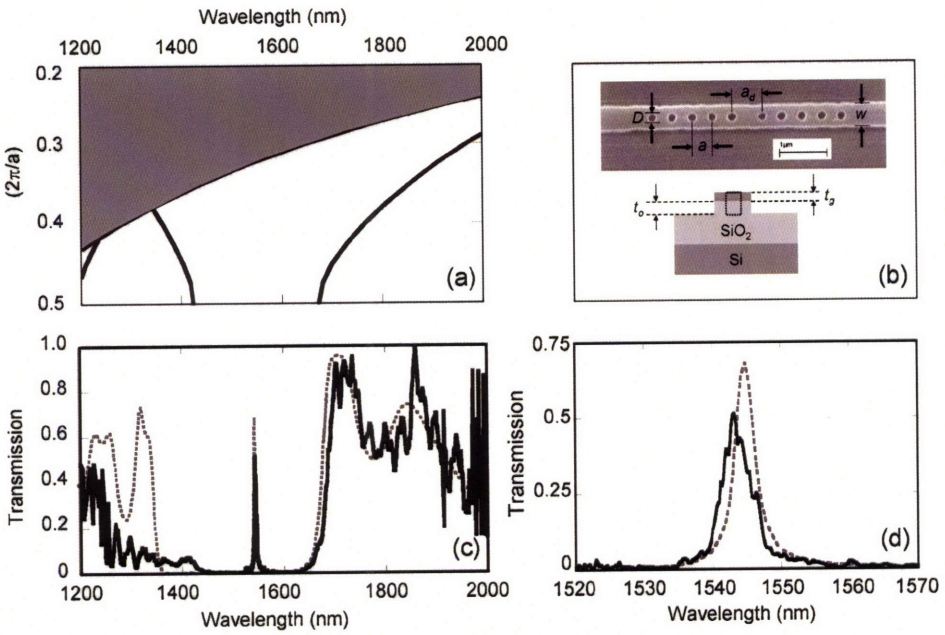

Figure 2.6: (a) Band diagram (TE-like bands only) based on SEM measurements of device. Grey region indicates states above the light line. (b) SEM of microcavity (top) and cross-section of waveguide (bottom). Device parameters extracted from SEM are a = 424 nm, ad = 649 nm, w = 494 nm, tg = 195 nm, to = 350 nm, and D = 179 nm. (c) A transmission measurement (solid) and simulated transmission (dashed) of photonic crystal microcavity (TE polarization). The transmission measurement is normalized to that of a similar waveguide without etched holes. (d) High resolution (0.1 nm) measurement (solid) and simulation (dashed) of the microcavity resonance.

efficiency of 68%. For wavelengths below 1400 nm the onset of a higher order waveguide mode complicates the device behaviour, resulting in some discrepancy between experiment and theory. Nevertheless, this method clearly resolves the photonic bandgap and the defect resonance, demonstrating a remarkable wavelength range for the study of photonic crystals in the NIR.

2.4 3D photonic crystal with point defects

A similar supercontinuum based technique was applied to the study of a 3D photonic crystal, with embedded point defects, enabling high spatial resolution studies (with a 2.5 μm spot size) of a small number of embedded point defects which were randomly distributed within the PhC. An SEM of the 3D PhC under study can be seen in Fig. **2.7**(c), and was fabricated in silicon through a layer-by layer process utilizing several successive e-beam lithography steps. This 3D photonic crystal exhibits a 21% complete photonic bandgap at telecom wavelengths. The details of this fabrication process can be found in reference [**23**]. The fabricated structure consists of alternating layers of two complementary 2D photonic crystal slabs, one layer of dielectric rods and another of air holes in a dielectric slab. Embedded within the PhC are randomly distributed defects, each consisting of a completely filled air hole. Defects of this type produce a spatially localized photonic crystal mode, having numerous resonant states within the photonic bandgap, which couple to radiation. These defects are dispersed within the photonic crystal with a density of 15%. Despite the remarkable fabrication quality, inhomogeneity in the environment of these point defects was unavoidable, resulting in inhomogeneous broadening of defect states throughout the PhC. For this reason it was necessary to probe very small areas of the PhC to resolve the energy spectrum of individual defect cavities. Spectroscopic studies of these defects over small areas proved difficult with thermal white light sources due to their low brightness. However, SC based

measurement techniques yielded high fidelity measurements of a small number of nano-scale PhC defects, allowing the energy spectrum of individual defects to be fully resolved.

In this study, supercontinuum-based confocal reflection and transmission measurements were used to examine a small number of defects embedded within the PhC. An average of 3 PhC defects could be studied with use of a Gaussian spot size of 2.5 μm generated by a lensed fiber. The supercontinuum source used in these studies consisted of a Ti:Sapphire pumped optical parametric oscillator (OPO) which was used generate SC spanning 1.2 - 2.0 μm in highly nonlinear fiber. Further details about the SC source are described in Ref. [**22**]. In these experiments, a reference channel was used to normalize for any spectral variations; however, unpolarized SC light was sufficient to observe the defect resonances, making polarization control unnecessary.

Spatially localized reflection measurements, taken by this method, were performed at numerous positions on the photonic crystal. Some characteristic reflection and transmission measurements can be seen in Figs. **2.7**(b) and (d) along with the corresponding theoretical transmission and reflection spectra computed through 3D FDTD computations. The experimental geometry for the transmission measurement is depicted in the inset of Fig. **2.7**(a). Here a lensed fiber forms a 2.5 μm Gaussian spot size on the PhC, while a flat-cleaved single mode fiber optic was used to collect the light transmitted through the PhC over a narrow range of transverse wave-vectors (corresponding to $\sim$1 degree half angle). The PhC transmission spectrum was then normalized to a

similar measurement through the same substrate, without the PhC in the path. We can see that the bandgap of the PhC is clearly resolved along with two peaks in the transmission spectrum (denoted by I & II in Fig. **2.7**(b)), corresponding to resonant transmission through the multi-mode point defects. This can be seen by comparing the theoretical (aqua) and experimental (red) transmission spectra. Such peaks in transmission are not found in simulations of the structure without defect states (green), clearly indicating that these spectral features result from resonant transfer of power through the defect modes. More striking features resulting from the defect states are observed as dips in the reflection spectrum. This is because the reflection measurement probes a large transverse wave-vector range (corresponding to a 15.5 degree half angle), which is more suitable for coupling to localized defect states which tend to radiate over large solid angles. A detailed comparison of the experimental (red) and theoretical (aqua) reflection spectra can be made from Fig 4(d). Three dips are observable in the reflection spectrum at approximately 1.4 μm, 1.5 μm and 1.6 μm wavelengths (denoted by III, IV & V in Fig. **2.7**(d)), which result from resonant coupling to localized defect states within the PhC. The observed stop band and the positions of the defect resonances are in remarkable agreement with the simulated reflection spectrum. It should also be noted that all parameters used to simulate the transmission spectra shown below were extracted from SEMs of the device, and no free parameters were used.

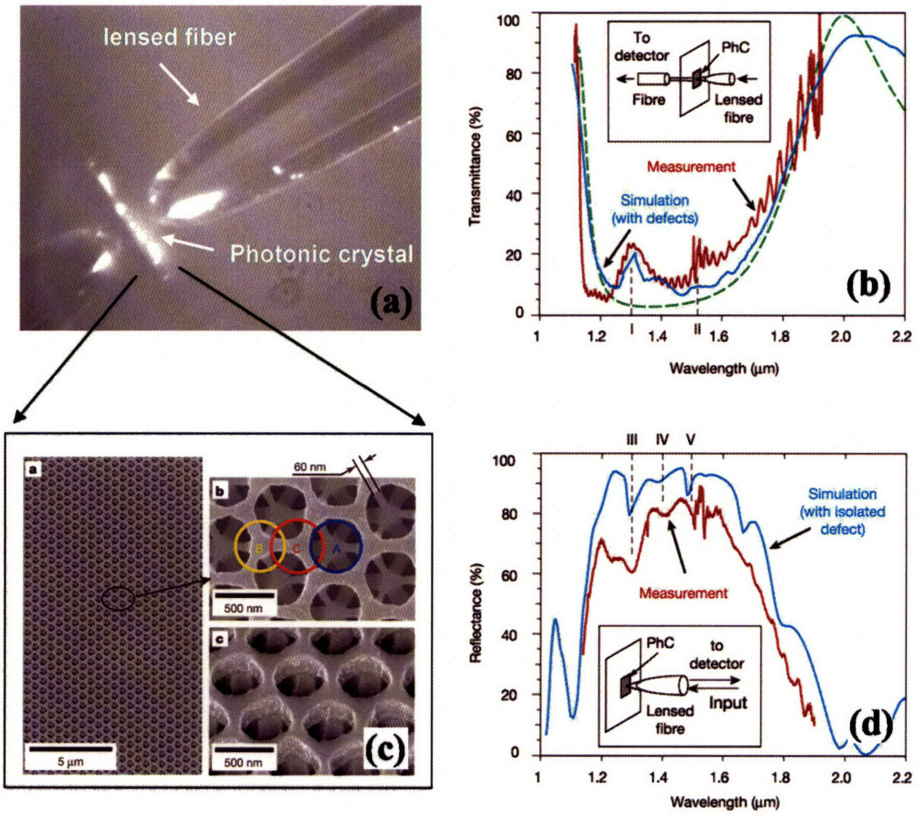

Figure 2.7: (a) photo of lensed fiber and photonic crystal 3D PhC device under test (b) Theoretical (aqua) and experimental (red) transmission spectra of 3D PhC with defects. Theoretical transmission of PhC without defect states (green dash). (c) SEM of 3D fabricated SEBL (d) Theoretical (aqua) and experimental (red) reflection spectra of 3D PhC with point defects.

2.5 Conclusions

In conclusion, a newly developed unpolarized supercontinuum source provides a practical means of studying photonic devices over broad wavelength ranges in the NIR, enabling a host of new studies involving both 1D periodic photonic crystal microcavities and 3D periodic photonic crystals. An all-fiber apparatus enables very practical and low-loss means of utilizing supercontinuum sources over the 1.2 - 2.0 μm wavelength range for photonic crystal studies. Additionally, through sensitive detection and careful normalization many of the undesirable aspects of a typical SC source can be mitigated, producing high fidelity measurements of nano-scale photonic devices over the entire wavelength range.

Chapter 3

High index-contrast microphotonics for reconfigurable telecom networks

3.1 Introduction

Microphotonics is a growing field of research, whose purpose it is to miniaturize highly functional optical components such as waveguides, filters, switches such that they can be implemented on planar surfaces through lithographic techniques. Such large scale integration promises to yield high performance photonic circuits and most advanced optical functionality, and benefit applications ranging from spectroscopy to sensing and telecommunications networks. Over the past several decades much effort has been placed on the development of low index contrast optical circuits which utilize coarse optical lithography ($\Delta n/n$

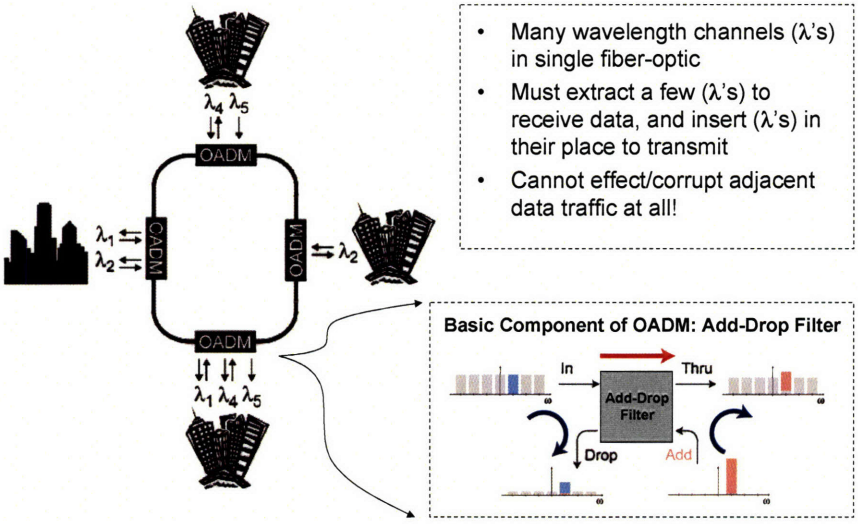

Figure 3.1: Schematic demonstrating basic function of fiber-optic ring network. Lower right inset depicts the basic function of optical add-drop multiplexer (OADM) which forms the cornerstone for such networks[Graphics by Tymon Barwicz and Milos Popovic].

of 5% and lower) and enable the creation of crucial components such as array waveguide gratings (AWGs) and distributed Bragg gratings [4, 39, 40, 41, 42]. Due to the low degree of spatial confinement afforded by LIC circuits, they tend to be of centimeter scale and have performance limitations. In the past decade, recent advances in lithography and computation have enabled the study of HIC circuits ($\Delta n/n$ of 100% and greater) that are sub-wavelength in dimension and permit increased modal confinement, strong coupling of modes, and reduced bending losses, all of which are important to conventional waveguides and PhC based waveguide research.

In this chapter we describe research on HIC based microring based filters for the purpose of routing and detecting data channels transmitted through fiber-

optic telecommunications networks. The basic concept used in implementing a wavelength division multiplexed (WDM) fiber-optic ring network is summarized in Fig. **3.1**. Data is encoded on distinct wavelength channels ($\lambda_1, \lambda_2 ... \lambda_n$) which are transmitted through the ring fiber-optic network [**40**, **41**, **42**]. A particular λ (or λs) can be assigned to any two cities (or nodes) for transmission of data between them. The addition or removal of a data channel (or channels) is performed by a device called an optical add-drop multiplexer. This sounds simple enough. However, with an increasing number of channels and the requirement of high transmission efficiencies (meaning low bit error rates (BER)), much of the burden and complexity of this optical network is shifted to the OADM. For an example of suitable drop-port and through-port characteristics for an OADM in real-world applications, see the filter requirements detailed in Fig. **3.2**. Furthermore, the most efficient use of a telecommunications network can be made if the data channels are dynamically allocated between nodes of the telecom network. This too presents a great challenge for integrated optics.

To date, virtually all networks of this type use costly and large (dispersive) AWG devices to demultiplex all channels passing through the ring network. These demultiplexed channels are then passed through an array of optical switches (such that only a few channels can be dropped and detected), after which the remaining data channels are multiplexed and transmitted to the next node [**4**, **39**, **40**, **41**, **42**]. While this approach is effective, it carries a high signal penalty (6-12 dB per node) and the large AWG sizes (typically 10 cm) result in high costs for these components. For these reasons, HIC microphotonics have

been the subject of intense study over the past decade.

Although dispersive AWGs are the most proven technology for integrated optical demultiplexing of signals, resonant cavity based filters clearly show the greatest promise for dense integration. Recently high performance PhC-based and ring resonator-based microcavities of wavelength-scale have been demonstrated in Silicon on Insulator materials (index contrast 3.5:1) systems. The research described here seeks to use microring resonators (of scale $\sim$100 λ) to synthesize filters and OADMs in a silicon-rich silicon nitride materials system (index contrast 2.2:1). Due to the complex nature of integrated photonics research, this program has required close collaboration on materials science, nano-lithography, electromagnetic design, and optical metrology. The following chapter focuses most heavily on results obtained through optical studies of photonic materials and devices.

3.2 Filter synthesis with microrings

Microring resonators, such as the one depicted in Fig. **3.3**a, have been studied extensively in optics because of numerous advantages they possess over more conventional resonant devices [**43**]. Some key apects of a microring are: (1) it is a traveling-wave multi-port resonator device, (2) it produces spatially separate resonant and non resonant response, (3) separation of resonant and nonresonant response occurs without need to break time-reversal symmetry. See, for example, Fig. **3.3**. These characteristics present numerous advantages over

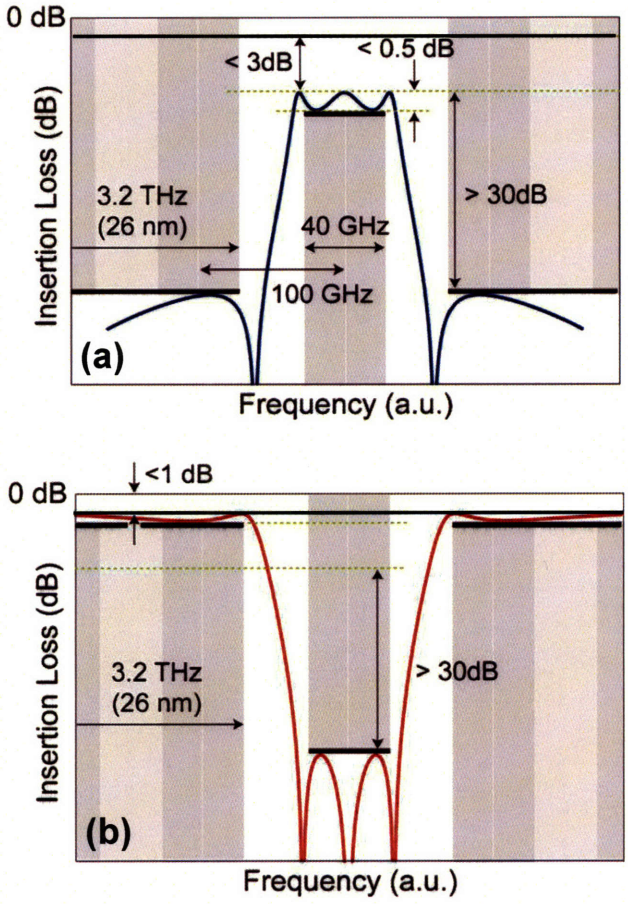

Figure 3.2: Ideal transfer functions of drop and through filter response. [plots by Milos Popovic]

standing wave resonators, such as Fabry-Perot cavities and distributed gratings, making them ideal for use in complex optical circuits. Such advantages were first recognized and exploited for use in Microwave circuits and networks. However, only recently has it been possible to implement ring resonator-based optical cavities of micron scale.

The Lorentzian first order microring response seen in Fig. 3.3b is not appro-

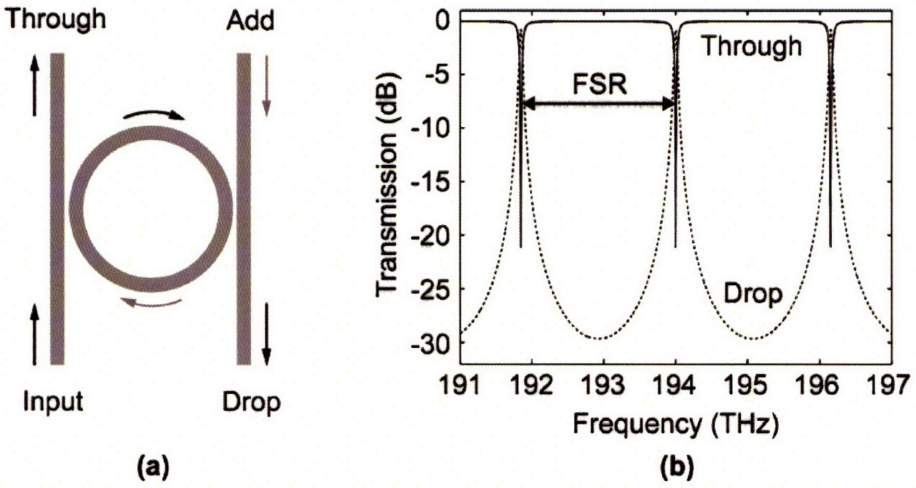

Figure 3.3: (a) Diagram of first order microring resonator. (b) Ideal frequency response of first order microring for the drop and through ports. [Figure by Milos Popovic]

priate for use as an OADM in telecommunications networks. A natural means of synthesizing a more suitable higher order filter response is via cascading such microrings. Precise placement of the microring frequencies and control of the coupling coefficients between resonators enables the synthesis of arbitrary filter response in a way that is analogous to that done in electronics today. Time dependent coupled mode theory provides a natural formalism through which higher order coupled microring filter synthesis can be performed [12]. Numerous realizations of such designs have been carried out in LIC systems [44].

To date, cascaded microring devices have been studied extensively in LIC materials systems (index contrast $\leq 5\%$), and large FSRs have been obtained through vernier* schemes [45] for the purpose of spectral slicing in star networks

*Vernier schemes in multi-resonator systems simply refer to the cascading of rings with differing FSRs such that the product of their transfer functions yields an artificially

(i.e. no through-port used). Although the vernier approach is effective for the synthesis of large FSRs, it generates intolerable dispersion for all through channels and makes such schemes impractical for OADM filter synthesis. For these and other reasons, artificial means of generating large FSR microcavities from numerous small FSR cavities is not practical. It is apparent that there is no substitute for large FSR cavities in important applications such as OADM synthesis.

As discussed in the introduction, high extinction through response is important to ensure that small amounts of power from dropped signals don't continue in the ring network. Dimensional sensitivity analyses reveal that the extinction ratios of higher-order microring through responses are far more sensitive to coupling coefficients and the placement ring super-mode frequencies than is the drop response [**46**]. This places greater burden on fabrication tolerances and design and is likely a reason that this problem hasn't yet been addressed in microphotonics literature.

Unfortunately, large FSR microring cavities can only be constructed in HIC materials systems, since a reduction in the bending radius requires tighter modal confinement. This presents a host of new challenges for microphotonics research since HIC microphotonics demand waveguides and lithographic features whose dimensions, in many cases, are controlled at the nanometer scale. Furthermore, lithographic roughness often results in intolerable waveguide and microring losses. Both require research in and refinement of materials science

increased FSR.

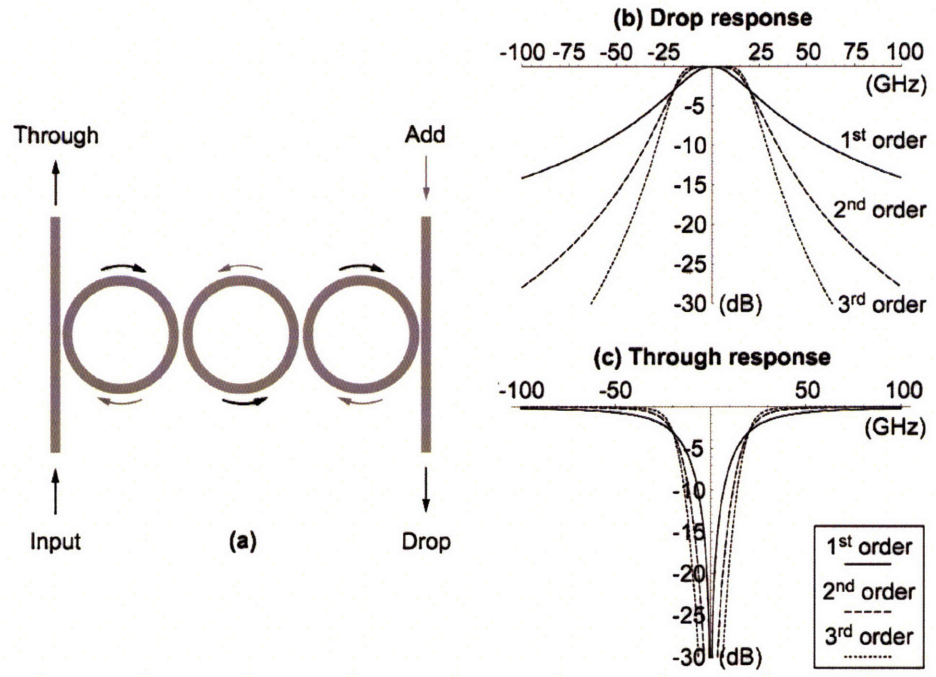

Figure 3.4: (a) Diagram of third order microring resonator. (b) Ideal frequency response of lossless first, second and third order microring resonators for the drop and through ports. [calculations by Milos Popovic]

and lithography techniques. Sub-micron waveguide dimensions also require sophisticated solutions for efficient coupling from fiber-to-chip, a long-standing problem for microphotonics to which there is no obvious solution.

3.3 Frequency compensated third-order filters

Through the coupling of identical microrings, which facilitates the higher order filter response seen in Fig. **3.4**, one generally expects that a coupled system will exhibit a set of eigenfrequencies (or supermodes) dictated by the coupling strength between the resonators. In our early studies of third order microring

filters it was found that some higher order corrections to the ring frequencies become very important in determining super-mode frequencies of a real coupled microring system [**47**]. This is important for filter synthesis since the frequencies of these supermodes must be known for proper placement of filter poles [**44**, **48**]. A drastic example of filter distortion arising from unwanted shifts in the supermode frequencies can be seen from the measured response of a fabricated third-order microring of Fig. **3.5**a.

Analysis of this device reveals that the one of the super-modes exhibits a drastically different resonant frequency from that expected from the initial CMT-based design (which assumes identical uncoupled ring frequencies). Further finite-difference time domain (FDTD) simulations, performed by Milos Popovic, reveal that the supermode frequency-shifts arise from the fact that time-dependent coupled mode theory (CMT) doesn't take into account the spatial complexities of the coupled waveguide system. It becomes necessary to incorporate critical higher order corrections when designing multi-ring filters system through CMT [**50**].

Correction in the ring frequencies can be performed in a number of ways through various lithographic structures and post fabrication trimming techniques. However, with electron-beam lithography, systematic changes in electron-beam dose have enabled the direct fabrication of frequency-compensated three-ring filters [**47**, **49**]. Through this method the ring width can be systematically controlled at the angstrom level, which is necessary for proper frequency compensation of higher-order microring filters.

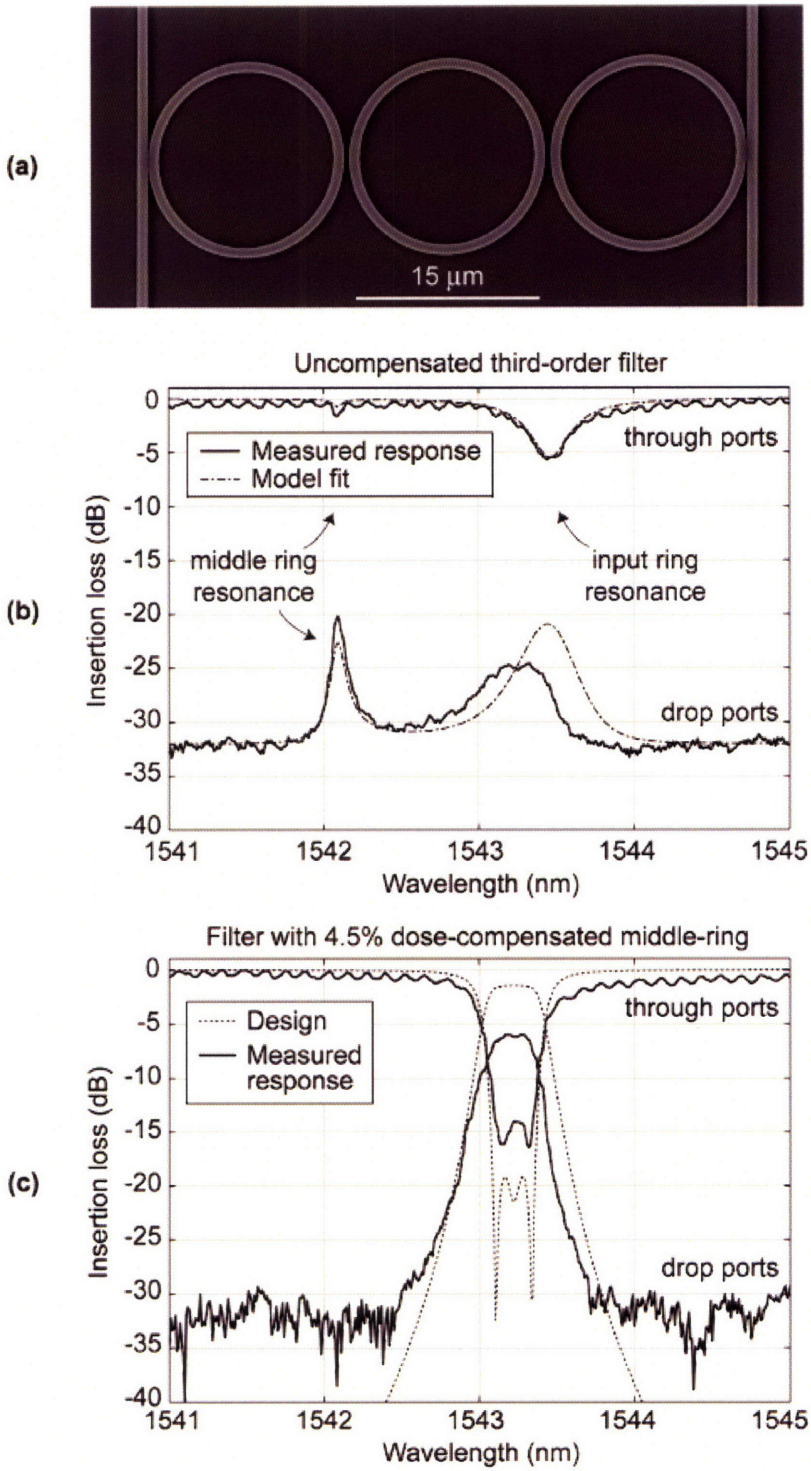

Figure 3.5: (a) SEM of third order microring resonator. (b) Frequency response of uncomopensated third order microring resonator (c) Response of frequency compensated microring. [Figure taken from Ref. [49]]

Using this method of ring-frequency compensation, a through-port contrast of 14 dB was obtainable for individual third order microring filters as seen in Fig. **3.5**c. This is a significant improvement over previously reported performance of microring based filters. While the drop response for this third order filter exhibits sufficient roll-off to the adjacent channel (see Fig. **3.2**) for OADM synthesis, a through-port contrast of 14 dB isn't sufficient for rejection of dropped signals. Higher contrast is, in principle, achievable through use of 4th and 5th order filters, but then frequency compensation becomes much more complex. Furthermore, stochastic lithographic variations place some limit on the degree to which this performance can be achieved [**46**]. For these reasons, we implement a multi-stage filter design to achieve the a through-port contrast of 30 dB seen in Fig. **3.2**. The multi-stage filter design seen in Fig. **3.6**a affords much more robustness to lithographic variations while ensuring a filter through-port contrast of $>$ 30 dB. Although, proper implementation can only be made with sufficiently frequency matched 2nd and 3rd stage filters.

The spectral response measured for both 1, 2 and 3 stage filters can be seen in Fig. **3.7**b-d. As can be seen from the compensated single stage filter result, a through-port contrast of 17 dB was obtained. In principle, it seems clear that adding more subsequent stages of well matched filters will increase the through contrast; however it was initially unclear to what degree polarization conversion within rings and coupling regions would place a fundamental limitation on the through contrast. It is known that slanted sidewalls, produced through the etch process, result in some degree of polarization conversion between TE and TM

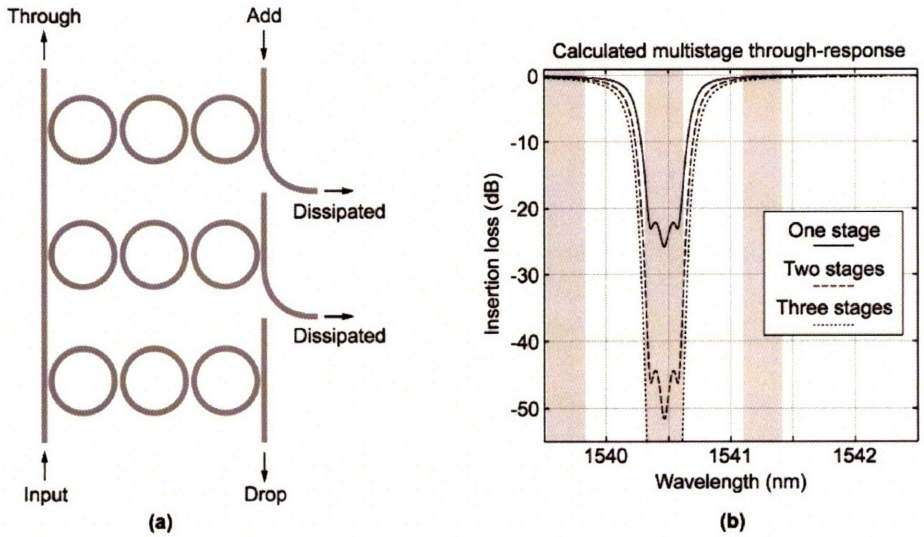

Figure 3.6: (a) Schematic of 3-stage third order microring filter (b) Plot of through response as number of stages is increased from one to three. [Design by Milos Popovic]

polarizations [51, 52, 53]. Fortunately, careful study of the device polarization eigenstates through the experimental methods described in section 3.6.4 reveal that the polarization conversion doesn't appear to present a problem for sidewall angles of 2-3 degrees [54]. As can be seen in Fig 3.7c, two stages yield ~30 dB of contrast, and three stages yield between 47-51 dB of in-band contrast. This filter response far exceeds the requirements for through-port contrast in a telecommunications based OADM, and is the first microcavity-based HIC notch filter of its kind.

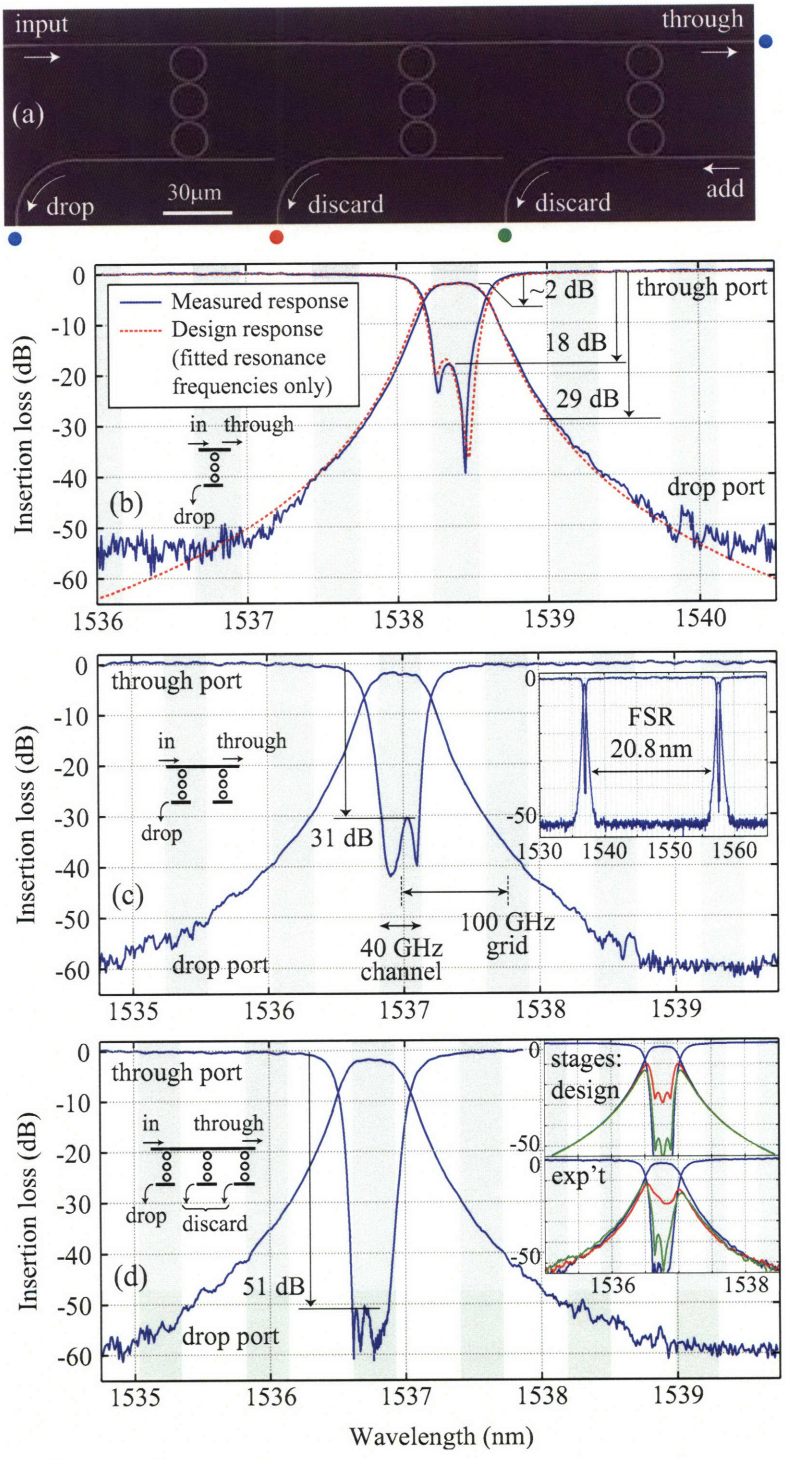

Figure 3.7: (a) SEM micrograph of 3-stage third order microring filter (b) measured response of single stage filter (c) double stage (d) and triple stage filters from the same device [taken from reference [46]]

3.4 Polarization independent microphotonics

As described in section **3.2** we have achieved a truly remarkable filter performance that is suitable for OADM applications. However, it must be emphasized that this filter performance can only be achieved for TE polarization in devices of this type. This is because the TM mode is much more poorly confined and experiences very different bending losses and coupling coefficients. Polarization sensitives of this type are pervasive in HIC microphotonics and have been the basis for long-standing criticism of HIC microphotonics, since this makes them incompatible with the optical fibers necessary to connect the devices to the outside world. This is because polarization states evolve randomly in optical fibers and become ill defined after only meters of length. This prevents use of HIC microphotonics in numerous applications ranging from communications to spectroscopy to sensor networks. Almost all published HIC microphotonic devices suffer from polarization sensitivity. In our work, this major obstacle is overcome by demonstrating a general scheme allowing polarization-transparent microphotonic circuits to be built from arbitrary polarization-sensitive microphotonic devices. To demonstrate this approach, we create a polarization transparent optical add-drop filter (OADF) from polarization-sensitive microring resonators filters described in section **3.2**. This rigorous test case demonstrated almost complete elimination of polarization sensitivity while maintaining outstanding filter performance. To our knowledge, the resulting microphotonic circuit is the most complex implemented to date. In this section, we show that, with

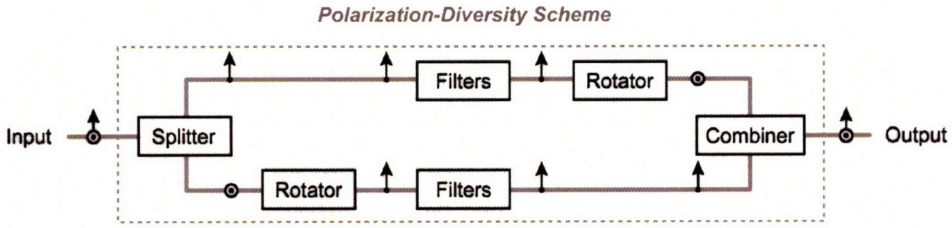

Figure 3.8: Diagram depicting the polarization diversity concept. Light of arbitrary polarization is split into TE and TM states. The TM state is then rotated to TE, and passed through identical polarization sensitive devices. The reverse is done to recombine them at the output. [Graphic by Hermann A. Haus and Michael R. Watts]

the proposed approach and with innovative high-fidelity nanofabrication techniques, HIC microphotonics, such as photonic-crystal structures and microring resonators, can be used in real-world applications today.

3.4.1 Polarization diversity in HIC microphotonics

The polarization diversity scheme is very simple in concept. One can use two identical polarization dependent devices to achieve polarization independent response if incident light is decomposed into its TE and TM polarizations and passed through identical filters. To do this on a lithographically fabricated microphotonic circuit, we must rotate the TM state to TE so that both states will see a similar device response. After transmission through the polarization sensitive components, the ports can be transformed in a similar (symmetric) manner such that TE and TM light is recombined. A diagram of this configuration can be seen in Fig. **3.8**.

3.4.2 Polarization splitter and rotator

The polarization splitting and rotation operations present a very interesting challenge for lithographically fabricated HIC microphotonics. Of all the possible methods, an adiabatic means of splitting and rotating polarizations is the most inherently broadband and robust means [**55**, **56**, **57**]. However, these device designs required the development of a novel two-layer nanofabrication technique in order to break the vertical waveguide symmetry. Through the dual hard-mask, scanning electron beam lithography (SEBL) techniques both adiabatic designs were successfully implemented in SiN [**58**].

3.4.3 Implementation of polarization diversity

Our goal, however, is to effectively utilize these newly developed components to obtain a polarization independent filter that is appropriate for use in a real WDM telecom network. This requires integration of all of the aforementioned devices into a single working optical circuit that enables splitting, rotation and filter transmission, before the inverse operations are performed to recombine the filtered polarization states (see Fig. **3.8**). Since three ports from each filter must be accessed, (Add, Drop and Through) waveguide crossings are also necessary, leading to the device design seen in Fig. **3.9**a. Waveguide crossings were implemented through an adiabatic expansion of the waveguide such that the fundamental mode experiences lower divergence, enabling low cross-talk horn-type crossings. With this waveguide crossing design a complete OADM with

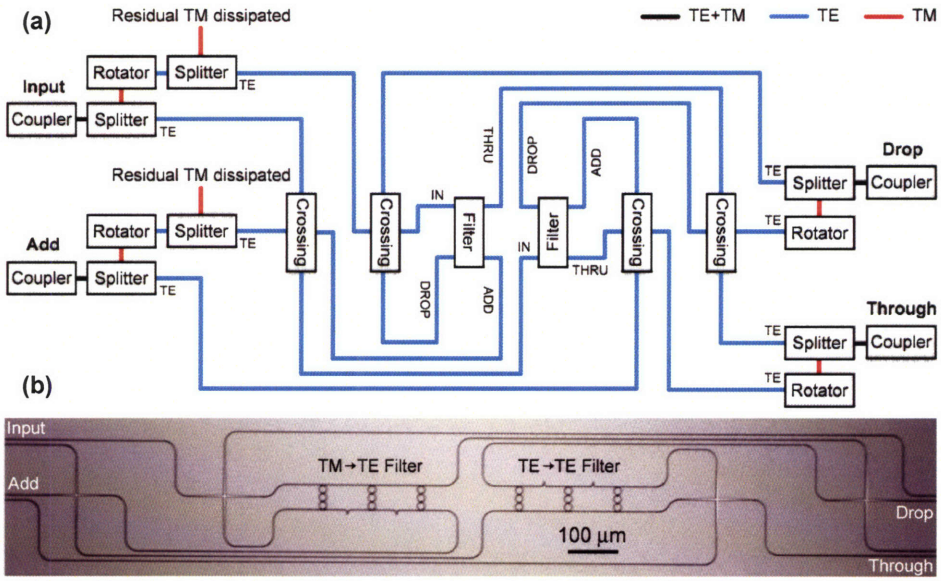

Figure 3.9: (a) Diagram of optical add-drop multiplexor layout indicating the path of the TE and TM polarizations. Note that routing of signals to the Add, Drop and Through ports necessitates the use of waveguide crossings. (b) Optical micrograph of fabricated polarization independent OADM. Polarization splitter-rotators are out of the field of view. [images by Tymon Barwicz]

polarization diversity was fabricated using a similar dual-hard mask technique to that described above, yielding the device seen in Fig. 3.9b.

Optical studies of the fabricated device seen in Fig. ?? were performed through the laser-based methods described in section 3.6.4. In order to achieve proper ring frequency compensation, 30 copies of the same circuit were fabricated with varying middle-ring electron beam doses. Of these 30, a small number will be nearly frequency compensated, yielding high contrast through response. Transmission of the through and drop ports of the best compensated filter for both the TE and TM eigenstates reveal that both multi-stage filters

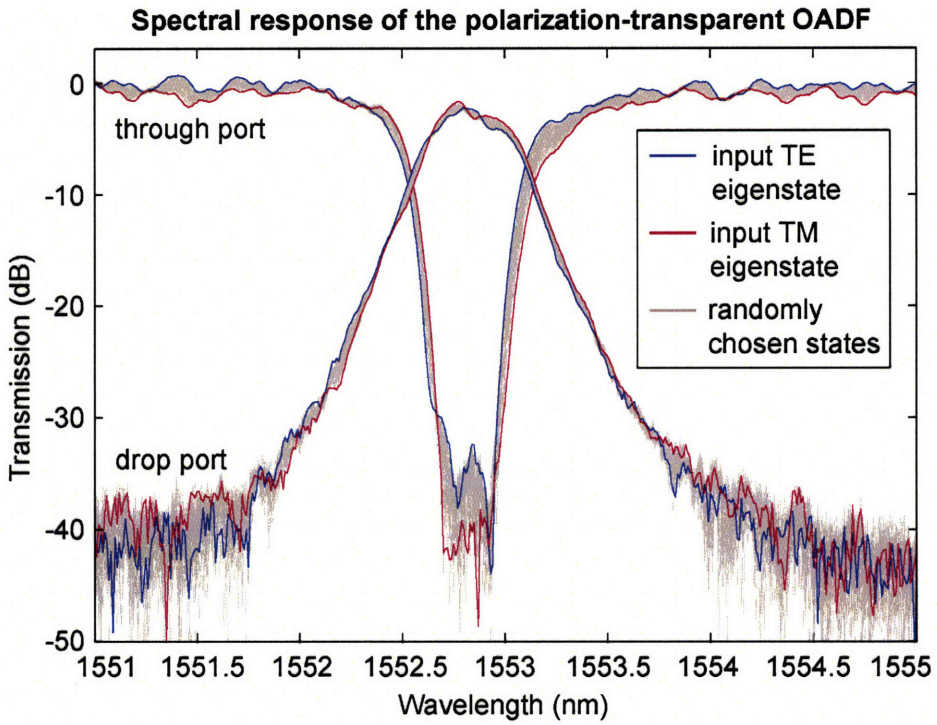

Figure 3.10: Transmission spectrum of drop-port and through-port for TE input (Blue) TM input (Red) and 100 randomly chosen polarization states (Grey)

are remarkably well frequency aligned and that there is less than 2dB of polarization dependent loss (PDL) between eigenstates, a drastic improvement from the 35-40 dB generated otherwise. These eigenstate measurements can be seen in Fig. **3.10** along with a scan of 100 randomly chosen input polarization states, demonstrating that the eigenstates form the upper and lower bounds for the PDL and are a good measure of the device performance in this case. It should be noted that the high through-contrast (~35 dB) would not be achievable without good polarization splitter and rotator performance.

3.4.4 Origin of residual polarization dependence

In studying the PDL over larger bandwidths, we find that it exhibits a maximum value of 2.2 dB in the through-port transmission over the C-band wavelengths (1530-1565 nm). Oscillations of 2-5 nm FSR are observed throughout. This frequency of oscillation is not consistent with the length of the Fabry-Perot cavities that are likely to be formed in the circuit layout, leading us to believe that modal interference is the only plausible culprit. Throughout study of isolated PSR devices and horn crossings and three ring filters on the same device, similar such oscillations were observed, but only for the cross-state in horn crossing transmission. A transmission spectrum of a typical horn crossing is shown in **3.11**. The cross-state consistently experiences larger insertion losses than the straight-state. SEM images of the crossings later revealed that rotational stitching errors were far worse for the cross-waveguide E-beam field than for the through, resulting in an abrupt offset and partial waveguide discontinuities. Measurements of three different horn-crossings on the same device yield various excess losses seen in table **3.12**.

In the complete device, it is plausible that the magnitude of the stitching errors is larger for TE than TM since they are written at different times, and accumulated stage drift of the Raith E-beam will differ, resulting in PDL. Fortunately, this is a relatively easy problem to correct in future device fabrications, since either improved layout or improved waveguide crossings can be implemented.

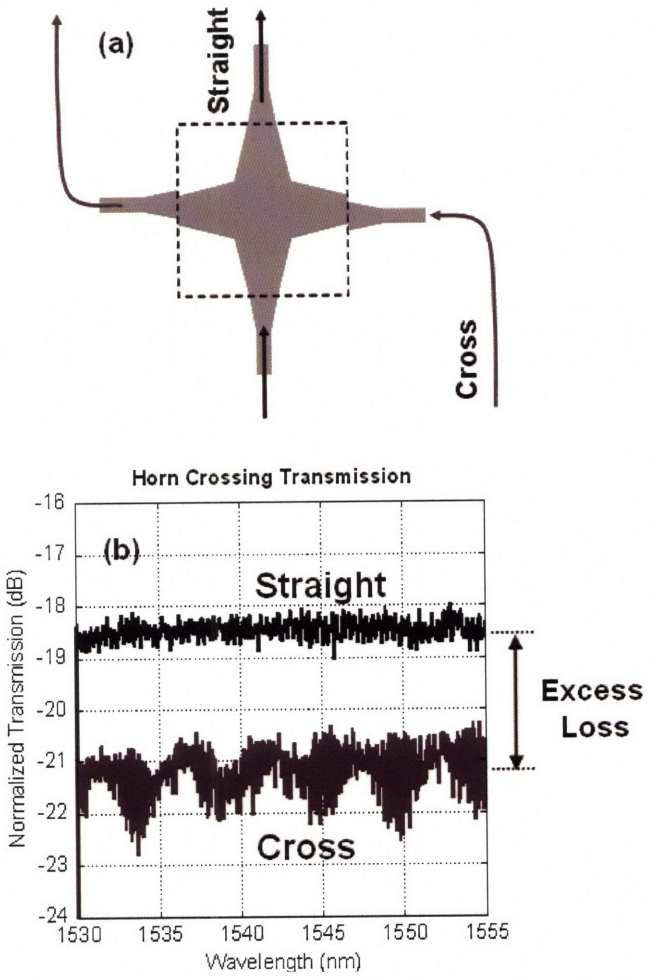

Figure 3.11: (a) Schematic of horn crossinig implemented in polarization diversity scheme. (b) Measured TE transmission of straight and crossed ports of horn crossing

	Cross #1	Cross #1	Cross #1
Excess loss (dB)	2.5±0.5dB	1.8±0.5dB	3.2±0.5dB

Figure 3.12: Measured values of measured horn-crossing excess losses

Despite some minor imperfections, we have achieved a truly remarkable degree of PDL in a high index contrast system. This is a tremendous first accomplishment for HIC microphotonics, which is necessary for useful implementation of microrings, photonic crystal devices and other such HIC devices.

3.5 Material loss studies

Since the performance of microrings and optical circuits is strongly dependent on waveguide losses, characterization and minimization of waveguide losses is of paramount importance. Unfortunately, the material properties of thin films, from which waveguides are constructed, often differ from their bulk properties (if they even exist in bulk form). Therefore, the only way to determine their loss characteristics is often through the study of guided mode transmission. This creates a serious challenge for materials science in the context of integrated optics, since the study of guided modes presents numerous additional complexities. This is because the waveguide losses originate from, not only absorption, but also scattering due to interface roughness, lithographic stitching errors, and substrate and other forms of mode leakage. Fortunately, numerous waveguide loss measurement techniques have been developed and are commonly used, although all of them have advantages and disadvantages. From a materials science perspective, however, it is most meaningful if one can obtain loss data over a large wavelength range so that some understanding of the thin-film electronic structure can be obtained. In this section, we describe the loss studies per-

formed on silicon-nitride films which were deposited through various methods, and compare these results.

3.5.1 Silicon nitride loss studies

As described in the previous sections, the large FSR microrings of this research require a high-index-contrast materials system. Although stoichiometric silicon nitride (Si_3N_4) thin films are known to have very low intrinsic losses, they have an index of refraction $\sim$ 1.98, which doesn't generate sufficient index contrast to support rings of FSR larger than $\sim$10-12 nm. For this reason we use of a silicon-rich silicon-nitride (grown via low pressure chemical vapor deposition (LPCVD) vertical thermal reactor (VTR) system) film with index $\sim$2.2. This might seem like a marginal difference, but it affords bending radii of $\sim 8\mu m$ and microring FSR of 20-24nm due to the rapid reduction of bending losses with index contrast [**43**, **44**, **59**].

Since, in the development of integrated circuits, we pursue high quality-factor resonators (Q) and low losses over the device dimension ($\sim$centimeter), it is generally desirable to have small losses on the centimeter length-scale (e.g. $\leq$3dB/cm is an admirable benchmark). This is important since it places a lower limit on total loss that a circuit can achieve. The bulk and thin-film properties of stoichiometric silicon-nitride (Si_3N_4) are well known. It is an amorphous material with an absorptive band-edge near 400 nm, resulting in a refractive index of 1.98 at telecom wavelengths [†] It is also well known that silicon-rich

[†]through Kramers Kronig relations, it is clear that the closer the electronic resonance,

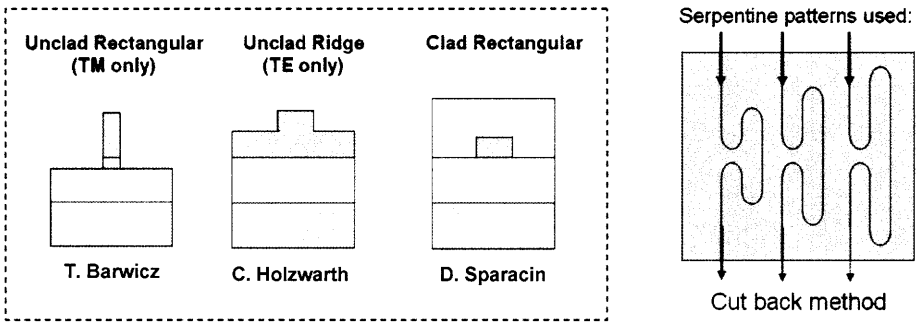

Figure 3.13: (Left) Crossections of the various waveguides used to perform cut-back loss measurements. (Right) Schematic of serpentine patterns used to vary the length of a waveguide segment for cut-back measurements.

silicon-nitride has a higher refractive index (from ellipsometry measurements) due to the lower energy band-edge produced by the increased silicon content. However, the impact that this silicon content has on the absorptive properties at telecom wavelengths was unclear, as little had been published on this matter.

Over the course of this project, we have applied a number of measurement techniques to the study of the high silicon-content SiN films, including microring resonators based loss measurements, Fabry-Perot loss measurements, imaging techniques, and cut-back measurements. Comments on and discussion of these techniques can be found in appendix D. However, the most useful and reliable technique was found to be the cut-back method, which we describe briefly here. The cutback method (or paper-clip method) simply refers to a series of power transmission measurements through waveguides of differing lengths. The first waveguides studied in low-index-contrast could not tolerate significant

the larger refractive index becomes. Silica, for example has an absorption band in the UV, resulting in an index of refraction of 1.445 at 1550 nm.

waveguide bending, so waveguides of differing lengths were fabricated, or a single device was measured as its length was cut-back. However, in high-index-contrast, bends can facilitate the fabrication of different waveguide lengths on the same chip through serpentine patters of the type seen in Fig. **3.13**. The key advantage of this method is that it provides a measure of the waveguide losses over very large wavelength ranges. This cannot be said of resonant methods described in appendix **D**.

Example measurements obtained through the cut-back method can be seen in Fig. **3.14**. Power transmission measurements obtained with use of the apparatus described in section **3.6.4** enabled insertion loss measurements from 1260-1630 nm. This loss study involves a rectangular waveguide in VTR nitride (n = 2.2) of dimensions 330nm x 820nm[‡] supporting only a TM waveguide mode for much of the measurement range. Decreasing transmission is seen in Fig.**3.14**a as the differential length of the serpentine patterns is increased from 0-10 mm. From the data seen in Fig.**3.14**a, the wavelength dependent loss is obtained through a linear fit of insertion loss versus differential length. Each circle displayed in Fig.**3.14**b is the result of such fits, yielding an uncertainty of ± 1 (dB/cm) over most the measurement range. For this waveguide geometry, interface roughness at the side walls, stitching errors and intrinsic losses each produce some component of the measured waveguide losses. Through evaluation of the sidewall roughness and the magnitude of the stitching errors[**54**, **60**] we can see that stitching errors are not apt to account for more than 2dB

[‡]January 2005 OADM fabrication

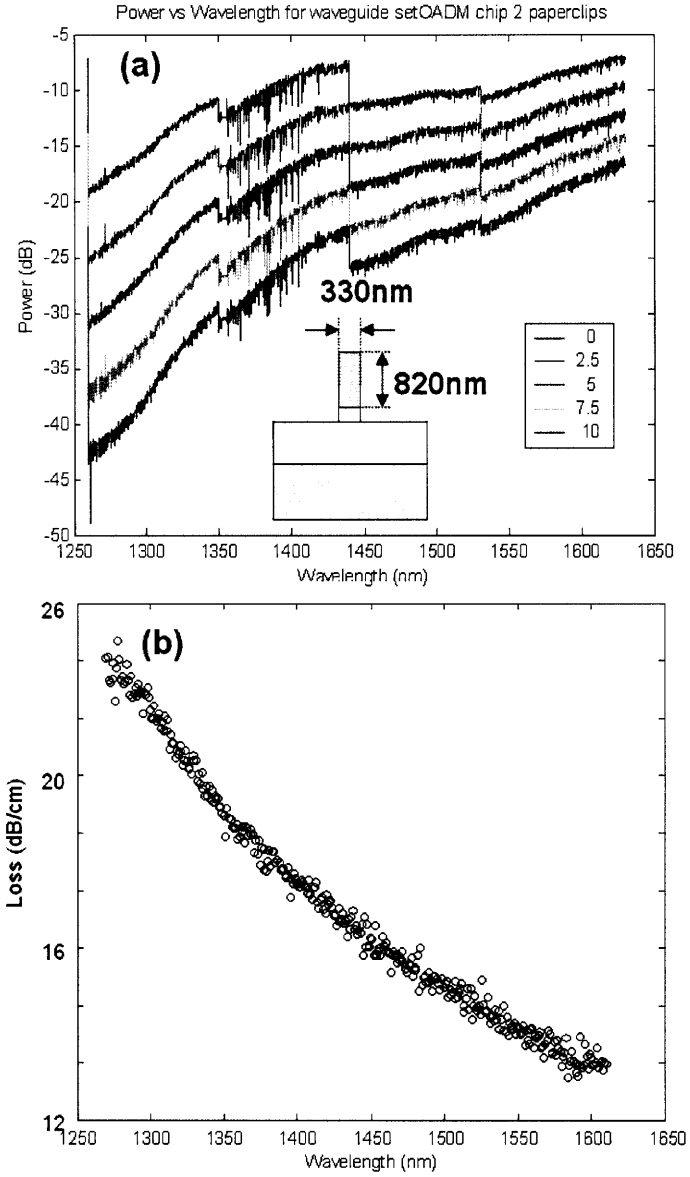

Figure 3.14: (a) Power transmission measurements obtained through serpentine waveguides of the crossection seen in inset. Decreasing transmission (dB) can be seen as the differential guide length is increased from 0-10 mm. (b) Computed waveguide loss (dB/cm) extracted from power transmisison measurements displayed in (a). Each circle is the result of a linear fit of power transmission vs length (5 points in each fit). [Waveguide fabrication by Tymon Barwicz]

of loss, and scattering losses are only likely to contribute 2-3 dB/cm of loss. These estimates, along with the fact that the losses do not scale with $1/\lambda^4$ lead us to believe that the major component of the losses seen here is an intrinsic absorption tail due to increased silicon content in the VTR nitride.

Scattering losses can be further reduced by the use of ridge waveguides of the type seen in Fig. **3.13**. This is because only a small fraction of the mode overlaps with lithographically formed side-wall roughness. Furthermore, the effects of stitching errors should be negligible in this case, since the mode cross section approaches 1 μm which is much larger than the stitching errors (typically 30-50 nm). For these reasons, a ridge waveguides provide a more direct measurement of intrinsic losses. Ridge structures were fabricated in both VTR and DCVD nitride materials by Charles Holzwarth through E-beam lithography. Cutback loss measurements similar to those described above were performed on these ridge structures, and compared with the measurements of Fig. **3.14** in Fig. **3.15**. As can be seen, cutback measurements on the ridge structure yield loss estimates between 6.5-8 dB/cm at telecom wavelengths, which is significantly lower than the 10-12 dB/cm measured in the rectangular TM waveguides.

In principle the scattering contribution to the losses can be made smaller by reducing the waveguide index-contrast with the aid of a silica overcladding. Figure **3.15**b displays some cutback measurements silica overclad VTR nitride waveguides, revealing a similar loss figure to that obtained through the ridge waveguide measurements. However, some additional structure to the loss profile is also apparent when the cladding material is introduced. The most notable

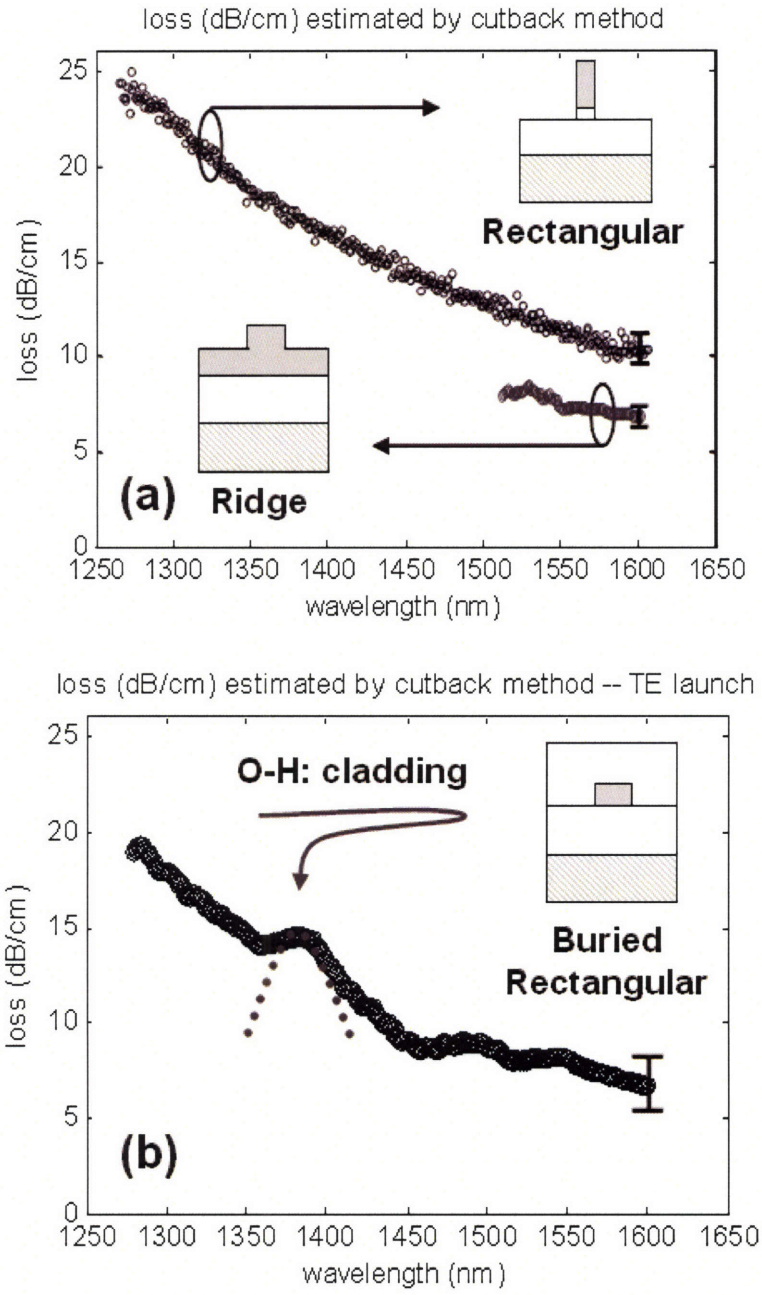

Figure 3.15: (a) Computed waveguide loss (dB/cm) for TM-rectangular guide and ridge structures in inset [Fabrication by Charles Holzwarth and Tymon Barwicz] (b) Computed waveguide loss (dB/cm) for buried rectangular waveguide [Waveguide fabrication by Daniel Sparacin]

feature is the resonant peak centered 1380nm, which is consistent with an O-H absorption resonance.

3.6 Experimental methods

3.6.1 Modal analysis of waveguides

In optical studies of microphotonic waveguides and materials, there are numerous instances when imaging of waveguide modes can be helpful. For example, spectral oscillations in device transmission may be an indication of modal beating, often observable as a wavelength dependent mode evolution at the waveguide output. Multi-mode performance is often avoidable in rectangular waveguide geometries if the waveguide dimensions precisely controlled, however, experience has shown that these subtleties are more difficult to evaluate in ridge waveguides. This is, in part, because ridge structures are multi-mode systems with a fundamental mode that is often weakly confined. Therefore, the conditions of excitation can greatly effect the transmission characteristics, making modal imaging of utmost importance.

3.6.2 Free-space imaging methods

Throughout this research, two different modal imaging techniques have been applied to the study of waveguides, both have distinct advantages which we describe in detail here. The most obvious technique, which was first applied through our studies, is shown schematically in Fig. **3.16a**. It utilizes a lens

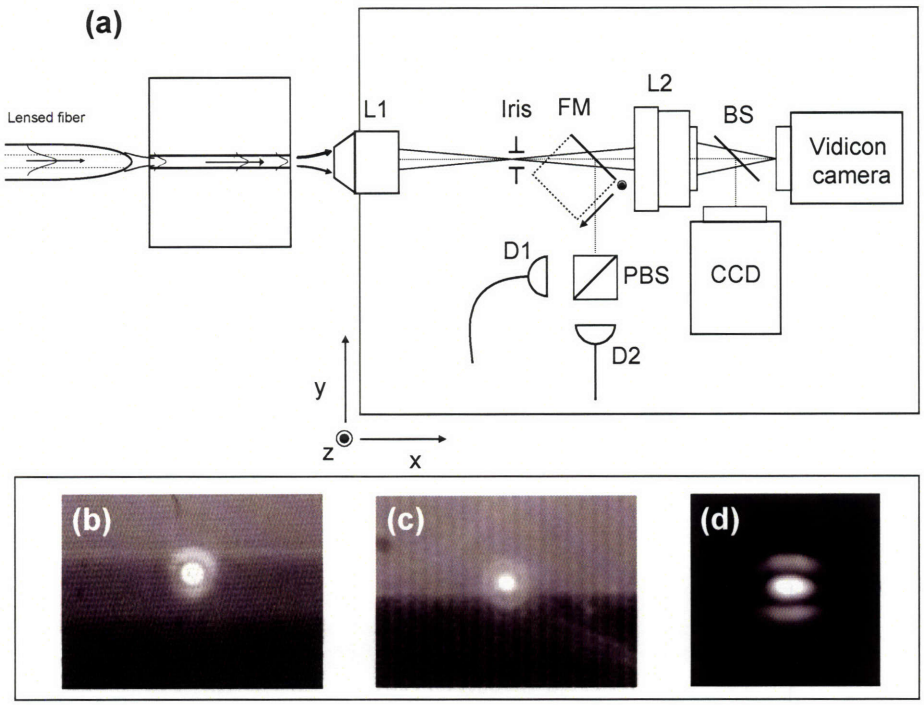

Figure 3.16: (a) Diagram of free space imaging apparatus. (b) Free-space modal image obtained from overclad waveguide mode with white light illumination. (c) Mode of unclad GaAs waveguide. (d) Mode of ridge waveguide.

system to image the waveguide output facet to dual-camera imaging system employing both Vidicon and CCD cameras. The Vidicon camera (S1 photo cathode) responds to telecom wavelengths (albeit poorly) enabling modal images to be formed with as little as $\sim$1 nW of power. However, due to the slow response and poor contrast facilitated by Vidicon imaging, we employ a CCD camera in parallel. This enables visible imaging of the waveguide endfacet with resolution that is often good enough to identify the waveguide anatomy. Some example images can be seen in Fig. 3.16b-d. It should be noted; however, that

simultaneous imaging over a broad range of wavelengths (400-1600nm) requires careful choice of optics. In this case, a multi-element Ealing reflecting-objective (L1) was used to the eliminate chromatic dispersion in the imaging apparatus.

This imaging technique has the advantage that it enables video-rate imaging of the waveguide mode as the laser is tuned, which is useful to identify modal beating. Furthermore, through use of spatial filtering (with the iris) and actuation of the flip mirror (FM) one can switch between imaging and signal detection effortlessly. This form of free-space signal collection enables unambiguous polarization analysis of the detected signal. However, due to the nonlinearity of the S1 photo-cathode response and the poor uniformity of vidicon response, it is difficult to use this imaging method for anything other than qualitative diagnostic purposes.

3.6.3 Scanning confocal imaging

With scanning confocal imaging methods high performance solid-state detectors can be employed, enabling a great deal more quantitative information to be obtained from modal images. For the study of waveguides, confocal imaging was performed with the use of single-mode lensed fibers for both waveguide excitation and collection as seen in Fig. **3.17**c. This experimental geometry is practical since it allows us to easily switch between spectral measurement and imaging. Images are formed by scanning the collection with position-calibrated piezo translation stages as the signal is detected with an InGaAs detector and lockin amplifier.

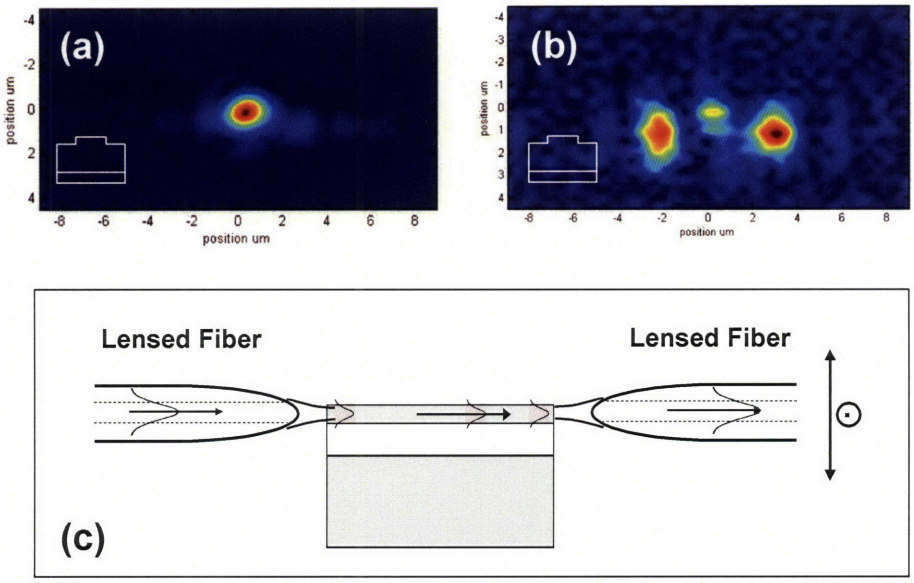

Figure 3.17: (a) Confocal image at the output of a ridge waveguide for TE excitation (b) Similar image for TM excitation (c) Illustration of confocal imaging method performed with lensed fibers.

Two example modal images obtained through confocal imaging can be seen in Figs. 3.17a-b. As can be seen, both fundamental and higher order modes were identifiable through this method as the polarization is changed between TE and TM.

3.6.4 Laser based measurements of HIC devices

In the study of high extinction multi-stage ring resonator filters, such as those described in sections 3.3-3.4, the key problems are: (1) identification of the polarization eigenstates of the microring and waveguide, (2) reduction of laser ASE for high contrast notch filter measurement and (3) accurate wavelength calibration of the laser line. In this section we explain these problems in the

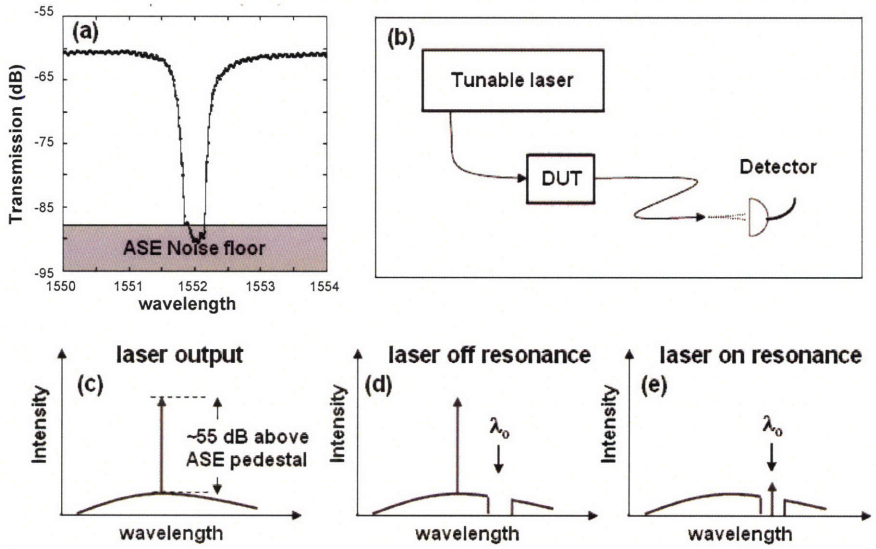

Figure 3.18: (a) An integrated-power transmission spectrum of a multi-stage filter demostrating an erronious extinction of 28 dB. (b) Diagram of power-transmission method (c) Typical power-spectrum at output of laser, illustrating a narrow laser line and an ASE pedestal. (d) Laser power-spectrum when tuned away from notch-filter resonance (e) Laser power-spectrum when on-resonance.

context of HIC device studies, and describe the solutions that we have devised through our studies.

In performing high-resolution transmission measurements, tunable laser sources are widely implemented due to their unparalleled brightness and versatility. The simplest approach to obtaining a transmission measurement of an optical device is through power transmission measurements in the configuration seen in Fig. 3.18b. However, in the study of high extinction notch filters, such as the multi-stage third-order filters, the precise form of the laser linewidth begins to play a role. If we imagine integrating the total power transmitted through a high extinction notch filter, we can see that the ASE pedestal of the laser output will

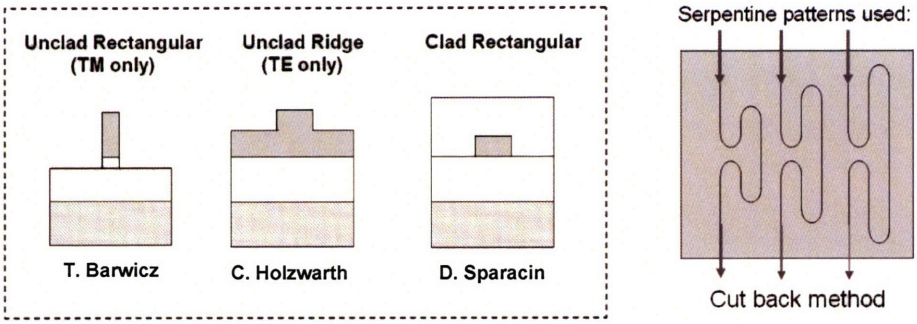

Figure 3.13: (Left) Crossections of the various waveguides used to perform cut-back loss measurements. (Right) Schematic of serpentine patterns used to vary the length of a waveguide segment for cut-back measurements.

silicon-nitride has a higher refractive index (from ellipsometry measurements) due to the lower energy band-edge produced by the increased silicon content. However, the impact that this silicon content has on the absorptive properties at telecom wavelengths was unclear, as little had been published on this matter.

Over the course of this project, we have applied a number of measurement techniques to the study of the high silicon-content SiN films, including microring resonators based loss measurements, Fabry-Perot loss measurements, imaging techniques, and cut-back measurements. Comments on and discussion of these techniques can be found in appendix **D**. However, the most useful and reliable technique was found to be the cut-back method, which we describe briefly here. The cutback method (or paper-clip method) simply refers to a series of power transmission measurements through waveguides of differing lengths. The first waveguides studied in low-index-contrast could not tolerate significant

the larger refractive index becomes. Silica, for example has an absorption band in the UV, resulting in an index of refraction of 1.445 at 1550 nm.

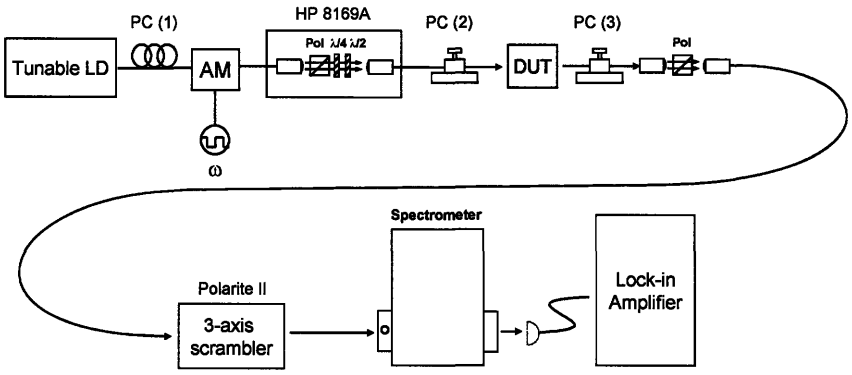

Figure 3.19: A simplified schematic of the laser-based measurement apparatus for study of multi-stage filters and the OADM. The tunable laser diode (LD) is passed through a polarizatoin controller (PC1) before a chopper (AM). PC(1) aligns the polarization with the Glan-Thomposon polarizer inside of the HP8169A, enabling a polarization purity of ~50dB. Through control of the waveplates in the HP8169A orthogonal states can be generated. PC(2) then allows mapping of these states to the device eigenstates. Analysis is performed by PC(3) and another polarizer(POL). A three-axis piezo polarization scrambler precedes the spectrometer in order to remove polarizaiton dependence before the light is detected.

3.19. The tunable laser (Photonetics Tunics) source is first passed polarization controller (HP 8169A) to generate high-purity polarization states. A second strain-type (Polarite) polarization controller is used to transform the orthogonal states of the polarization controller to eigenstates of the integrated circuit. At the output of the device, light is collected with a second lensed fiber, and analyzed with use of a second polarization controller and polarizer. The transmitted power is then passed through a resonant polarization scrambler and spectrally filtered with a monochromator (Acton 500i) which is synchronously tuned with the laser. Laser light is then collected with a TE-cooled InGaAs detector and lock-in detected (EG&G 7220) permitting noise floors of 400 fW and lower.

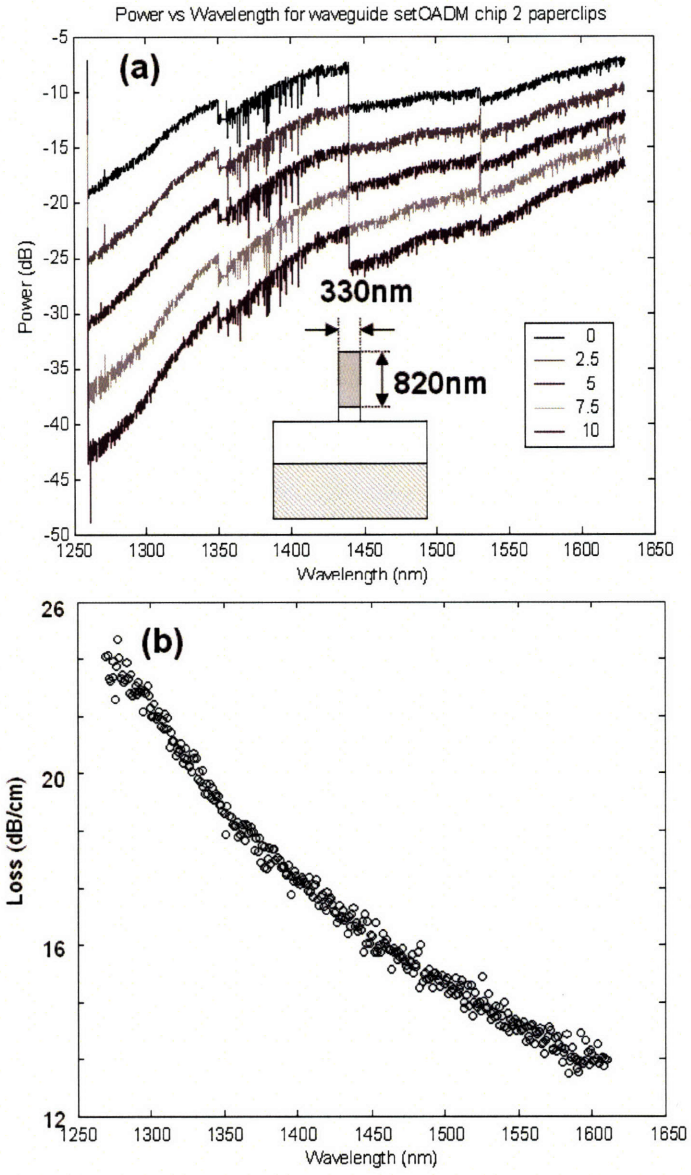

Figure 3.14: (a) Power transmission measurements obtained through serpentine waveguides of the crossection seen in inset. Decreasing transmission (dB) can be seen as the differential guide length is increased from 0-10 mm. (b) Computed waveguide loss (dB/cm) extracted from power transmisison measurements displayed in (a). Each circle is the result of a linear fit of power transmission vs length (5 points in each fit). [Waveguide fabrication by Tymon Barwicz]

detector. This reduces the impact that the laser ASE pedestal has on the measurement of the through port and makes possible measurements with extinction of greater than 50 dB (see for example Fig **3.7**). The polarization scrambler preceding the monochromator was necessary to average out the polarization dependent loss (PDL) produced by the grating within the monochromator.

3.7 Conclusions

In conclusion, we have described studies of HIC microphotonic circuits suitable for telecommunications networks, utilizing cascaded microring resonator filters. Through laser-based measurement techniques, higher order corrections to our ring frequencies were identified and corrected through fabrication. The results are some of the most remarkable filter performance attained to date in HIC microphotonics. Despite the high performance of these microring filters, they exhibit severe polarization sensitivities, rendering them useless in real fiber-optic telecom networks. However, through integration of identical sets of microring filters in a polarization diversity scheme, we have shown that the polarization dependence of such devices can be virtually eliminated, and complex functional HIC optical circuits achieved.

Chapter 4

Widely tunable photonic microcavities via evanescent field perturbation

4.1 Introduction

The field of integrated optics promises to provide a practical and scalable means of routing and switching light for applications ranging from telecommunication networks to sensing and spectroscopy. However, the problem of producing large waveguide effective-index changes (Δn_{eff}) presents a key barrier to the development of dynamic integrated optical circuits. Large Δn_{eff}'s are critical for the development of widely tunable filters and for scaling active components to smaller size. Currently, thermo-optical tuning is the only widely implemented means of producing Δn_{eff} in integrated circuits [**61**, **62**, **63**], but it has insuf-

ficient range and is slower than desired for many applications.

In this chapter we examine a means of producing Δn_{eff} through changes in waveguide geometry as an alternative to changes in material properties. Geometrical tuning mechanisms, such as evanescent tuning, present a number of possible advantages over thermo-optical tuning. Evanescent tuning can enable much larger changes in waveguide effective index, doesn't require significant power dissipation, and can enable switching speeds which far exceed those typically possible through thermal tuning. Although, our research will show that a MEMS based approach to evanescent tuning is very promising, we find that it is not without its complexities; and numerous problems must be addressed before effective real-world implementation.

In what follows, we describe a method for laboratory-based study of evanescent tuning, compare our experimental tuning results with a rigorous theoretical model to estimate the tuning, and discuss some of the complexities that must be tackled to utilize evanescent and other geometrical tuning mechanisms to their fullest extent. Through tuning experiments it is found that high-fidelity ultra-wide tunablility of optical micro-cavities can be achieved through evanescent perturbation. In what follows, a 1.7 % frequency shift is demonstrated (or 27 nm tuning at 1565 nm) in a microring resonator without resolvable distortion of the cavity resonance. Furthermore, complete recovery of the resonance is found when the perturbing body is removed. Approximately 80 separate tuning trials produced similar results, without observable modification of the microring. Experiments are carried out with a novel silica fiber-probe which provides access

to the evanescent field of an air-clad high index-contrast (HIC) ring resonator mode. As the probe is advanced toward the ring resonator, the probe-ring distance is found through simultaneous nano-metric distance calibration and force measurements [**64**].

4.2 Evanescent field-perturbation

In the experimental studies that follow, we examine perturbation of an unclad microring resonator with a uniform silica perturbing body (n = 1.45), whose dimension can be approximated by a dielectric half-space (for example see Fig **4.1**). Before describing experiments, we first perform a brief analysis of the effect of evanescent perturbation on n_{eff} of an unclad waveguide mode and relate this to a change in resonance frequency of a microcavity.

4.2.1 Perturbation of guided modes

The evanescent tuning concept that we examine is rather simple, and its essence is captured by the sketches of Fig. **4.1**. Fig. **4.1** depicts a dielectric waveguide of rectangular cross-section, supporting a TE-like waveguide mode. In the absence of any perturbations, the guided mode has an effective index n_{eff} (Fig 4-1a). A perturbation of the waveguide mode is generated by placing a dielectric slab in the evanescent field of the waveguide mode. This changes its effective index from n_{eff} to $n'_{eff} \approx n_{eff} + \Delta n$. Since the effective index of a waveguide mode can, in general, be expressed by the overlap integral of its electric field

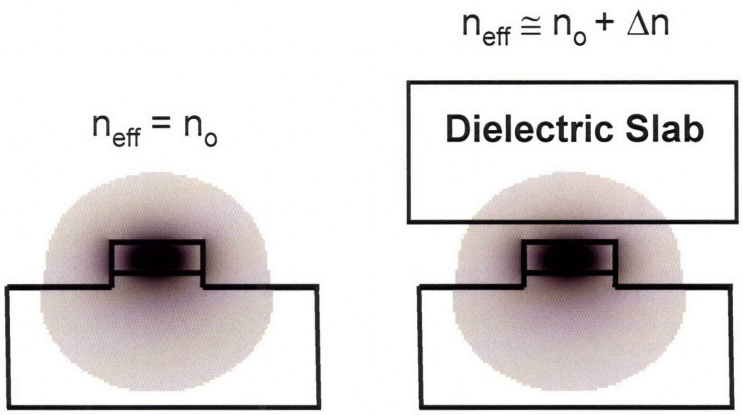

Figure 4.1: Diagram illustrating the first order correction to the effective index of a 'tightly bound' waveguide mode when a dielectric body is placed in the evanescent field of an unclad waveguide. The salient points being that the magnitude of the index change depends on the spatial overlap ( ) and the index of the perturbing structure (nslab).

components with the material index $n(x, y)$ over all space [59]. Clearly, if we place a dielectric body in evanescent field of the waveguide mode, its effective index will change. The basic questions that we must address are: (1) What effect does this type of perturbation have on the mode? (2) How large of an effective index change can be expected? (3) How large of a perturbation (tuning) can be tolerated without severely distorting the mode?

If the dielectric slab acts as a modest perturbation on the waveguide mode (i.e. modification of the modal shape is negligible), one can properly estimate the new effective index through scalar first-order perturbation theory as, $n'_{eff} \approx n_{eff} + \frac{\beta}{2n_{eff}}$*. For a more detailed discussion of scalar perturbation theory see [12, 59]. However, as the n_{slab} increases it will have a larger im-

*Here $\beta =$ (overlap of the mode with the dielectric slab)$\times(n^2_{slab} - 1)$.

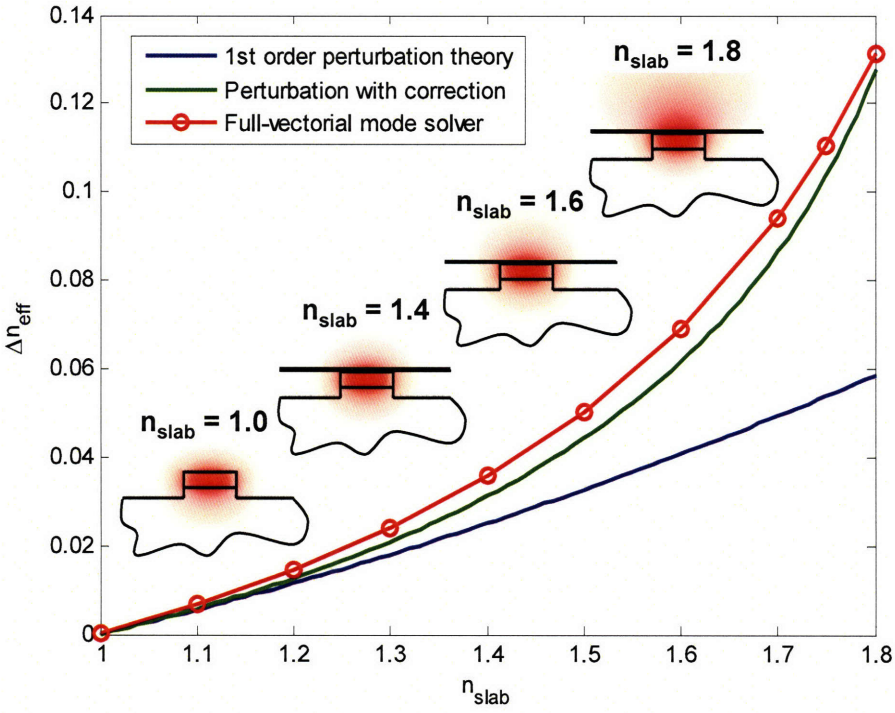

Figure 4.2: Computed change in effective index induced by evanescent perturbation. The perturbing dielectric slab is assumed to be in flush contact with the top surface of waveguide. Full-vectorial computations (red circles) perturbation theory (blue) and improved approximation (green) are compared above.

pact on the guided mode, resulting in deviation from the first order correction. The computed $\Delta n_{eff,max}$ produced through evanescent perturbation of a silicon nitride waveguide is shown in Fig. 4.2 as a function of n_{slab} for various computation methods. The waveguide under study is assumed to have a core index of 2.2 and core dimensions $w = 1050nm, h = 325nm$, and possesses a single TE-like mode over telecom wavelengths. Computations obtained with

a full-vectorial mode solver[†] (red circles) and through first order perturbation theory (blue solid) are shown. One can immediately see that for $n_{slab} = 1.2$ significant deviation from first order perturbation theory is observed. This is because the perturbing slab alters the mode shape, resulting in an increased penetration length in the upper half-space representing the probe. See for example the computed mode profiles inset in Fig. **4.2**. To first order, this penetration length can be estimated through phase-matching at the upper boundary of the waveguide. This simple estimate yields a decay length of[‡]

$$\alpha_{slab}(n_{slab}) = k\sqrt{n_{eff}^2 - n_{slab}^2}. \tag{4.1}$$

As n_{slab} increased, this tells us that the modal penetration into the slab will increase. Interestingly, we can use this relation to construct a correction factor to our first order perturbation theory. If the core of our waveguide were infinite in lateral extend (i.e. a planar waveguide), the overlap integral with the perturbing slab will scale as $1/\alpha(n_{slab})$. Therefore a correction factor of $\alpha(n = 1)/\alpha(n_{slab})$ to our first order computation seems physically justified. Applying this correction factor, we find markedly improved agreement with the full-vectorial computation (green curve). Therefore, to obtain a reasonable approximation of the range of Δn_{eff} induced through evanescent tuning, it appears that one need only know the fractional mode overlap of the unperturbed waveguide with the slab, and n_{eff} of the guided mode.

[†]Special thanks to Michael Watts and Milos Popovic for use of their mode solver.
[‡]For examples see [**4**, **12**]

4.2.2 Tuning of cavities

Next, we examine the wavelength tuning ($\Delta\lambda$) that is produced by the computed Δn_{eff} found above. As it turns out, the resonance wavelength as a function of the slab-ring separation (z) can be approximated from the effective index (n_{eff}) and the group index (n_{group}) of the perturbed waveguide mode through a simple perturbative expansion. This is described next.

One can begin this analysis by noting that the resonance condition of the ring mode is, $\phi(n_{eff}, \lambda) = kn_{eff}L = 2\pi m$ where $\phi(n_{eff}, \lambda)$ is the round trip phase, k, L and m are the free-space wave number, the path-length of the ring, and an integer, respectively. If we think of perturbing the cavity mode by changing the cavity index by some amount Δn_{eff} such that the new cavity effective index is $n_{eff}^{'} \equiv n_{eff} + \Delta n_{eff}$, the m^{th} cavity mode will be shifted to different wavelength $\lambda^{'} \equiv \lambda + \Delta\lambda$. The round trip phase of the perturbed system is denoted as $\phi^{'}(n_{eff}^{'}, \lambda^{'})$. Therefore the round trip phase of the perturbed cavity can be approximated as

$$\phi^{'}(n_{eff}^{'}, \lambda^{'}) \approxeq \phi(n_{eff}, \lambda) + \frac{\partial\phi}{\partial n}\Delta n_{eff} + \frac{\partial\phi}{\partial\lambda}\Delta\lambda = 2\pi m \tag{4.2}$$

through first order Taylor expansion. Since the round trip phase of the m^{th} cavity mode is always $2\pi m$, it must be the case that

$$\frac{\partial\phi}{\partial n}\Delta n_{eff} + \frac{\partial\phi}{\partial\lambda}\Delta\lambda = 0. \tag{4.3}$$

Therefore we can solve for the shift in wavelength experienced by the cavity resonance using the definition of $\phi(n_{eff}, \lambda)$, yielding

$$\frac{\partial\lambda}{\lambda} \approxeq \frac{\Delta n_{eff}}{n_{eff} - \lambda\frac{\partial n_{eff}}{\partial\lambda}} = \frac{\Delta n_{eff}}{n_{group}}. \tag{4.4}$$

Here, $\Delta n_{eff}(z)$ is the change in effective index induced by the perturbing slab. Therefore Eq. (3) can be used to evaluate the tuning range made possible by the Δn_{eff}. displayed in Fig. **4.3**. The results of these computations can be seen in Fig. **4.3**.

Upon examination of Fig. **4.3** we see that a tuning range of ~80 nm is achievable at the expense of modal confinement. However, since we first seek to perform a simple laboratory demonstration of evanescent tuning, we will confine our study to the case of a silica perturbing body (indicated by the dashed line of Fig. **4.3**).

4.2.3 Theoretical tuning of HIC microring

For the purposes of this study, a silicon-nitride ring resonator of the type described in chapter 3, but of first order, is considered. The ring resonator, designed for operation at 1.5 μm wavelengths, with an free-spectral-range of 27 nm. The transmitted (through-port) and resonantly dropped powers (drop-port) are shown as a function of wavelength in Fig. **4.4**. The mode of the air-clad ring resonator has an evanescent-field extending outside the guide in the direction normal to the plane of the ring such that dielectric body can uni-

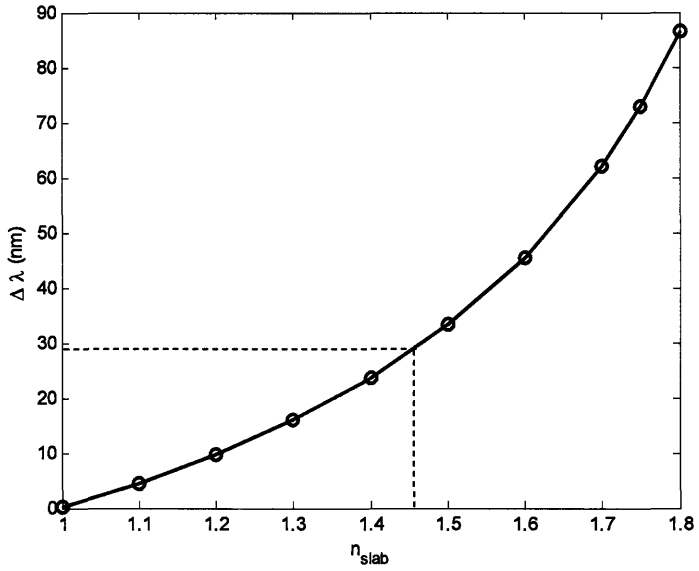

Figure 4.3: Plot of maximum possible wavelength tuning achievable through evanescent perturbation versus slab-index. Dashed line indicates the tuning obtainable with a silica (n = 1.45) perturbing body.

formly penetrates the evanescent field of the ring. See, for example, the inset of Fig. **4.3**). This produces an increase in effective-index of the mode, resulting in a shift of resonance frequency.

With a similar set of computations with a full-vectorial mode solver and Eq. **4.4** the wavelength tuning versus the height of the perturbing slab (z) can be computed. The results of the perturbative computation plotted in Fig. **4.5** show a maximum theoretical tuning range of 28.5 nm at an operating wavelength of 1565 nm. The computed wavelength shift closely approximates an exponential, with a decay length of $1/\alpha = 89.3$ nm, making it evident that a nano-metric of positional control is required. This turns out to be one of the key challenges surrounding implementation of evanescent tuning, since in many cases, a high

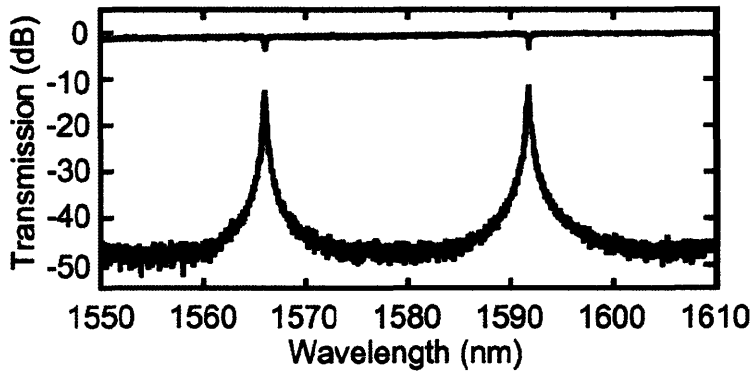

Figure 4.4: Thru response (upper) and drop response (lower) of the large FSR silicon-nitride ring resonator used for evanescent tuning study.

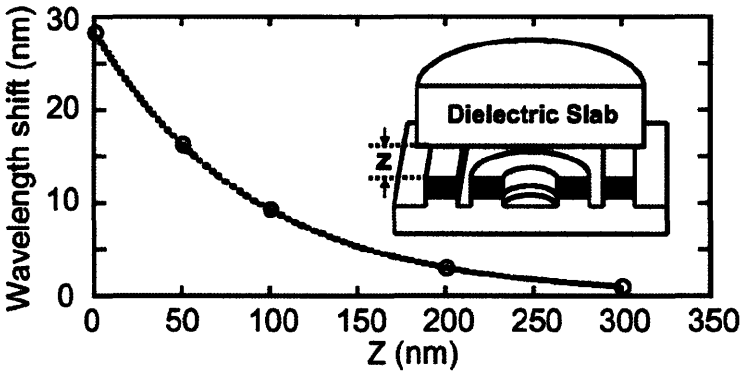

Figure 4.5: Wavelength shift (nm) induced in a microring microcavity versus separation of perturbing slab from waveguide surface (z). Inset depicts geometry under study. Computed tunings are displayed as circles while dashed line indicates exponential fit of tuning.

degree of wavelength control translates to a remarkable degree of positional control of the perturbing slab.

4.3 Evanescent tuning experiments

In laboratory implementation of evanescent tuning, we can imagine using a probe of small dimension to perturb this microring in a fashion approximating to that shown above. Although the short decay length of the electric field above the ring results in a rapid change in cavity resonance with position, requiring nanometric control, a more serious challenge in laboratory implementation of this geometry is the high degree of angular alignment required between the perturbing body and the ring resonator. For example, if a probe of 100 μm dimension is used to perturb our ring resonator (diameter 14 μm) in a nearly ideal fashion, it must lie parallel to the lithographic surface within $\sim$100 μrad. In initial studies of evanescent tuning, numerous attempts to perturb the ring with a rigid probe and active alignment were only moderately successful, yielding tuning ranges which were a fraction of the theoretical tuning (2-10 nm tuning ranges).

4.3.1 Probe fabrication

Ultimately, the angular alignment issue was addressed through a passive alignment method utilizing the novel probe design illustrated in Fig **4.6**. It exploits a flexible fiber-taper near the end of the probe, which allows the fiber end to

lie parallel to the surface when it comes in contact with the substrate of the ring resonator. The fabrication process for this probe is outlined in inset of Fig **4.6**. First, the fiber (125 μm diameter) is tapered to several microns to form a flexible joint. Then the face of the probe (used to perturb the ring resonator) is formed by a fiber cleave and annealed until a small amount of glass reflow occurs. Glass reflow ensures ensuring an ultra-smooth surface with which the microring can be perturbed and eliminates topological defects that can be formed in the cleaving process.

4.3.2 Tuning apparatus

The apparatus developed to perform evanescent perturbation experiments can be seen in Fig **4.7**. It consists of the silica fiber probe (described above), which is mounted on a 5 cm long cantilever having a force constant of $\sim$5000 N/m. The probe cantilever assembly is mounted on a distance-calibrated piezo translation stage such that it can be brought in and out of contact with the ring-resonator device. Motion of the cantilever and probe relative to the device is monitored with a Fabry-Perot fiber interferometer, one end of which is formed by the cantilever. Position is read through rapid interrogation of the interferometer with white-light from an erbium-doped fiber amplifier (EDFA) and an optical spectrum analyzer (OSA). The force experienced by the probe can be precisely measured from the cantilever deflection (obtained from the difference between the interferometer and stage displacements). Broadband EDFA light is also coupled into and collected from the ring resonator device with lensed fibers.

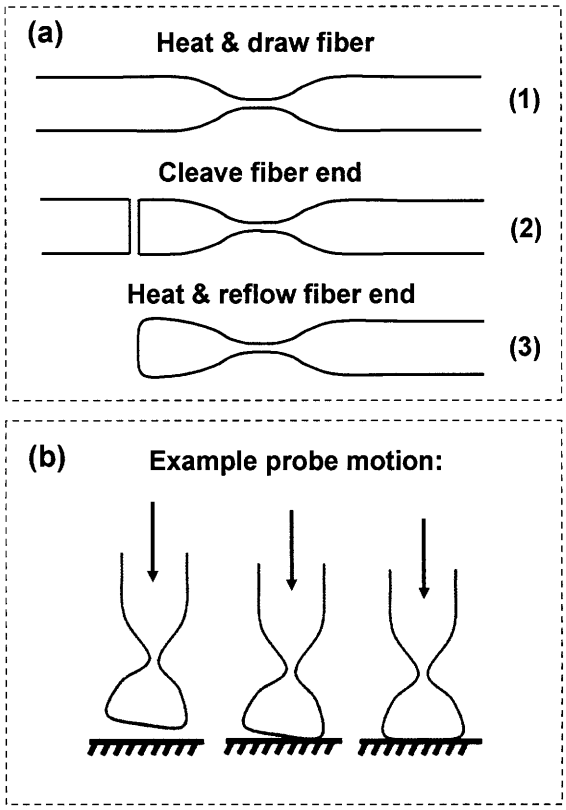

Figure 4.6: (a) probe fabrication process (1) silica fiber is heated and tapered to several microns in dimension, (2) the fiber is then cleaved forming a flat surface (3) reflow of the fiber end is performed through an anneal. (b) An example of the probe 'auto-alignment' motion as it contacts the surface of a substrate.

Rapid spectral acquisitions ($\sim 100\mu$sec snapshots) of the ring drop response are taken with a monochromator and InGaAs camera. Rapid measurement was necessary to resolve the ring resonance, as cantilever vibrations tended to distort the resonance when measured on longer time scales. Experiments were performed by simultaneously measuring the ring resonator drop response, cantilever position, and forces of probe-sample interaction.

The Fabry-Perot interferometer, used for distance calibration, is formed between a cleaved fiber-optic and a glass substrate on which the fiber-probe is mounted. Interrogation of the interferometer was performed by measuring the Fabry-Perot response in reflection with broadband EDFA (1530-1610 nm) light and the OSA. A change in position of the cantilever relative to the device results in a phase-shift of fringe pattern of the interferogram. Therefore, an FFT algorithm can be used to recover of the fringe-pattern phase-shift and thus the relative motion of the cantilever. Although the throughput of the interferometer was poor ($\sim$%5), rapid spectral scans with 5 mW of EDFA light were sufficient to enable position measurements with an accuracy of 0.2-2 nm at refresh times of 2-0.2 seconds.

With use of the tapered fiber probes described above, the angular alignment of the perturbing body with the surface of the microring is vastly improved. Fig **4.7**(b) shows a series of drop spectra that were obtained as microring tuning takes place. The solid trace shows the unperturbed drop-port response. As the probe is advanced toward the microring a series of red-shifted drop-port responses are seen (dashed traces) until a maximum tuning of $\sim$27 nm occurs. After this point, further advancement doesn't result in further tuning. These observations are strong evidence that evanescent tuning is taking place. A more complete picture of what is occurring at the ring-surface can be formed through careful analysis of resonance wavelength, displacement and the forces applied by the probe.

The results of a tuning experiment including simultaneous acquisition of

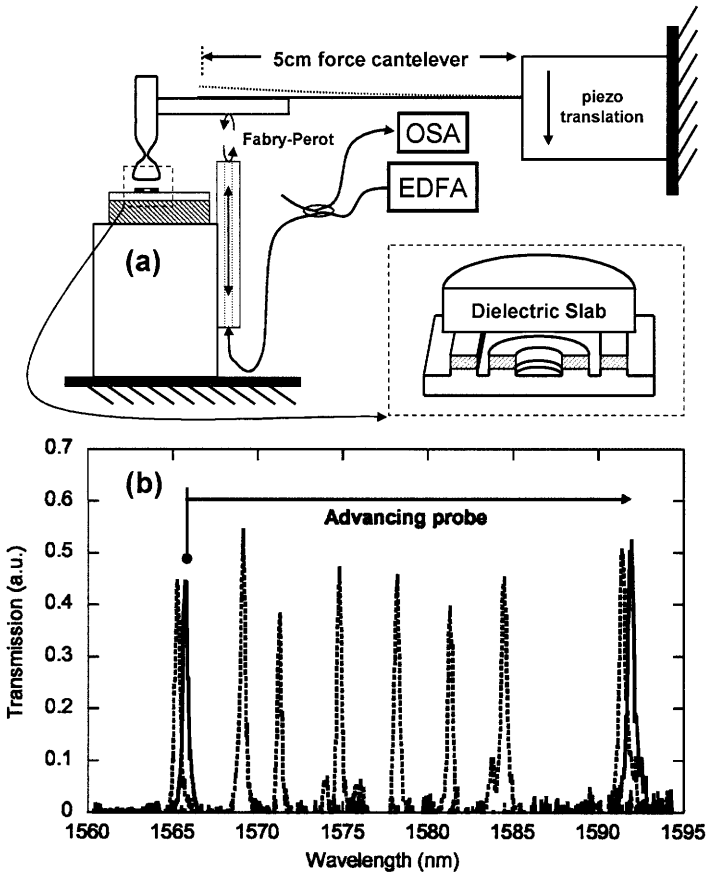

Figure 4.7: (a) Apparatus used to perform evanescent tuning. Tapered fiber probe is mounted on the end of a 5 cm force cantilever such that it can be brought in and out of contact with the top surface of the microring resonator with a distance calibrated piezo stage. The motion of the probe relative to the microring is monitored with a Fabry-Perot interferometer. Interferometer is interrogated with white light from an erbium doped amplifier (EDFA) and an optical spectrum analyzer (OSA). (b) Characteristic drop resonance measurements obtained at 100 sec intervals with InGaAs CCD camera, as probe is advanced toward ring resonator. Solid traces are unperturbed resonances. Dashed traces show various tunings as probe advances toward ring.

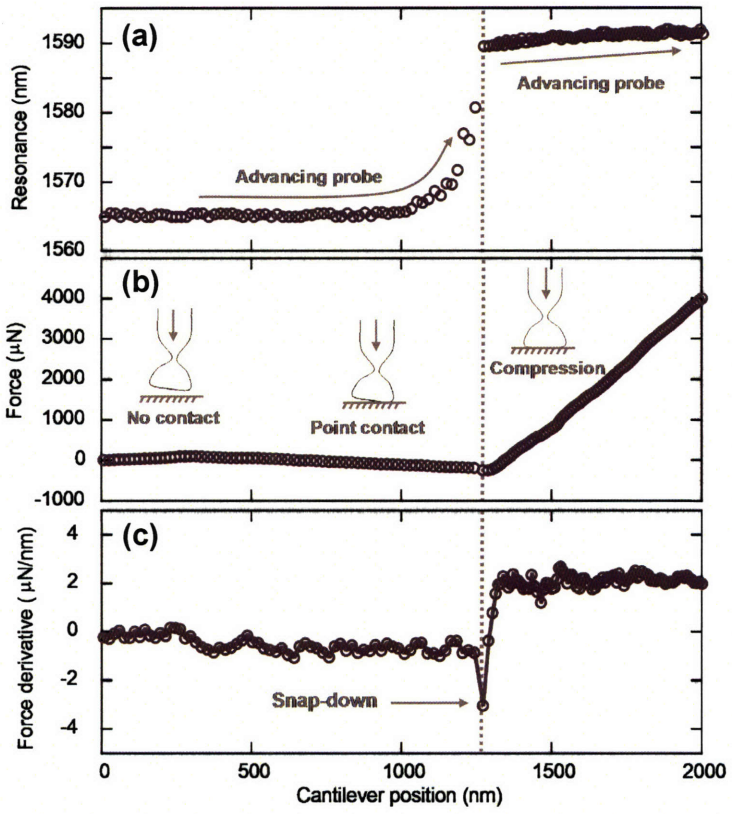

Figure 4.8: (a) Measured resonance frequency of ring resonator (obtained from drop response) as a function of cantilever displacement (measured by interferometer). (b) Force of probe-ring interaction (circles) vs interferometer position measurement (for comparison with (a)). Two regimes of probe behavior are identified: (1) tilting of the probe (2) flush contact resulting in compression of the probe. Fig. 3(c) is the derivative of the force. The sharp discontinuity at 1270 nm, indicates snap-down of the probe due to attractive forces

these data are shown in Figs **4.8**(a)-(c). Fig. **4.8** (a) shows the ring resonance frequency as a function of the cantilever height measured by the interferometer. Each data point (circle) represents the resonant wavelength obtained from a drop port measurement of the ring resonator. The force and force derivative experienced by the probe over the same range of cantilever displacement are displayed in Fig. **4.8**(b-c). In Fig. **4.8**(a) two trends can be seen: (1) for smaller positions (i.e. position 1270 nm) an exponential change in resonance wavelength occurs over a 25 nm tuning, (2) for positions larger than 1270 nm (indicated by the vertical dashed line) there is a very gradual change in ring resonance frequency. In interpreting these two tuning regimes, the forces of interaction between the probe and sample (seen in Fig. **4.8**(b)) provide insight. Over the exponential tuning regime attractive forces (negative in sign) are experienced by the probe. These are likely due to a combination of capillary and Van der Waals interactions as the probe approaches flush contact [**65**]. Snap down of the probe can be seen at 1270 nm most clearly through a sharp decrease in the derivative of the force, corresponding to the maximum in the exponential portion of the tuning curve. After this point, the probe remains flush with the surface of the device, resulting in compression of the probe, which is seen as large positive slope in the force curve. It should be noted that in all cases the forces applied are far smaller than those required to generate a commensurate strain-based tuning.

Using the snap-down position found from the force and force derivative measurements, the probe-ring distance can be placed on an absolute scale and

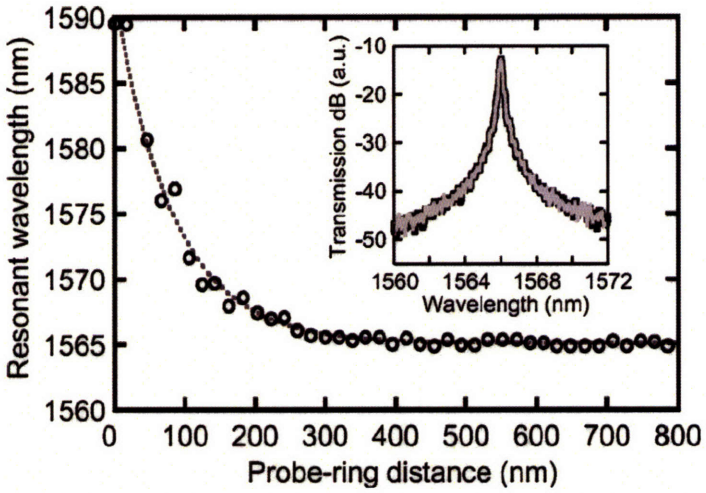

Figure 4.9: (a) Measured tuning versus distance from probe snap-down (circles) with exponential fit (dash). Inset: high resolution drop-port measurement before and after tuning experiment.

	Theory	Expt.
$1/\alpha$	~91 nm	87±4 nm
$\Delta\lambda_{max}$	30 nm	27 nm

Figure 4.10: table comparing experimental and theoretical tuning range and decay length.

compared with theory, as seen in Fig. **4.9**. An exponential fit of the tuning versus probe ring-distance reveals a decay length of 87 ± 4 nm and a maximum tuning of 24.8 nm, which agrees with the theoretical decay length of 89.3 nm and maximum tuning range of 28.5 nm. Tunings, of as much as 27 nm, were also obtainable by contacting the ring using unique points of the probe face, indicating that conformation of the probe surface plays a role in limiting the maximum perturbation possible. It is important to note that throughout the tuning process the resonance shape appears to be roughly preserved. Variations in amplitude of the dropped signal, seen in Fig. **4.7**(b), are more likely a result of the poor signal-to-noise experienced when acquiring spectra at these speeds. Additionally, when the fiber is raised again the unperturbed resonance is fully recovered (inset Fig. **4.9**), demonstrating a negligible degree of hysteresis, suggesting no material exchange between the probe and ring.

4.3.3 Probe asymmetry and maximum tuning

Once the probe is attached to the end of the cantilever, it could be contacted to the ring surface with impunity. This is because the cantilever is very effective at limiting the forces applied to the microring, making it is very difficult to damage the microring or the probe. With the use of the InGaAs CCD for rapid spectral acquisitions of the drop-port and the piezo stage to advance the cantilever-probe assembly, tuning of the microring could be observed in real-time. This allowed a systematic maximization of the tuning with transverse motion of the probe. It was found that at a unique point, 30-40 microns from the probe center, a

maximum tuning of 27 nm was achievable. A characteristic tuning curve versus position is shown in Fig. **4.11**.

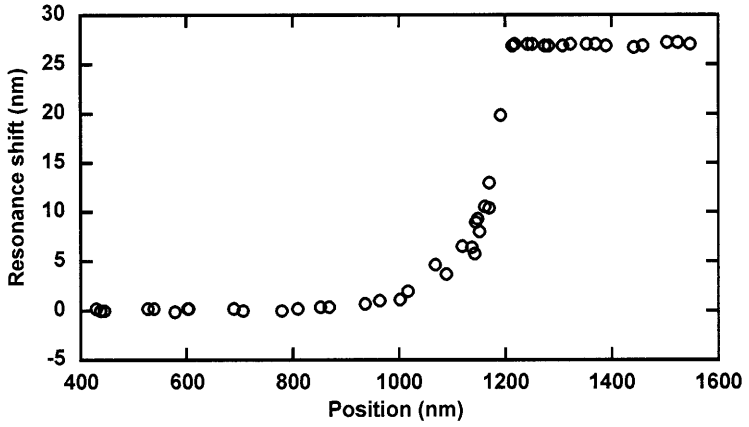

Figure 4.11: Plot of wavelength versus position demonstrating maximum wavelength tuning obtained when probe is off-center.

These unique 'sweet spots' the probe surface, resulting increased tuning, are likely a result of slight asymmetries in the probe topology formed during glass reflow of the probe surface. Both the tapering and the reflow steps (ie. 1 & 3) were performed in a fusion splicer (Ericson fusion splicer). As the degree of reflow of the probe end was increased (to a point that wasn't desirable for use in a this experiment), excessive asymmetries could be observed due to nonsymmetrical heating of the fiber during reflow. This was the maximum tuning obtainable in the laboratory, but unfortunately since the probe center doesn't coincide with the ring center, the height of the dielectric from the ring surface cannot be trivially related to the interferometer displacement. This makes it difficult to use data runs taken off-center to quantify the decay length of the electric field from the microring. However, it is interesting to note that

when operating at this special 'sweet spot', the ring frequency remains static as further advancement of the probe is made. Whereas, when the probe is advanced on the probe center (away from the sweet spot), the tuning appears to increase very gradually after contact. This is a strong piece of anecdotal evidence, indicating that a small change in probe conformation occurs until further probe advancement.

4.3.4 Probe-surface interactions

In earlier experiments, it was first obvious that the probe was interacting with the ring surface when the tuning of the drop-port resonance was measured. While advancing the probe toward the ring surface it appeared that the ring resonant wavelength would consistently make a discrete hop over the last 7-10 nm of its tuning range. After this point, the ring would remain stable at the maximum tuning, indicating that the probe is flush with the surface of the ring. Removal of the probe from the ring surface would require $\sim$ 2-5 mN of force. Later, these discrete hops in position were quantified through simultaneous acquisition of forces (seen in Fig. **4.8**). It isn't a surprise that the probe is attracted to the surface of the microring. Such attractive forces are to be expected, and have recently been quantified and studied great deal, since they constitute a big problem for the operation of MEMS devices. Our goal here is to understand the nature of these forces and determine if they can be mitigated to some degree, because they could seriously hinder the performance of the class of optical MEMS devices that we studied here.

4.4 Conclusions

In conclusion, high-fidelity reversible tuning was demonstrated over 1.7% frequency range through evanescent tuning of a microring. In this experiment, a uniform silica perturbing body was used, although, it should be noted that with a higher-index perturbing structures, a 3% tuning could be implemented through the same range of motion. Furthermore, higher index-contrast waveguides, such as silicon, can tolerate stronger perturbation before coupling to radiation modes occurs and should permit considerably larger tuning ranges. It is also important to note that evanescent tuning would be equally effective in a photonic crystal platform. Ultimately, MEMS implementation of this tuning mechanism through a device of the type described in Ref. [**66**] would be ideal, as it would require negligible power dissipation, and could enable rapid switching times (micro - nanosecond). However, the attractive forces between the perturbing body and the ring-surface must be mitigated to ensure that snap down does not disrupt the device behavior. Additionally, due to the sensitivity of this tuning mechanism to the position of the perturbing body, careful consideration of thermally induced vibrations must be made in designing a MEMS device [**67**, **68**].

Bibliography

[1] J. D. Joannopoulos, Robert D. Meade, and Joshua N. Winn. *Photonic crystals : molding the flow of light.* Princeton University Press, Princeton, N.J., 1995. John D. Joannopoulos, Robert D. Meade, Joshua N. Winn. ill. (some col.) ; 25 cm. [cited at p. 8, 17]

[2] Steven G. Johnson and J. D. Joannopoulos. *Photonic crystals : the road from theory to practice.* Kluwer Academic Publishers, Boston, 2002. [cited at p. 8, 17]

[3] Kazuaki Sakoda. *Optical properties of photonic crystals.* Springer, Berlin ; New York, 2nd edition, 2004. [cited at p. 8, 17, 24]

[4] Katsunari Okamoto. *Fundamentals of optical waveguides.* Elsevier Academic Press, Burlington, MA, 2nd edition, 2006. Katsunari Okamoto. ill. ; 24 cm. 1. Wave theory of optical waveguides – 2. Planar optical waveguides – 3. Optical fibers – 4. Coupled mode theory – 5. Nonlinear optical effects in optical fibers – 6. Finite element method – 7. Beam propagation method – 8. Staircase concatenation method – 9. Planar lightwave circuits – 10. Several important theorems and formulas. [cited at p. 8, 11, 18, 80, 81, 120, 163]

[5] H. Kosaka, T. Kawashima, A. Tomita, M. Notomi, T. Tamamura, T. Sato, and S. Kawakami. Self-collimating phenomena in photonic crystals. *Applied Physics Letters*, 74(9):1212–1214, 1999. Times Cited: 64. [cited at p. 9]

[6] H. Kosaka, T. Kawashima, A. Tomita, T. Sato, and S. Kawakami. Photonic-crystal spot-size converter. *Applied Physics Letters*, 76(3):268–270, 2000. Times 2. [cited at p. 9]

[7] L. J. Wu, M. Mazilu, and T. F. Krauss. Beam steering in planar-photonic crystals: From superprism to supercollimator. *Journal of Lightwave Technology*, 21(2):561–566, 2003. [cited at p. 9]

[8] D. W. Prather, S. Y. Shi, D. M. Pustai, C. H. Chen, S. Venkataraman, A. Sharkawy, G. J. Schneider, and J. Murakowski. Dispersion-based optical routing in photonic crystals. *Optics Letters*, 29(1):50–52, 2004. [cited at p. 9]

[9] D. M. Pustai, S. Y. Shi, C. H. Chen, A. Sharkawy, and D. W. Prather. Analysis of splitters for self-collimated beams in planar photonic crystals. *Optics Express*, 12(9):1823–1831, 2004. Times Cited: 3. [cited at p. 9]

[10] S. Y. Shi, A. Sharkawy, C. H. Chen, D. M. Pustai, and D. W. Prather. Dispersion-based beam splitter in photonic crystals. *Optics Letters*, 29(6):617–619, 2004. [cited at p. 9]

[11] X. F. Yu and S. H. Fan. Bends and splitters for self-collimated beams in photonic crystals. *Applied Physics Letters*, 83(16):3251–3253, 2003. [cited at p. 9]

[12] Hermann A. Haus. *Waves and fields in optoelectronics*. Prentice-Hall series in solid state physical electronics. Prentice-Hall, Englewood Cliffs, NJ, 1984. Hermann A. Haus. ill. ; 24 cm. "The introductory graduate course 'Optics and optical electronics,' the notes of which developed into this book, was taught jointly by Professor S. Ezekiel and the author"– P. xii. [cited at p. 11, 84, 118, 120]

[13] Joseph W. Goodman. *Introduction to Fourier optics*. Roberts & Co., Englewood, Colo., 3rd edition, 2005. Joseph W. Goodman. Fourier optics ill. ; 24 cm. [cited at p. 11, 34, 163]

[14] John David Jackson. *Classical electrodynamics*. Wiley, New York, 3rd edition, 1999. John David Jackson. ill. ; 26 cm. [cited at p. 11]

[15] S. G. Johnson and J. D. Joannopoulos. Block-iterative frequency-domain methods for maxwell's equations in a planewave basis. *Optics Express*, 8(3):173–190, 2001. [cited at p. 17, 71]

[16] S. G. Johnson, M. I. Povinelli, M. Soljacic, A. Karalis, S. Jacobs, and J. D. Joannopoulos. Roughness losses and volume-current methods in photonic-crystal waveguides. *Applied Physics B-Lasers and Optics*, 81(2-3):283–293, 2005. Times Cited: 4 Article English Cited References Count: 48 947dq. [cited at p. 28]

[17] S. Bourzeix, J. M. Moison, F. Mignard, F. Barthe, A. C. Boccara, C. Licoppe, B. Mersali, M. Allovon, and A. Bruno. Near-field optical imaging of light propagation in semiconductor waveguide structures. *Applied Physics Letters*, 73(8):1035–1037, 1998. [cited at p. 52]

[18] N. Axelrod, A. Lewis, N. Ben Yosef, R. Dekhter, G. Fish, and A. Krol. Small-focus integral fiber lenses: modeling with the segmented beam-propagation

method and near-field characterization. *Applied Optics*, 44(7):1270–1282, 2005. [cited at p. 57]

[19] T. Yamashita and C.J. Summers. Evaluation of self-collimated beams in photonic crystals for optical interconnect. *IEEE Journal on Selected Areas in Communications*, 23(7):1341–7, 2005. [cited at p. 59]

[20] P. T. Rakich, M. S. Dahlem, S. Tandon, M. Ibanescu, M. Soljacic, G. S. Petrich, J. D. Joannopoulos, L. A. Kolodziejski, and E. P. Ippen. Achieving centimetre-scale supercollimation in a large-area two-dimensional photonic crystal. *Nature Materials*, 5(2):93–96, 2006. Times Cited: 1 Article English Cited References Count: 13 008sc. [cited at p. 59]

[21] P. T. Rakich, H. Sotobayashi, J. T. Gopinath, S. G. Johnson, J. W. Sickler, C. W. Wong, J. D. Joannopoulos, and E. P. Ippen. Nano-scale photonic crystal microcavity characterization with an all-fiber based 1.2-2.0 mu m supercontinuum. *Optics Express*, 13(3):821–825, 2005. [cited at p. 62, 63]

[22] Peter T. Rakich, Juliet T. Gopinath, Hideyuki Sotobayashi, Chee Wei Wong, Steven G. Johnson, John D. Joannopoulos, and Erich P. Ippen. Broadband supercontinuum based measurements of high-index contrast photonic bandgap devices from 1 to 2 microns. In *2004 IEEE LEOS Annual Meeting Conference Proceedings, LEOS 2004, Nov 7-11 2004*, volume 2 of *Conference Proceedings - Lasers and Electro-Optics Society Annual Meeting-LEOS*, pages 813–814, Rio Grande, Puerto Rico, 2004. Institute of Electrical and Electronics Engineers Inc., Piscataway, NJ 08855-1331, United States. [cited at p. 62, 74]

[23] M. H. Qi, E. Lidorikis, P. T. Rakich, S. G. Johnson, J. D. Joannopoulos, E. P. Ippen, and H. I. Smith. A three-dimensional optical photonic crystal with designed point defects. *Nature*, 429(6991):538–542, 2004. [cited at p. 62, 63, 70, 73]

[24] M. C. Netti, C. E. Finlayson, J. J. Baumberg, M. D. B. Charlton, M. E. Zoorob, J. S. Wilkinson, and G. J. Parker. Separation of photonic crystal waveguides modes using femtosecond time-of-flight. *Applied Physics Letters*, 81(21):3927–3929, 2002. [cited at p. 62]

[25] Robert R. Alfano. *The supercontinuum laser source : fundamentals with updated references*. Springer, New York, 2nd edition, 2006. [cited at p. 63]

[26] G. P. Agrawal. *Nonlinear fiber optics*. Optics and photonics. Academic Press, San Diego, 3rd edition, 2001. [cited at p. 63, 66]

[27] G. Genty, M. Lehtonen, H. Ludvigsen, J. Broeng, and M. Kaivola. Spectral broadening of femtosecond pulses into continuum radiation in microstructured

fibers. *Optics Express*, 10(20):1083–1098, 2002. Times Cited: 46 Article English Cited References Count: 22 601jk. [cited at p. 63]

[28] T. Ritari, G. Genty, and H. Ludvigsen. Supercontinuum and gas cell in a single microstructured fiber. *Optics Letters*, 30(24):3380–3382, 2005. [cited at p. 63]

[29] J. T. Gopinath, H. F. M. Shen, H. Sotobayashi, E. P. Ippen, T. Hasegawa, T. Nagashima, and N. Sugimoto. Highly nonlinear bismuth-oxide fiber for smooth supercontinuum generation at 1.5 microns. *Optics Express*, 12(23):5697–5702, 2004. [cited at p. 63]

[30] Robert W. Boyd. *Nonlinear optics*. Academic Press, San Diego, CA, 2nd edition, 2003. [cited at p. 66]

[31] M. Lehtonen, G. Genty, H. Ludvigsen, and M. Kaivola. Supercontinuum generation in a highly birefringent microstructured fiber. *Applied Physics Letters*, 82(14):2197–2199, 2003. [cited at p. 66]

[32] N. R. Newbury, B. R. Washburn, K. L. Corwin, and R. S. Windeler. Noise amplification during supercontinuum generation in microstructure fiber. *Optics Letters*, 28(11):944–946, 2003. [cited at p. 66, 68]

[33] Y. Kuroiwa, N. Sugimoto, K. Ochiai, S. Ohara, Y. Fukasawa, S. Ito, S. Tanabe, and T. Hanada. Fusion spliceable and highly efficient bi/sub 2/o/sub 3/-based edf for short-length and broadband application pumped at 1480 nm. In *OFC 2001. Optical Fiber Communication Conference and Exhibition. Technical Digest, 17-22 March 2001*, volume vol.2 of *OFC 2001. Optical Fiber Communication Conference and Exhibit. Technical Digest Postconference Edition (IEEE Cat. 01CH37171)*, pages 5–1, Anaheim, CA, USA, 2001. Opt. Soc. America. [cited at p. 67]

[34] H. A. Haus, K. Tamura, L. E. Nelson, and E. P. Ippen. Stretched-pulse additive-pulse mode-locking in fiber ring lasers - theory and experiment. *Ieee Journal of Quantum Electronics*, 31(3):591–598, 1995. [cited at p. 67]

[35] K. Shiraishi, H. Hatakeyama, H. Matsumoto, and K. Matsumura. Laminated polarizers exhibiting high performance over a wide range of wavelength. *Journal of Lightwave Technology*, 15(6):1042–1050, 1997. [cited at p. 70]

[36] J. S. Foresi, P. R. Villeneuve, J. Ferrera, E. R. Thoen, G. Steinmeyer, S. Fan, J. D. Joannopoulos, L. C. Kimerling, H. I. Smith, and E. P. Ippen. Photonic-bandgap microcavities in optical waveguides. *Nature*, 390(6656):143–145, 1997. [cited at p. 70]

[37] C. W. Wong, P. T. Rakich, S. G. Johnson, M. H. Qi, H. I. Smith, Y. Jeon, G. Barbastathis, S. G. Kim, E. P. Ippen, and L. C. Kimerling. Strain-tunable silicon photonic band gap microcavities in optical waveguides. *Applied Physics Letters*, 84(8):1242–1244, 2004. [cited at p. 70]

[38] K. S. Kunz and R. J. Luebbers. The finite-difference time-domain method for electromagnetics. *(CRC Press: Boca Raton, 1993)*, (CRC Press: Boca Raton, 1993). [cited at p. 71]

[39] Amnon Yariv. *Optical electronics in modern communications*. Oxford University Press, New York, 5th edition, 1997. [cited at p. 80, 81]

[40] G. P. Agrawal. *Lightwave technology : components and devices*. John Wiley, Hoboken, NJ, 2004. [cited at p. 80, 81]

[41] G. P. Agrawal. *Lightwave technology : telecommunication systems*. Wiley-Interscience, Hoboken, N.J., 2005. [cited at p. 80, 81]

[42] Rajiv Ramaswami and Kumar N. Sivarajan. Optical networks a practical perspective, second edition, 2002. [cited at p. 80, 81]

[43] E. A. J. Marcatilli. Bends in optical dielectric waveguides. *Bell System Technical Journal*, 48:2103–2132, 1969. [cited at p. 82, 100]

[44] Kerry Vahala. *Optical microcavities*. Advanced series in applied physics ; v. 5. World Scientific, Singapore ; Hackensack, N.J., 2004. [cited at p. 84, 87, 100]

[45] Y. Yanagase, S. Suzuki, Y. Kokubun, and S. T. Chu. Box-like filter response and expansion of fsr by a vertically triple coupled microring resonator filter. *Journal of Lightwave Technology*, 20(8):1525–1529, 2002. Times Cited: 20 Article English Cited References Count: 13 618ca. [cited at p. 84]

[46] M. A. Popovic, T. Barwicz, M. R. Watts, P. T. Rakich, L. Socci, F. X. Kaertner, H. I. Smith, and E. P. Ippen. Multistage high-order microring-resonator add-drop filters. *(accepted for publication, Optics Letters, May 2006)*. [cited at p. 85, 89, 91, 177]

[47] T. Barwicz, M. A. Popovic, P. T. Rakich, M. R. Watts, H. A. Haus, E. P. Ippen, and H. I. Smith. Microring-resonator-based add-drop filters in sin: fabrication and analysis. *Optics Express*, 12(7):1437–1442, 2004. [cited at p. 87]

[48] Milos Popovi, Massachusetts Institute of Technology. Dept. of Electrical Engineering, and Computer Science. *Air trenches for dense silica integrated optics*. Masters thesis, 2002. [cited at p. 87]

[49] T. Barwicz, M. A. Popovic, M. R. Watts, P. T. Rakich, , E. P. Ippen, and H. I. Smith. Fabrication of add-drop filters based on frequency-matched microring resonators. *Journal of Lightwave Technology*, 24(5):2207–2218, May 2006. [cited at p. 87, 88, 176]

[50] M. A. Popovic, C. Manolatou, and M. R. Watts. Coupling-induced resonance frequency shifts in coupled dielectric multi-cavity filters. *Optics Express*, 14(3):1208–1222, 2006. [cited at p. 87]

[51] S. S. A. Obayya, B. M. A. Rahman, K. T. V. Grattan, and H. A. El-Mikati. Beam propagation modeling of polarization rotation in deeply etched semiconductor bent waveguides. *Ieee Photonics Technology Letters*, 13(7):681–683. Times Cited: 15 Article English Cited References Count: 11 445hl. [cited at p. 90]

[52] F. Morichetti, A. Melloni, and M. Martinelli. Effects of polarization rotation in optical ring-resonator-based devices. *Journal of Lightwave Technology*, 24(1):573–585. Times Cited: 0 Article English Cited References Count: 32 011lv. [cited at p. 90]

[53] E. D. Finlayson, J. M. Heaton, B. M. A. Rahman, and S. S. A. Obayya. Polarization conversion in passive deep-etched gaas/algaas waveguides. *Journal of Lightwave Technology*, 24(3):1425–1432. Times Cited: 0 Article English Cited References Count: 17 022li. [cited at p. 90]

[54] Tymon Barwicz. *Accurate nanofabrication techniques for high-index-contrast microphotonic devices*. PhD thesis, Massachusetts Institute of Technology, Cambridge MA, 02139, September 2005. [cited at p. 90, 102]

[55] M. R. Watts. *Polarization independent microphotonic circuits*. PhD thesis, Massachusetts Institute of Technology, Cambridge MA, 2005. [cited at p. 94]

[56] M. R. Watts and H. A. Haus. Integrated mode-evolution-based polarization rotators. *Optics Letters*, 30(2):138–140, 2005. [cited at p. 94]

[57] M. R. Watts, H. A. Haus, and E. P. Ippen. Integrated mode-evolution-based polarization splitter. *Optics Letters*, 30(9):967–969, 2005. [cited at p. 94]

[58] Minghao Qi, Michael R. Watts, Tymon Barwicz, Peter T. Rakich, Luciano Socci, Erich P. Ippen, and Henry I. Smith. Fabrication of two-layer microphotonic structures without planarization. In *2005 Conference on Lasers and Electro-Optics, CLEO, May 22-27 2005*, volume 2 of *2005 Conference on Lasers and Electro-Optics, CLEO*, pages 1288–1290 BN – 1557527954, Baltimore, MD, United States, 2005. Optical Society of America, Washington, DC 20036-1023, United States. [cited at p. 94]

[59] Charles Vassallo. *Optical waveguide concepts*. Optical wave sciences and technology ; vol. 1. Elsevier, Amsterdam ; New York, 1991. [cited at p. 100, 118]

[60] T. Barwicz and H. A. Haus. Three-dimensional analysis of scattering losses due to sidewall roughness, in microphotonic waveguides. *Journal of Lightwave Technology*, 23(9):2719–2732, 2005. [cited at p. 102]

[61] P. Heimala, P. Katila, J. Aarnio, and A. Heinamaki. Thermally tunable integrated optical ring resonator with poly-si thermistor. *Journal of Lightwave Technology*, 14(10):2260–2267, 1996. [cited at p. 115]

[62] D. Geuzebroek, E. Klein, H. Kelderman, N. Baker, and A. Driessen. Compact wavelength-selective switch for gigabit filtering in access networks. *Ieee Photonics Technology Letters*, 17(2):336–338, 2005. [cited at p. 115]

[63] H. M. H. Chong and R. M. De La Rue. Tuning of photonic crystal waveguide microcavity by thermooptic effect. *IEEE Photonics Technology Letters*, 16(6):1528–1530, 2004. [cited at p. 115]

[64] P.T. Rakich, M.A. Popovic, M.R. Watts, T. Barwicz, H.I. Smith, and E.P. Ippen. Ultrawide tuning of photonic microcavities via evanescent field perturbation. *Optics Letters*, 31(9):1241–3, 2006. [cited at p. 117]

[65] W.M. van Spengen, R. Puers, and I. De Wolf. A physical model to predict stiction in mems. *Journal of Micromechanics and Microengineering*, 12(5):702–13, Sept. 2002. [cited at p. 131]

[66] G.N. Nielson, D. Seneviratne, F. Lopez-Royo, P.T. Rakich, Y. Avrahami, M.R. Watts, H.A. Haus, H.L. Tuller, and G. Barbastathis. Integrated wavelength-selective optical mems switching using ring resonator filters. *Photonics Technology Letters, IEEE*, 17(6):1190–1192, 2005. TY - JOUR. [cited at p. 136]

[67] R.S. Tucker, D.M. Baney, W.V. Sorin, and C.A. Flory. Thermal noise and radiation pressure in mems fabry-perot tunable filters and lasers. *IEEE Journal of Selected Topics in Quantum Electronics*, 8(1):88–97, 2002. [cited at p. 136]

[68] Dror Sarid. *Scanning force microscopy : with applications to electric, magnetic, and atomic forces*. Oxford series in optical and imaging sciences ; 5. Oxford University Press, New York, rev. edition, 1994. [cited at p. 136]

Appendices

Appendix A

Appendix 1A: catalog of experimental images

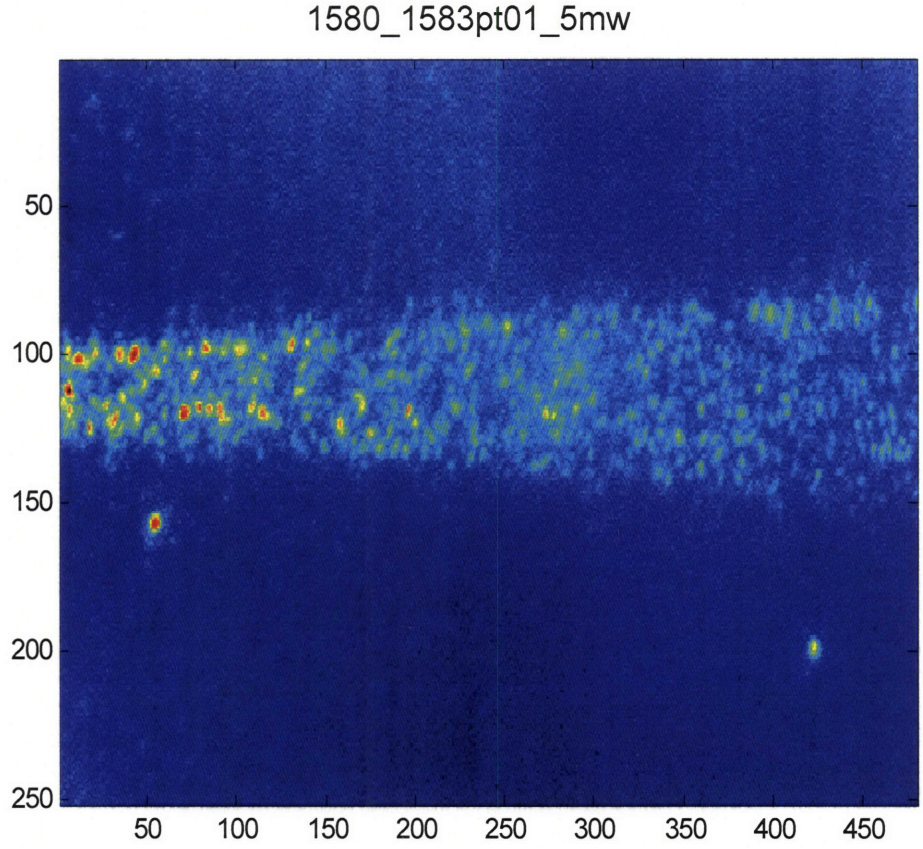

Figure A.1: Experimental scattered light image displayed over a 250 x 500 micron area

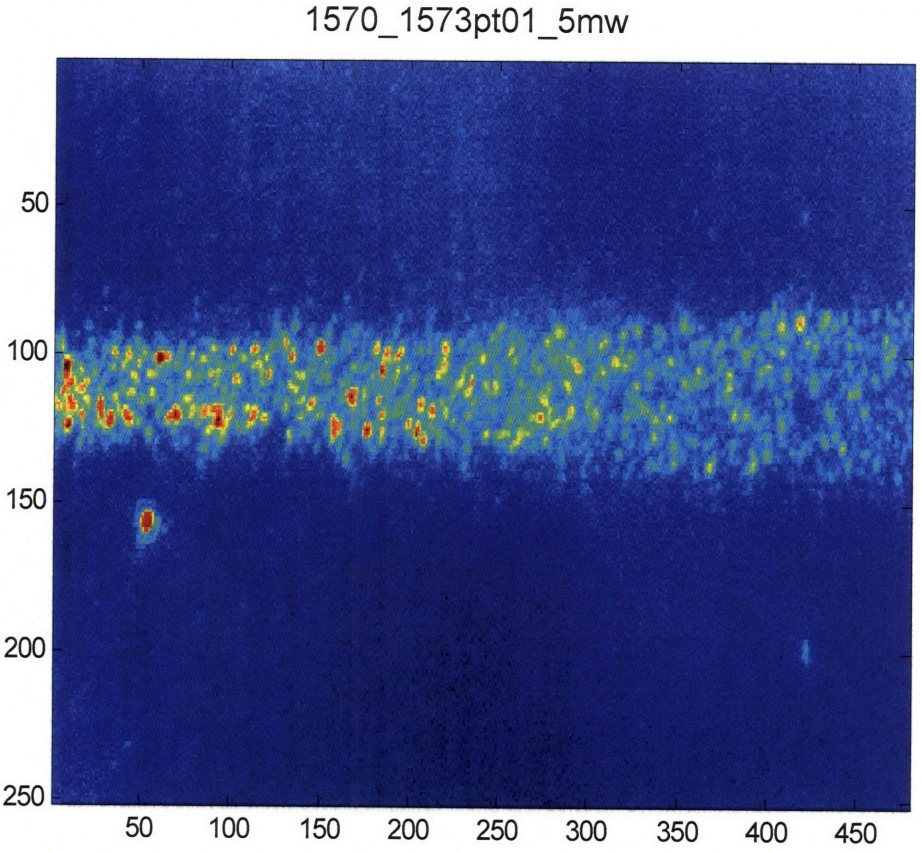

Figure A.2: Experimental scattered light image displayed over a 250 x 500 micron area

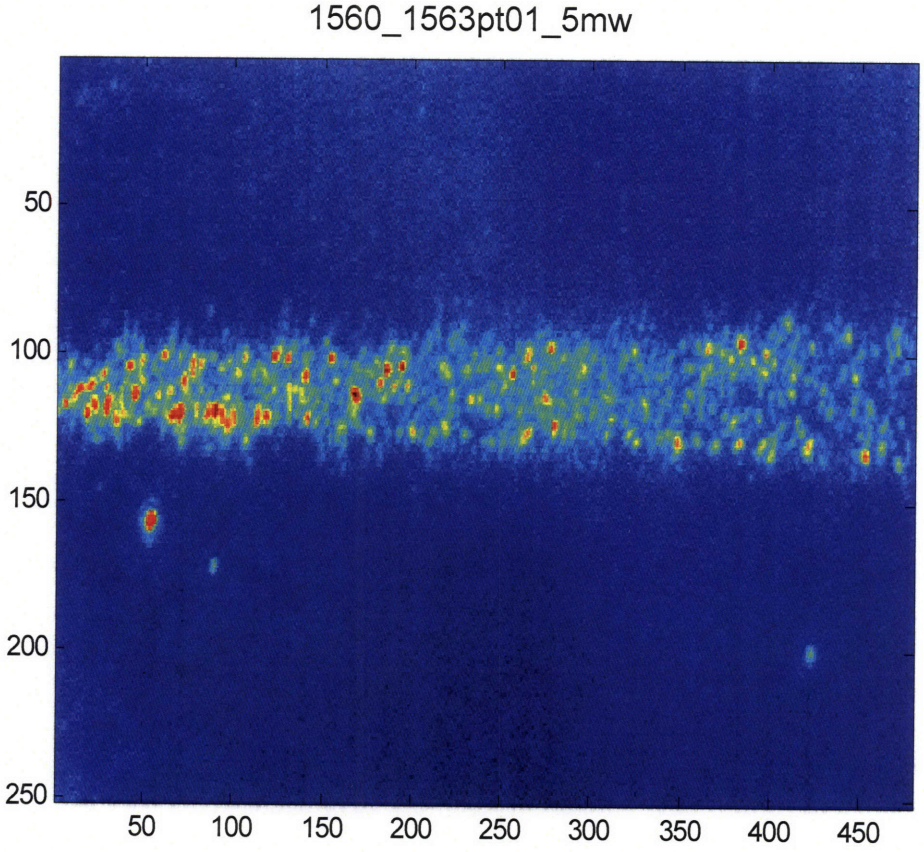

Figure A.3: Experimental scattered light image displayed over a 250 x 500 micron area

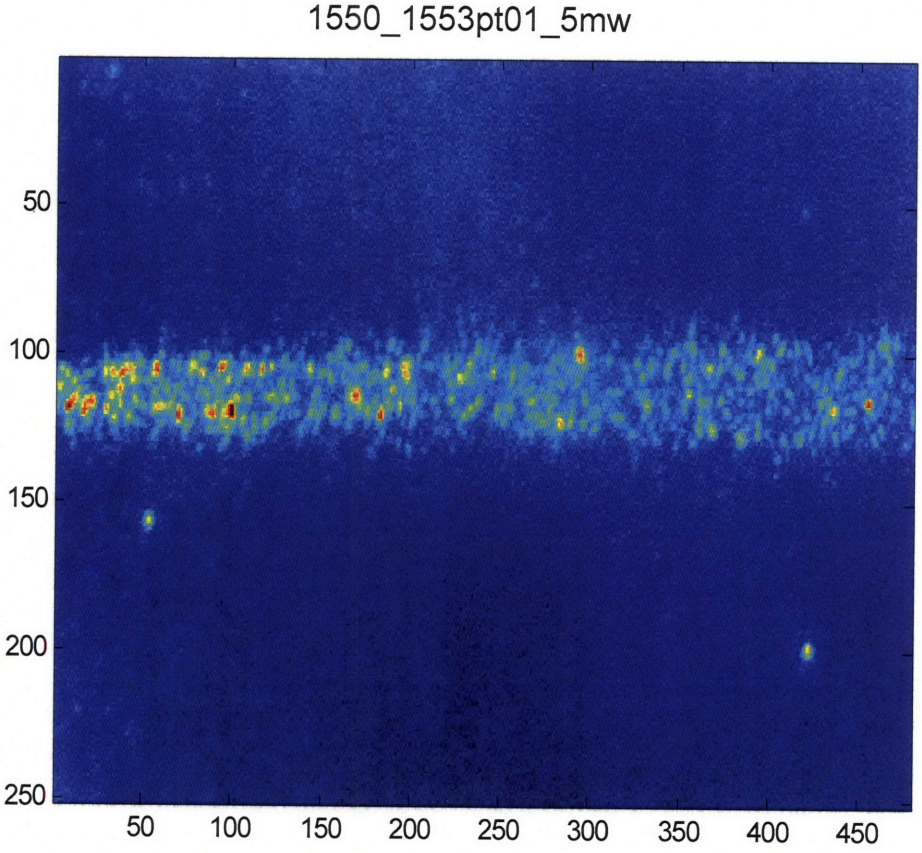

Figure A.4: Experimental scattered light image displayed over a 250 x 500 micron area

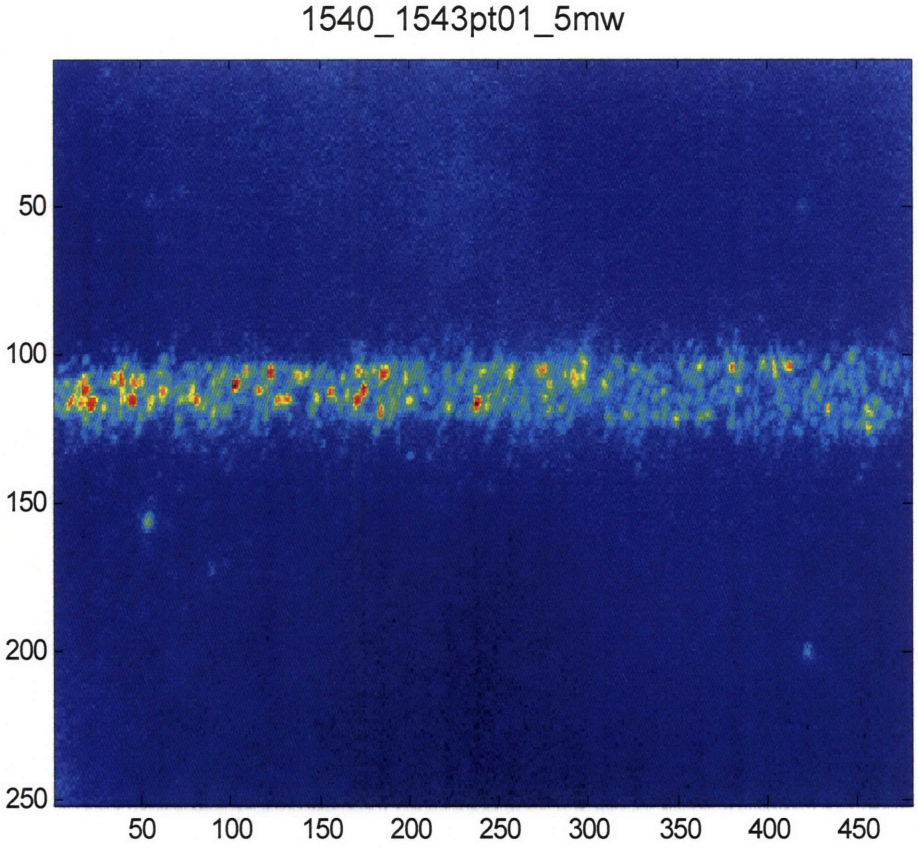

Figure A.5: Experimental scattered light image displayed over a 250 x 500 micron area

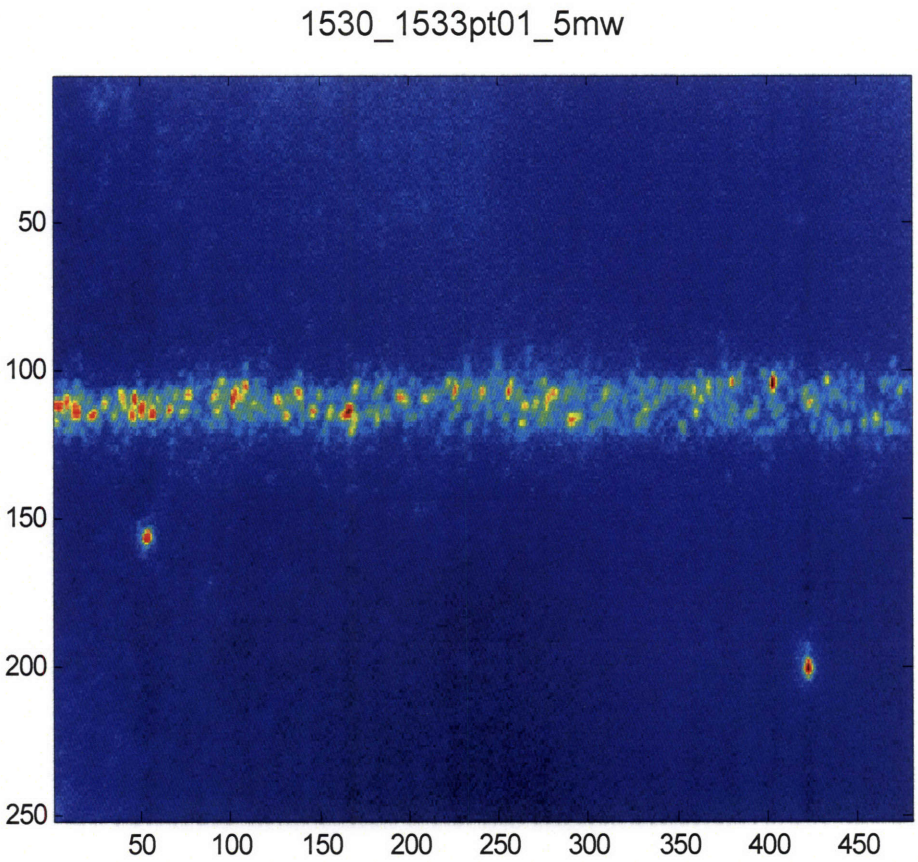

Figure A.6: Experimental scattered light image displayed over a 250 x 500 micron area

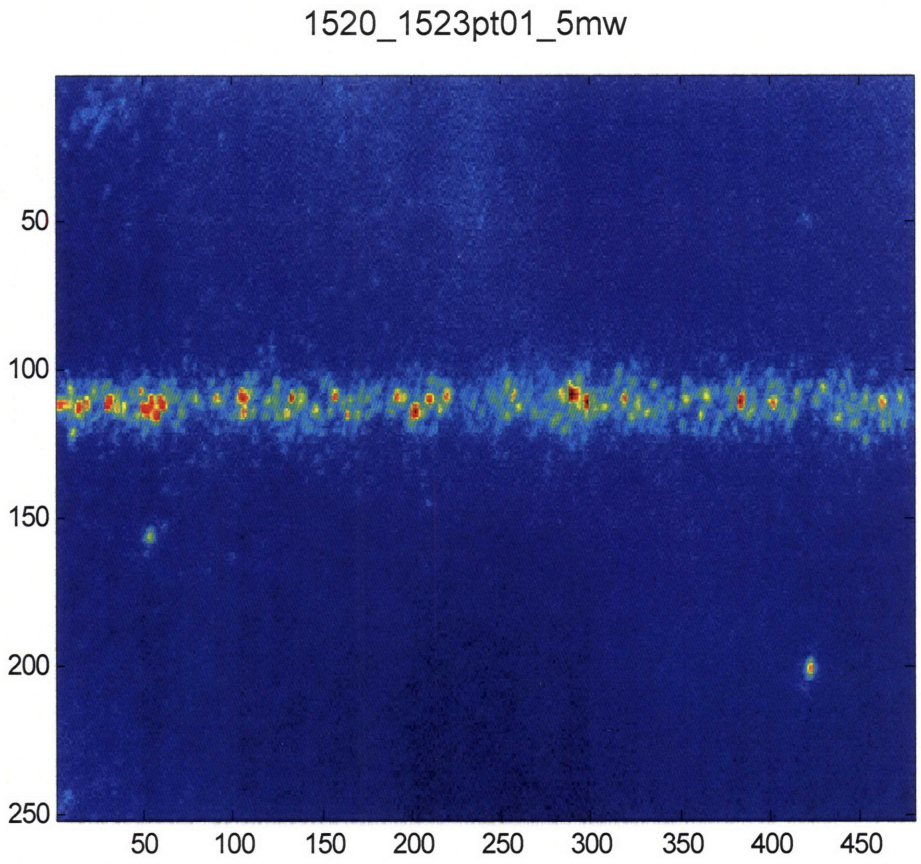

Figure A.7: Experimental scattered light image displayed over a 250 x 500 micron area

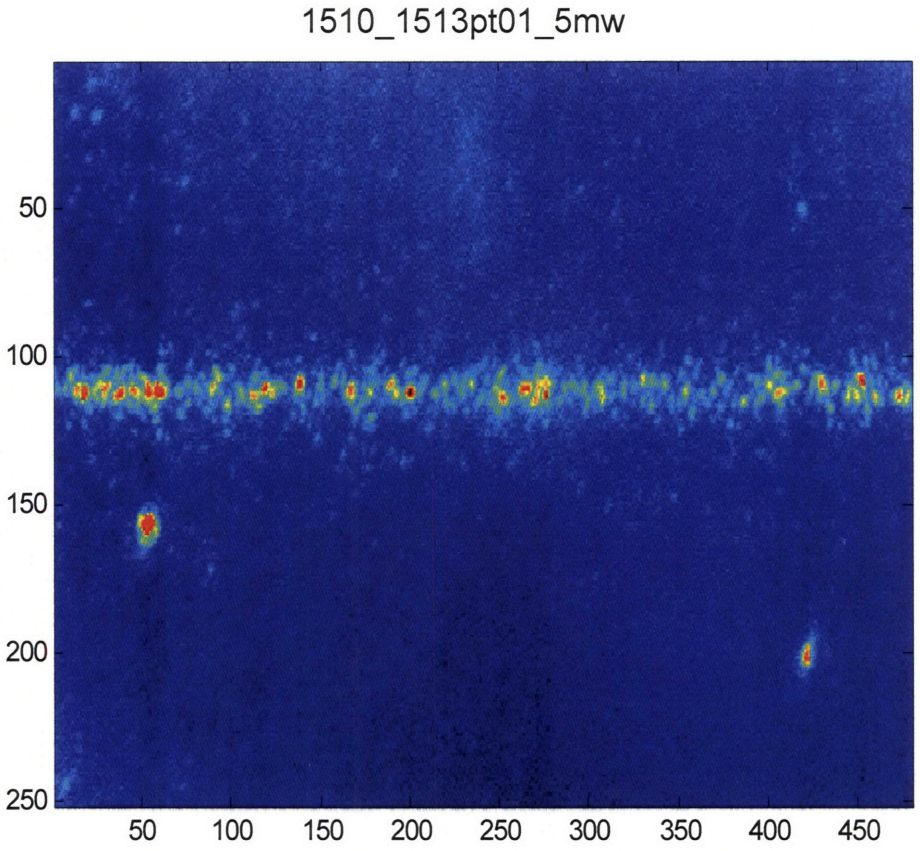

Figure A.8: Experimental scattered light image displayed over a 250 x 500 micron area

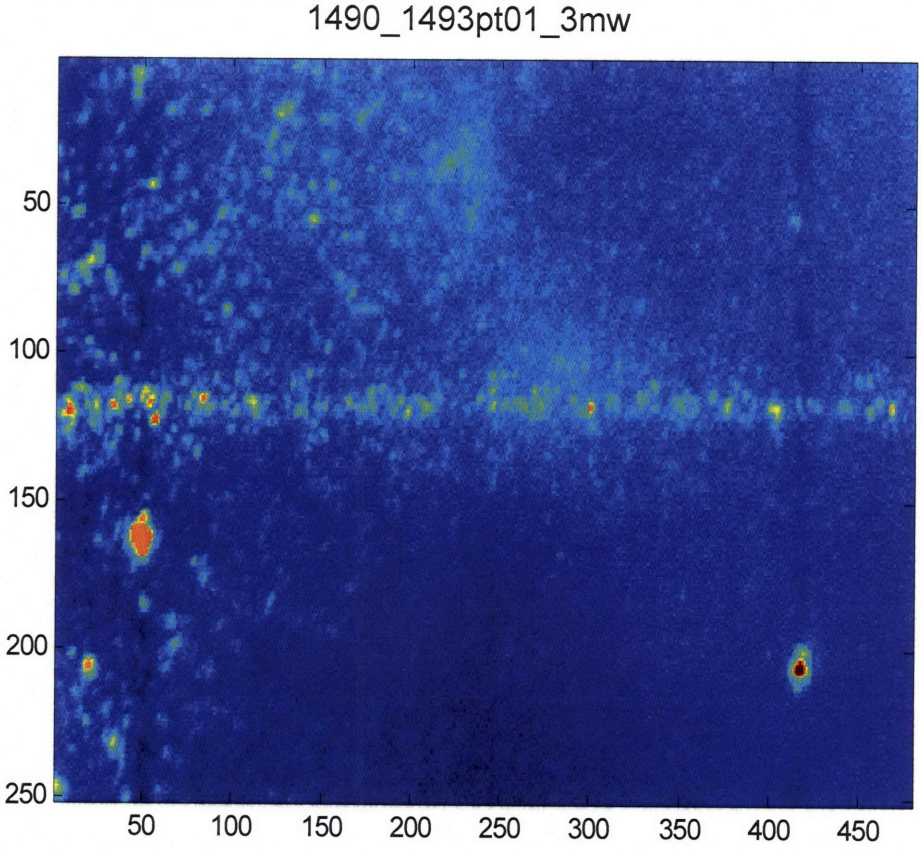

Figure A.9: Experimental scattered light image displayed over a 250 x 500 micron area

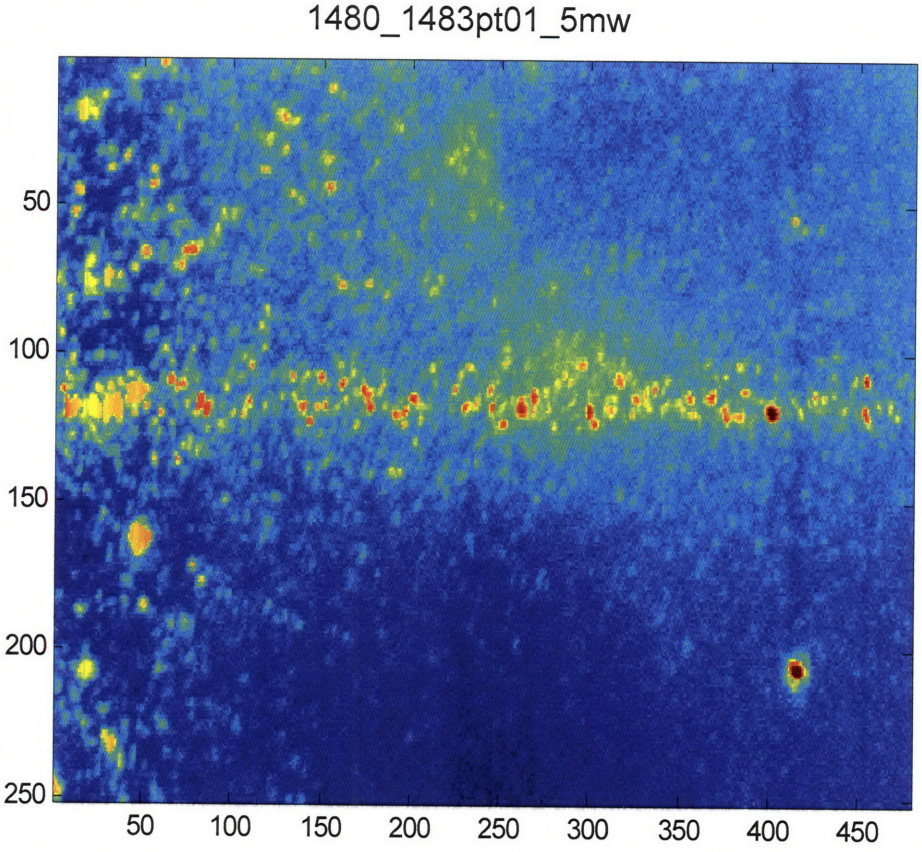

Figure A.10: Experimental scattered light image displayed over a 250 x 500 micron area

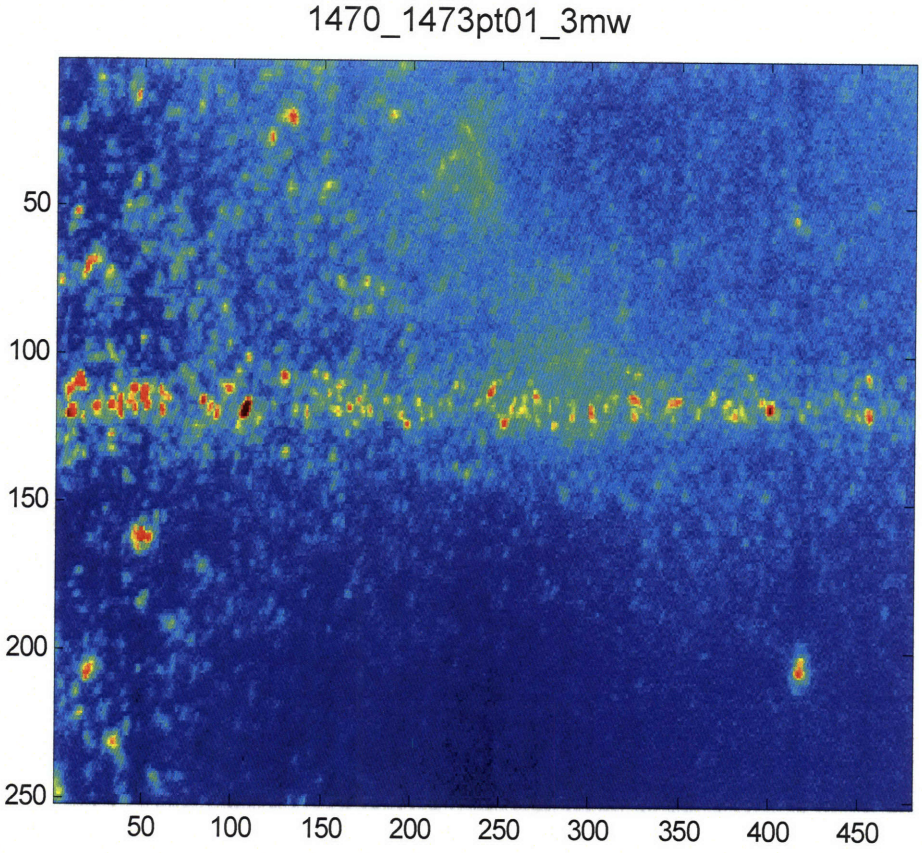

Figure A.11: Experimental scattered light image displayed over a 250 x 500 micron area

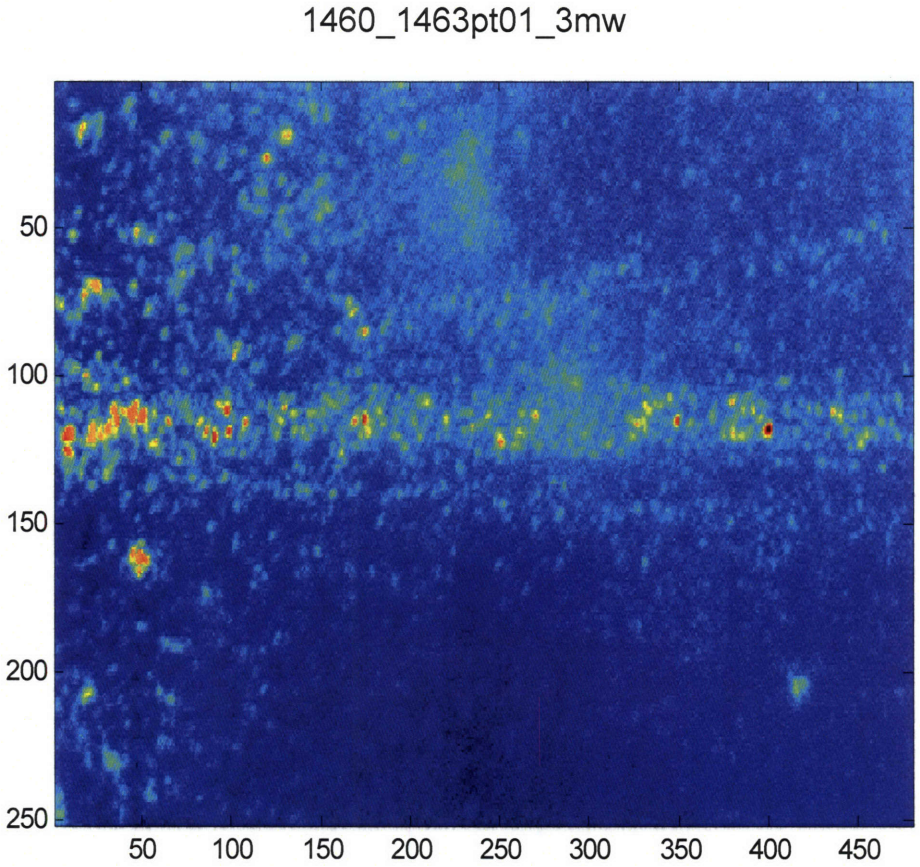

Figure A.12: Experimental scattered light image displayed over a 250 x 500 micron area

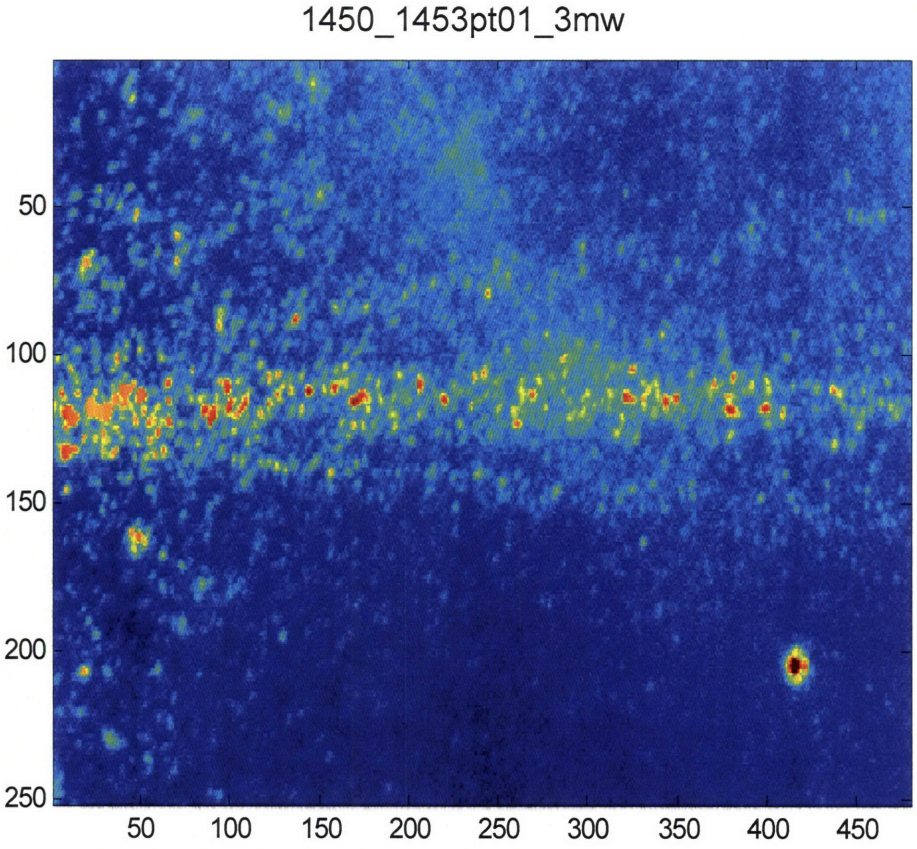

Figure A.13: Experimental scattered light image displayed over a 250 x 500 micron area

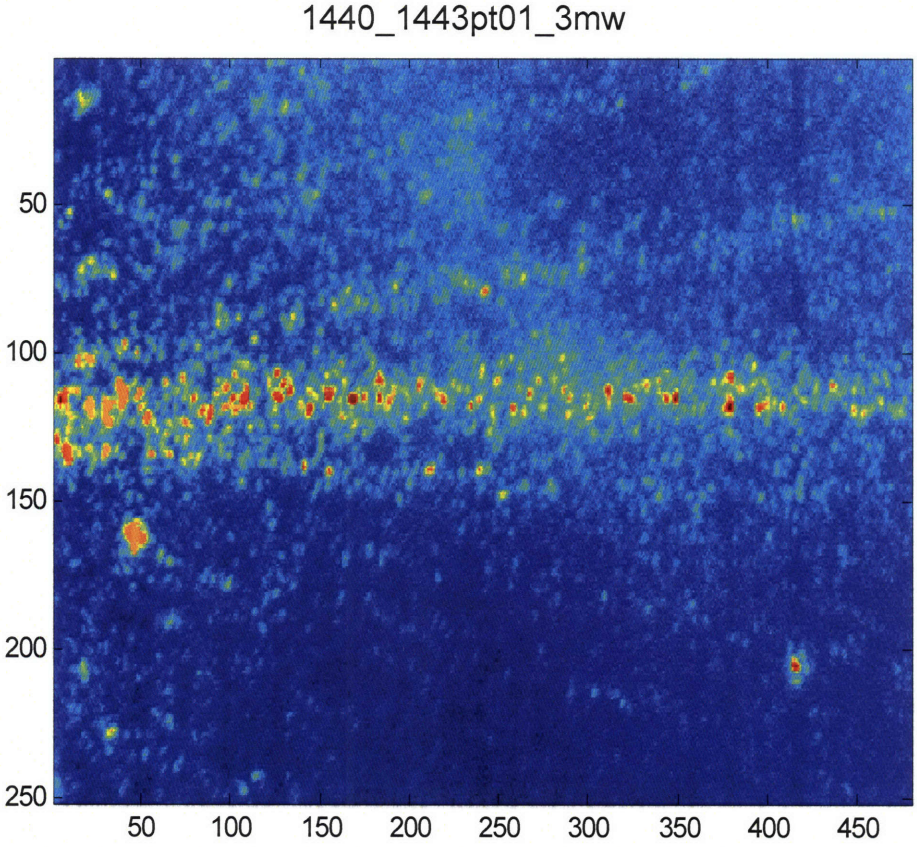

Figure A.14: Experimental scattered light image displayed over a 250 x 500 micron area

Appendix B

Appendix 1B: detailed analysis of phase evolution

In section **1.10** we present a heuristic analysis of beam breakup. In it we claim that diffraction results in a bandwidth limitation to the phase imprinted on the beam as it evolves. (see for example Fig. **B.1**.) In this appendix we describe this phase evolution in more quantitative terms.

In rigorous terms, we can compute the amplitude phase evolution of a beam whose initial electric field amplitude is described by $\tilde{A}_0(x)$ through a Fourier transform and a phase operation as follows [**13**, **4**]

$$\tilde{A}_1(x) = F^{-1}[F[\tilde{A}_0(x)] \cdot exp(k_y(k_x) \cdot L)]. \tag{B.1}$$

Here L is the distance over which the beam propagates, and $k_y(k_x)$ is the dispersion surface expressed as a function of transverse wave-vector k_x. For con-

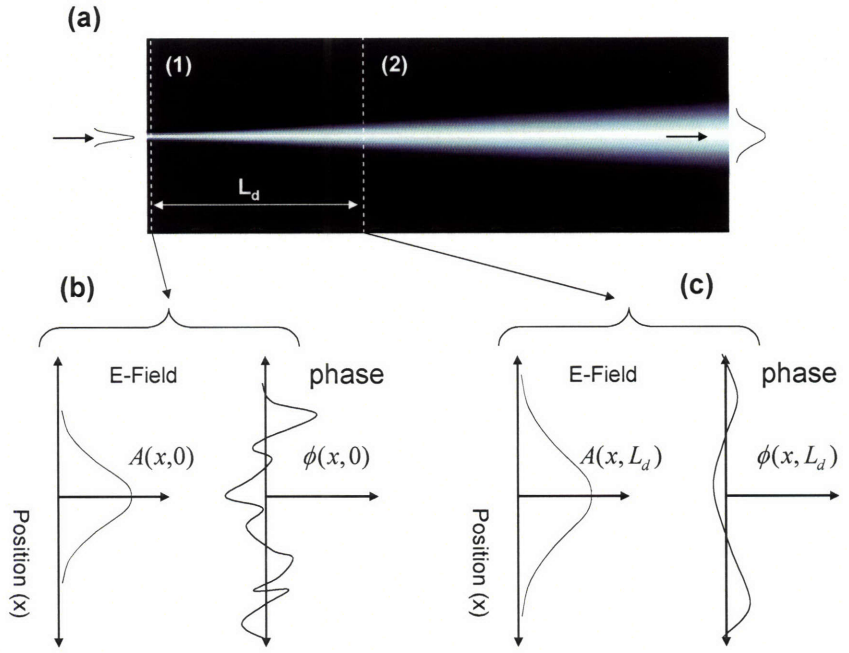

Figure B.1: Diagram illustrating the effects of diffraction on phase noise imprinted on a propagation Gaussian beam (a) Gaussian beam evolution over diffraction length L_d. (b) Plots of the Gaussian beam and phase profiles at start position (1). Here the phase profile is assumed to be broad-band (c) Plots of the beam and phase profiles after propagation over a distance L_d, indicated by position (2).

venience, propagation is also expressed in operator form as $\tilde{A}_1(x) = \hat{P}[\tilde{A}_0(x)]$. Using this formalism we seek some rigorous understanding of how the phase-noise imprinted on a propagating beam will evolve. In the case when the magnitude of the phase-noise,$\phi_0(x)$, imprinted on the beam is small (and assume an initial flat phase otherwise), we can make the following approximation

$$\tilde{A}_0(x) = A_0(x) \cdot exp(i\phi_0(x)) \approx A_0(x) \cdot (1 + i\phi_0(x)). \tag{B.2}$$

Using the above approximation, the phase evolution of the beam becomes much more transparent, since it can be expressed as

$$\tilde{A}_1(x) = \hat{P}[\tilde{A}_0(x)] \approx \hat{P}[A_0(x)] + i\hat{P}[A_0(x)\phi_0(x)]. \tag{B.3}$$

We are interested in how the imprinted phase-noise evolves and contributes to the phase at later points in the beams evolution. To this end, the second term in the R.H.S. fo Eq. **B.3** is most relevant. Since we assume that our beam is of finite extent, without loss of generality, we express our phase-noise as a Fourier sum of the form

$$\phi_0(x) = \sum_j \phi_{a,j} sin(k_j x) + \phi_{b,j} cos(k_j x). \tag{B.4}$$

It is instructive to determine how a single spatial frequency will be manifest on the beam as it propagates. Considering only the term $cos(k_n x)$, the second term in the R.H.S. of Eq. **B.3**. Evaluating we have

$$\hat{P}[|A_0(x)| \cdot cos(k_n x)] = F^{-1}[F[A_0(x) \cdot cos(k_n x)] \cdot exp(k_y(k_x) \cdot L)]. \tag{B.5}$$

Since $F[cos(k_n x)] = 1/2(\delta(k - k_n) + \delta(k + k_n))$, the convolution theorem provides a handy simplification for Eq. **B.5**. Employing the convolution theorem

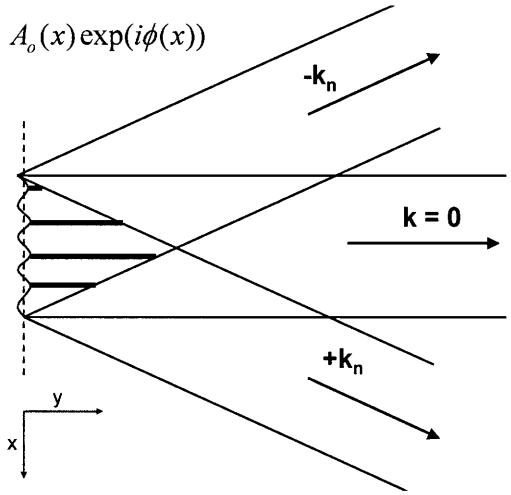

Figure B.2: Diagram depicting the spatial frequencies responsible for the phase oscillation within the beam. As the beams walk apart, the oscillations (or fringes) no longer persist. This geometrical picture makes it clear the apparent length-scale over which a phase oscillation will persist.

the R.H.S of Eq. **B.5** becomes

$$\begin{aligned} &= F^{-1}[F[A_0(x)] \otimes 1/2(\delta(k-k_n)+\delta(k+k_n)) \cdot exp(k_y(k_x)\cdot L) \\ &= 1/2F^{-1}[(\tilde{A}_0(k-k_n)+\tilde{A}_0(k+k_n)) \cdot exp(k_y(k_x)\cdot L)]. \end{aligned} \tag{B.6}$$

From the above expression, we can see that the sinusoidal phase modulation effectively results in two beams centered at $\pm k_n$ in reciprocal space. When these beams are spatially overlapped, a fringe period of k_n results, which is consistent with the phase imprinted on the beam. However, as these beams propagate, their spatial overlap will decrease resulting in decreasing fringe contrast of the phase oscillations. This is illustrated more clearly in Fig. **B.1** which depicts the spatial overlap of two such beams. Furthermore, the larger the value of k_n, the faster the phase oscillations will disperse.

Appendix C

Appendix 1C: Loss estimate from scattered light images for

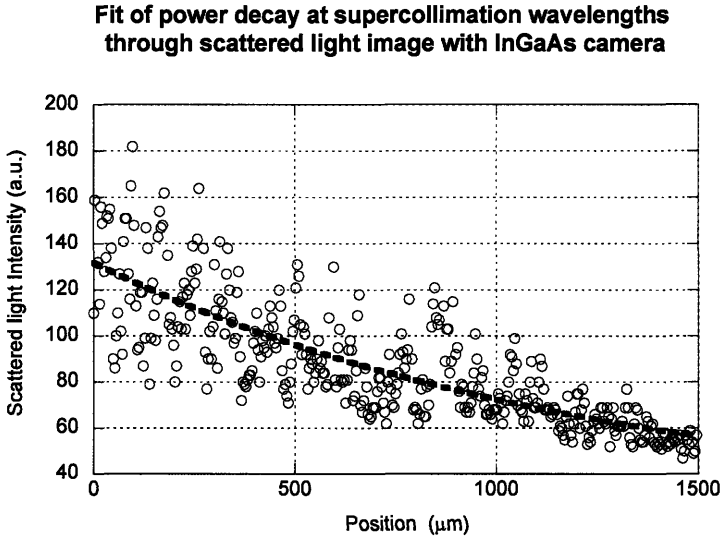

Figure C.1: Intensity of light scattered from the super-collimated beam as a function of position (circles) and exponential fit of the decay (dash). The fit yields a decay length of 1.4 mm corresponding to 3.6 dB/mm

y = m1 + m2 * exp(-M0/m3)		
	Value	Error
m1	24.357	15.152
m2	107.41	13.565
m3	1247.2	306.09
Chisq	93929	NA
R	0.81063	NA

Figure C.2: Functional form of fit (dashed line above), and parameters extracted through fitting algorithm

Appendix D

Appendix 3A: Discussion of various loss measurement methods

The Fabry-Perot method for loss measurement relies on the fact that a waveguide segment, whose ends terminate in air, creates a low-Q Fabry-Perot resonator. The reflectivities (r_1 & r_2) of the cavity ports are determined by the waveguide end-facets, and the waveguide losses influence the maximum fringe contrast observed in transmission through the cavity. This fringe contrast yields some estimate of the waveguide losses. However, in practice this method is difficult to use in studies of HIC waveguides for several reasons: (1) The quality of the waveguide endfacets are typically unknown for nano-scale HIC waveguides (for both cleaving and polishing preparation). This leads to a large uncertainty in r_1 and r_2, and thus waveguide losses. (2) the FSR tends to be very small

(typically 0.1nm for waveguide lengths of 5cm) requiring small laser step sizes, making the measurement fidelity sensitive to the laser line-width. (3) Correct estimate of the reflection coefficients (r_1 & r_2) in the ideal case often requires a non-trivial computations (such as FDTD computations). (4) Due to the aforementioned complexities, this is typically only useful over narrow spectral bandwidths.

The Fabry-Perot method is difficult to use, in part, because the external coupling of the resonant mode is uncertain due to variations in the endfacets. Ideally, one would only measure the internal losses of the cavity under study, and neglect the external coupling. A good approximation of this situation can be obtained through fabrication of a weakly coupled microring resonator. If the ring radius and coupling coefficients are chosen such that $1/Q_{tot} = 1/Q_{ext} + 1/Q_{int} \approx 1/Q_{int}$, waveguide losses can be approximated from the resonant width of the drop response alone. While this method tends to yield reasonable estimates of the scattering losses and intrinsic material losses, it doesn't yield an estimate of stitching errors, since a microring is typically fabricated in a single E-beam field. Furthermore, it shares some of the measurement complexities that the Fabry-Perot method carries, namely it requires very high resolution spectral measurements, and isn't typically useful over large spectral bandwidths.

List of Figures